High Frequency Characterisation of Magnetic Nanoparticles

Daniel M Clarke

Doctor of Philosophy

University of York

Physics, Engineering and Technology

March 2022

Abstract

There has been a renewed interest in magnetic hyperthermia therapies. These provide a low side effect, high precision therapy for malignant and non-malignant tumours. An issue preventing more widespread application of hyperthermia therapies is the inconsistency in heating rate. While the mechanisms of hyperthermia are known their proportions depend on nanoparticle size and shape. The mechanisms of import at the frequencies used are rotational or viscous heating, in which particles physically spin to follow an applied field, and hysteretic heating in which the moment of the particle switches to follow the field. Hysteretic heating is measurable and can be predicted based on a known sample whereas rotational heating is significantly less consistent. This work has three main sections. The first provides further context to the physics around ferrofluids, before describing the equipment and techniques for their characterisation. The second is the presentation of a high frequency B-H looper along with the design process. The looper is the first in its class to use soft ferrites to amplify the field in the sample space by up to a factor 6. This allows for low currents to achieve fields of 420 Oe at frequencies between 47 kHz and 111 kHz. The looper was used to characterise ferrofluid samples at frequencies common in hyperthermia therapies. The third is a comparison of regular colloid based ferrofluid with a new sample in which the nanoparticles have been immobilised in micrometer scale polymer spheres. The immobilised particles cannot rotate to follow the field, providing minimal rotational heating. The hysteresis heating measured in the B-H looper and the specific absorption rate were compared for two regular ferrofluids and one immobilised fluid. For both of the regular fluids, hysteresis heating accounted for 55% of the total heating, whereas for the immobilised nanoparticles this increased to 98%.

Contents

List of Tables

List of Figures

6

11

Acknowledgements

Declaration

I declare that the work presented in this thesis is based purely on my own research, unless otherwise stated, and has not been submitted for a degree in this or any other university.

Signed

Daniel M Clarke

List of Publications

1. Development of a variable frequency, low current, low volume hysteresis loop tracer, Journal of Magnetism and Magnetic Materials 552 (2022) 169249

2. Effect of the distribution of anisotropy constants on the magnetic properties of iron oxide nanoparticles, Journal of Magnetism and Magnetic Materials 559 (2022) 169543

Chapter 1

Introduction

Ferrofluids, first defined in the 1960's by NASA, are magnetic liquids comprised of a suspension of nanometre sized magnetic particles in a carrier liquid [1]. These particles are coated in a dispersant (or surfactant) to prevent the particles from aggregating in the carrier. The advantage of such a liquid is the ability to control several physical aspects though the application of magnetic fields. As an example a ferrofluid can be held in a location against the effects of gravity, have its effective density adjusted or the shape of the surface changed through the manipulation of the field the ferrofluid is in.

The ability for ferrofluids to be controlled remotely has given rise to several important industrial applications. These include, but are not limited to, sealants in high friction environments where a physical O-ring may wear out, damping in modern speaker systems and for use in high end vehicle hydraulics. Ferrofluids have also been used or trialled for biomedical applications. Several varieties of magnetic liquid were used as a contrast medium for Magnetic Resonance Imaging until 2011 [2]. Drug delivery mechanisms, in which the surface of the nanoparticles used are functionalised with a chemical and are then brought to a specific location in the body have been trialled [3]. The application relevant to this study is magnetic hyperthermia, a cancer therapy in which highly localised ferrofluids in a high frequency magnetic field are used to heat and kill cancer cells [4].

The primary advantage of hyperthermia is lack of additional side effects compared with the more common chemo- and radio-therapies. While there is pain as a result of hyperthermia - the process involves applying heat to the point of cell death - it is extremely manageable. The clinical trial in Germany conducted by Johannsen *et al.* [5] found that only a regular course of paracetamol was required after six 5 minute hyperthermia treatments. While hyperthermia is unlikely to be used as a singular treatment [6] it can be used in conjunction with other therapies to reduce the side effects and strain on the body [7]. In addition it may be a suitable substitute for treating non-cancerous tumours in areas where surgery may not be viable, such as the frontal lobe [8].

Iron oxide nanoparticles are the only magnetic nanoparticles currently approved for human use by the Food and Drug Administration (FDA) in the United States [9], though a variety of non-magnetic nanoparticles are still available for other uses. Further to this there is currently only one FDA approved manufacturer, though there are several in the process of acquiring approval [10]. While the magnetite nanoparticles can be safely absorbed by the body [11], there are still concerns with regards to their toxicity. Wu *et al.* state that ultra-small nanoparticles (2.3 nm and 4.2 nm) are highly toxic to mice in their 2022 study [12], while 9.3 nm particles were not. The choice of surfactant also effects the biocompatibility [13]. The particles used by this study are in the process of being approved, but follow the guidelines set by clinical trials.

The aim of this study was the measurement of magnetic nanoparticles in high frequency environments similar to those used by ongoing clinical trials. A primary concern with magnetic hyperthermia as a therapy is the uncertainty of dosage information. This is partially due to difficulties in predicting the heating of ferrofluids used at defined frequencies and fields. Vallejo-Fernandez *et al.* [14] defined the three mechanisms in which nanoparticles produce heat - susceptibility loss, hysteresis heating and rotational (or viscous) heating. While the output of the first two are calculable, rotational heating is not as will be discussed later in this study. This work presents a potential solution to this problem in the form of magnetic nanoparticles that have been immobilised in significantly larger (approximately 300nm) polymer spheres.

Given the difficulty in the calculation of rotational heating, a more specific aim of

this work is the characterisation of hysteresis heating for a set of nanoparticle samples for comparison with a sample that has been immobilised in polymer spheres. This required the design and construction of a B-H looper able to reach the fields and frequencies commonly used - a field of up to 200 Oe (20 mT) driven at frequencies of 111 kHz [15]. B-H loopers are a broad term for a system that measures a full hysteresis loop for a system. The hysteresis heating can be calculated by measuring the area encapsulated by a hysteresis loop the details of which will be discussed further in chapter 3. B-H looper systems commonly take the form of an electromagnet producing a field around a sample with variation in that field producing an induced current in a series of sensing coils. Both Vibrating Sample Magnetometers (VSM) and Alternating Gradient Force Magnetometers (AGFM) are examples of this. However commercial B-H loopers and magnetometers only produce a DC field which does not suit the specifications above. There are systems available to measure the heating rate of samples at suitable frequencies and fields, these systems do not measure the magnetic properties of the samples during the measurement. Rotational and hysteresis heating are measured simultaneously without considering the proportions of each mechanism.

Systems looking to measure the magnetic properties of the samples at hyperthermia frequencies have been built by other academic research groups and were used as a basis for the design used here. The parameters on these systems do not align with the samples used in this project and generally go beyond what is required for hyperthermia treatments as they are currently employed. This either comes in the form of reaching frequencies into the megahertz range (such as Connord's design [16]) or fields that go significantly beyond the saturation point of the HyperMAG samples used in this work (such as Lenox's system [17]). Additionally several of them have the same issue as the commercial designs - the temperature as a function of time is being measured instead of a magnetic characterisation. The system designed here is more targeted to the frequency and field area around those values used in hyperthermia therapies. Limiting the target fields and frequencies in this way allow the system to be considerably cheaper as less range is needed for each electrical component. Additionally it has resulted in a design with a higher signal to noise ratio than the most comparable system in part due to the smaller range of frequencies.

All samples studied in this work were supplied by Liquids Research Ltd [18]. The particles were prepared by the co-precipitation method [19], with controlled growth conditions giving a narrow size distribution. The particles are nominally Fe_3O_4 but the exact composition will lie between Fe_3O_4 and Fe_2O_3.

The thesis beyond this point is split into three main parts, each consisting of two chapters. Chapters 2 and 3 define the theoretical background to the results presented, starting with fine particle systems in general before moving on to the specifics of ferrofluids and a more in-depth explanation of the heating mechanisms mentioned above. Chapters 4 and 5 describe the experimental procedures of this work. These contain descriptions and schematics of each piece of equipment used for the characterisation of the HyperMAG particles. Additionally the measurement procedures are defined for the processes. Chapter 5 is devoted specifically to the design of the high frequency B-H looper. The measurement procedure for the looper is also defined in detail, with explanations for each step. Chapters 6 and 7 present the results of the characterisations completed. This is broken up into the initial characterisations in chapter 6 using well known techniques and equipment, and the high frequency measurements made on the B-H looper and a commercial system known as a Mangetherm. This concludes in a comparison of the total and hysteresis heating for HyperMAGs A and C, as well as the particles that have been immobilized in the polymer spheres as mentioned above.

Units Systems

Generally the research community for magnetism and magnetic materials uses c.g.s units over S.I. units. For convenience the results presented and any equations used in this work are in c.g.s units unless stated otherwise. The primary equation for magnetism in the SI regime is

$$B = \mu_0 \left(M + H \right) \tag{1.1}$$

where B is the magnetic flux density, μ_0 is the permeability of free space, M is the magnetisation and H is the magnetic field strength.

In the c.g.s system, this equation is given as

$$B = H + 4\pi M \tag{1.2}$$

The major difference between the two is the value of μ_0. In the SI system this is given a value of $4\pi \times 10^{-7}$ TmA^{-1}. In c.g.s μ_0 is equal to 1. The conversion for the magnetic flux density B is simple, with 1 Tesla (SI) equalling 10,000 Gauss (c.g.s). The major changes are with the units of H and M. In SI, both the magnetic field strength and magnetisation are measured in Amperes per meter (Am^{-1}). In c.g.s these are Oersteds (Oe) for magnetic field strength and Gauss (G) for magnetisation. Oersteds and Gauss are equal in value, and use the conversion in equation 1.3 below [20].

$$1Am^{-1} = \frac{4\pi}{10^3}Oe \tag{1.3}$$

The other primary measurement value in this work is moment m. This is measured using Am^2 in SI, which converts to 10^3 electromagnetic units (emu). These conversions are stated fully in table 1.1.

Unit	SI		c.g.s
B	1 T	=	10^4 G
H	1 Am^{-1}	=	$4\pi \times 10^{-3}$ Oe
M	1 Am^{-1}	=	$4\pi \times 10^{-3}$ G
m	1 Am^2	=	10^3 emu

Table 1.1: Conversions from SI units to c.g.s.

Experimental Error

The work in this study consists mainly of experimental measurements subject to error. In all cases the techniques used to reduce this error have been documented within the work. In most cases the data is presented with its associated error.

Error in magnetic measurements comes about from the measurement of field and magnetisation. For the DC case the Hall probe is calibrated against a series of permanent standards with a known field, resulting in low errors in the region of ± 1 μG. Magnetisation can have a higher error as a result of poor placement of either the sample or the calibration standard within the field profile. Should absolute values of magnetisation not be required this error can be reduced by normalising the magnetisation to the saturation magnetisation. Absolute values require a calibration standard to convert from the coil measurement (V) to a moment (emu). This is done with either a nickel or palladium standard depending on the expected magnitude of the sample moment.

For the B-H looper error in both the field and magnetisation measurements is higher due to the bespoke nature of the system. Efforts to reduce this error are noted in chapter 5, in which the design of the system is described.

For particle size and shape analysis the errors are relatively small and come as a result of the resolution of the microscopes used and either the Zeiss Particle Size analyser or ImageJ analysis software. These measurements are presented as distributions with their associated standard deviations.

Chapter 2

Magnetic Properties of Fine Particle Systems

2.1 Single Domain Particles

Anisotropy energy E_K is the energy required to pull magnetisation away from a crystal's preferred axis, known as the easy axis. E_K is given by

$$E_K = K sin^2(\theta) \tag{2.1}$$

where K is the anisotropy constant which will be described further in section 2.2.1, and θ is the angle between the applied field and the easy axis. The easy axis is defined by a combination of the magnetocrystalline structure and the shape of the magnet as a whole, aslo described in greater detail in section 2.2.1.

Magnetic domains were initially described by Weiss in 1906 [21]. The domains are regions within the material where magnetic spins are aligned, separated by thin domain walls. This was used to explain why magnetic materials exist in a demagnetized state, as should the domains be randomly aligned the material will show a net zero magnetization. Domains are formed within the material to reduce the energy of the system as a whole [20]. This is a balance between three competing energies - magne-
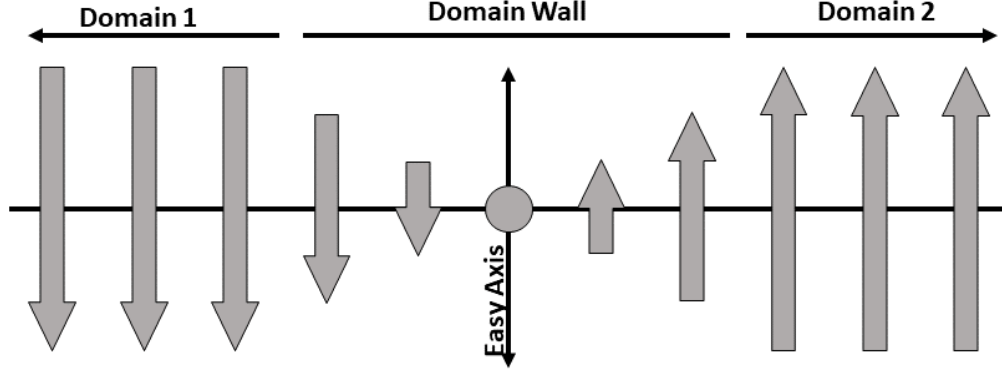
Figure 2.1: Diagram of moments rotating within a domain wall.

tostatic energy E_{ms}, anisotropy energy E_K and exchange energy E_{ex}. Magnetostatic energy, or self energy, is the result of the presence of free poles at the surface of a system, given by

$$E_{ex} = -2J_{ex}\bar{S}_i \cdot \bar{S}_j = -2J_{ex}S_iS_j cos(\phi) \qquad (2.2)$$

where J_{ex} is the exchange integral defined in more detail in section 2.5.4, S_i and S_j are the angular momentums of adjacent atoms i and j, and ϕ is the angle between their spins. The exchange energy is smallest when the angle between the spins is parallel, and so attempts to keep the domain wall as wide as possible so as to reduce ϕ. Anisotropy energy E_K is the energy required to pull magnetisation away from a crystal's preferred axis, known as the easy axis. E_K is given by

$$E_K = K sin^2(\theta) \qquad (2.3)$$

where K is the anisotropy constant which will be described further in section 2.2.1, and θ is the angle between the applied field and the easy axis. The easy axis is defined by a combination of the magnetocrystalline structure and the shape of the magnet as a whole, also described in greater detail in section 2.2.1. The anisotropy energy attempts to make the domain wall as small as possible so as to reduce the number of moments out of alignment with the easy axis.

21

Single domain particles were first theorised by Frenkel and Dorfman in 1930 [22]. Their theory was that if a material is reduced in size to that of the dimensions of a domain wall, it would be more energetically favourable to remain as a permanently magnetised particle rather than split further. In this case, the exchange energy required to form domain walls would be greater than the magnetostatic energy caused by free poles at the surface of the particle. The transition between multi-domain and single domain particles was examined by Kittel in 1946 [23]. Kittel estimates the critical length for single domain particles L_c by equating the single and multi domain states. This leads to equation 2.4 below -

$$L_c = \frac{1.7\gamma_D}{\pi M_s} \tag{2.4}$$

where M_s is the saturation magnetization and γ_D is the domain wall energy density, defined as the sum of the anisotropy energy caused by misalignment of spins from the easy axis and the exchange energy from misalignment between spins. The critical length produced is an approximation, and only for cubic structures. From this, Kittel estimates the critical length to be approximately 15 nm for ferromagnetic elements. A later experimental revision in 1956 [24] adjusted this value to 60 nm. Néel's work in 1947 introduced particle shape as an additional factor [25]. Particles with a longer c axis have a smaller demagnetizing factor along c, resulting in a lower magnetostatic energy. This permits a greater value of L_c provided the particle is elongated.

Lacking a domain wall, single domain particles exhibit different magnetic properties to multi domain. Reversal has to take place via overcoming the energy barrier rather than domain wall motion. This creates a rectangular hysteresis loop for a single particle, as measured by Morrish *et al.* in 1956 [26] and shown in figure 2.2. Particles much smaller than the critical diameter D_c can exhibit superparamagnetic behaviour, which will be discussed in more detail in section 2.4.
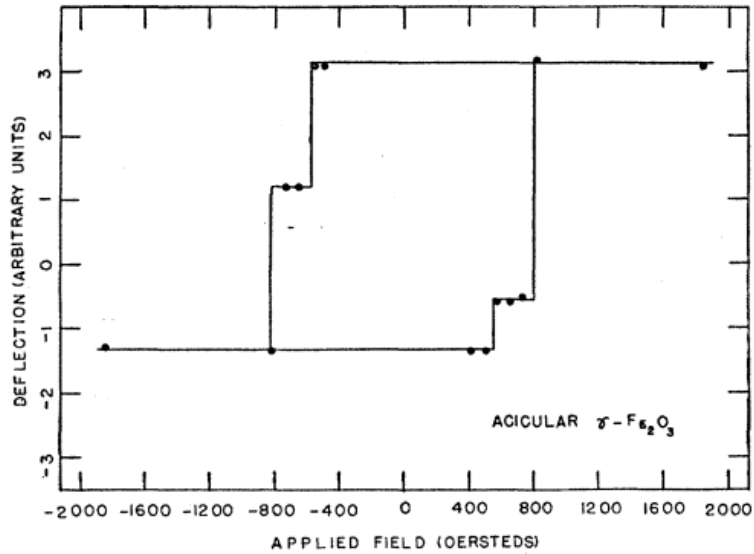
Figure 2.2: Rectangular hysteresis loop measured using a quartz fibre torsion balance. Reproduced from Ref [26].

2.2 Anisotropy

In this section the two anisotropies relevant to this work, crystal and shape anisotropy, will be discussed. As mentioned previously the anisotropies of a crystal define both the easy axis, along which a domain's magnetisation vector will return to in the absence of an applied field, and the energy barrier the particle must overcome in order to reverse. Anisotropy in this case refers to how the magnetic properties of a crystal structure depend on the direction of measurement.

2.2.1 Magnetocrystalline Anisotropy

The crystalline anisotropy originates in the spin and orbital moments in a material. The orbital moments have a strong coupling to the crystal lattice of the material, and are unaffected even in high fields. The spin moments are coupled both to each other through the exchange interaction, and to the the fixed orbital moments. Spin-spin coupling only takes angle between moments into account, and so does not affect the anisotropy. The spin-orbital coupling, however, is comparatively weak and tries to follow the easy axis. When an external field is applied to a domain in a direction

not following the easy axis, an amount of energy is required to break the spin-orbital coupling, known as the anisotropy energy [20] E_K.

The anisotropy energy required to break the spin-orbital coupling applies in any case where an applied field attempts to rotate the magnetization away from the easy axis. In such a case, the field applied has to be able to supply the anisotropy energy to successfully rotate the magnetization. The minimum value for this field is known as the anisotropy field. This is defined as being parallel to the easy axis, and exerting a certain torque (Γ) changes to the magnetization from the easy axis. Equation 2.5 below defines this -

$$\Gamma = H_K M_s \sin \theta \tag{2.5}$$

where H_K is the anisotropy field, M_s is the saturation magnetization and θ is the angle between the magnetization vector and the easy axis [24]. By equating this to the torque applied to the magnetization vector by the crystal (equation 2.6), an approximate value of the anisotropy field can be calculated.

$$\Gamma = \frac{K}{\alpha} \sin \theta \tag{2.6}$$

$$H_K M_s \sin \theta = \frac{K}{\alpha} \sin \theta \tag{2.7}$$

where K is the anisotropy constant and α is the crystal structure constant for the material. α depends on the crystal structure and easy axis of the material. For materials with a single easy axis, known as uniaxial, α has a value of 2 [27].

The lattice structure of the material is the defining factor for crystal anisotropy. If a material has a crystal with a single long axis, such as a hexagonal or tetragonal lattice, it is easier to magnetize along the longer axis. Magnetite has a face centered cubic structure with no long axis. For cubic crystals Akulov expressed the anisotropy energy E_K as a series expansion of the direction cosines of M_s relative to the crystal axis [28].
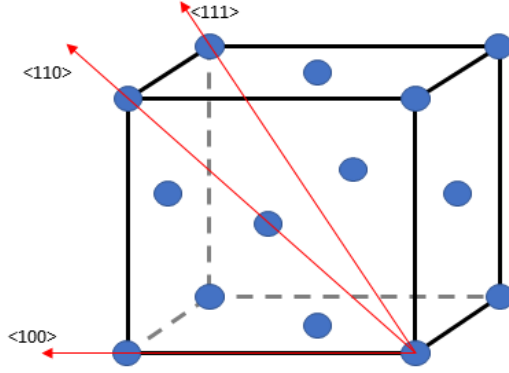
Figure 2.3: Crystal directions for a face centred cubic crystal.

$$E_K = K_0 + K_1 \left(\alpha_1^2 \alpha_2^2 + \alpha_1^2 \alpha_3^2 + \alpha_2^2 \alpha_3^2 \right) + K_2 \left(\alpha_1^2 \alpha_2^2 \alpha_3^2 \right) + ... \tag{2.8}$$

K_0, K_1, K_2 are the anisotropy constants of the material and α_1, α_2, and α_3 are the cosines of the angles between the magnetization vector and the crystal axes. A diagram of the crystal axes for a face centred cubic structure is shown in figure 2.3. K_0 values are independent of the angle of magnetization, and so are generally ignored. The direction of the easy axis of magnetisation is dependent on the sign of K_1. The easy axis for magnetite is along $\langle 111 \rangle$, the value of K_1 is negative [20]. Values beyond K_2 are generally not needed and K_2 itself is generally small and can be neglected. As such, equation 2.8 can be rewritten to give

$$E_K = K \sin^2(\theta) \tag{2.9}$$

where θ is the angle between the easy axis of the crystal and the moment direction, and K is the anisotropy constant for the material. K defines the strength of the anisotropy of a material. This is difficult to measure experimentally as it will vary from sample to sample based on any imperfections or strain the lattice may have. Table 1.1 summarizes several measured values for the anisotropy constant K for magnetite, the material used in this study. The value used generally is by Bickford *et al.* [29] [20].

Additionally the anisotropy constant is variable with temperature, becoming nearly

zero at the Curie temperature and increasing as the temperature lowers towards zero Kelvin[30, 31]. Its temperature dependence is given by

$$\frac{K(T)}{K(0)} = \left[\frac{M_s(T)}{M_s(0)}\right]^n \tag{2.10}$$

where $K(0)$ and $K(T)$ are the anisotropy constants at zero Kelvin and temperature of measurement respectively, $M_s(0)$ and $M_s(T)$ being the saturation magnetisation at zero Kelvin and temperature of measurement respectively. The exponent, n, is dependent on the crystal structure - Zener calculated the value to be 3 for uniaxial systems [30]. If a field large enough to saturate the sample is applied at zero Kelvin, all spins will be aligned with the applied field. As temperature increases local magnetic moments will precess through a range of angles, which when averaged give a local magnetization. As the anisotropy energy must be averaged over the motion of local magnetizations, the anisotropy energy decreases as temperature is increased.

Author	year	value ($x10^5$ erg/cm^3)
Bickford *et al.* [29]	1950	1.1
Mørup *et al.* [32]	1976	13
Söffge *et al.* [33]	1981	6
Hoon *et al.* [34]	1983	0.5
Lambrick *et al.* [35]	1988	0.6

Table 2.1: Various measured values for the anisotropy constant K for magnetite single domain particles.

2.2.2 Shape Anisotropy
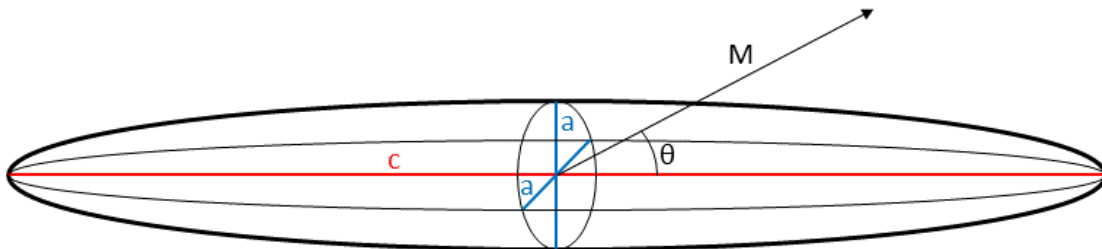
Figure 2.4: Axes for a prolate spheroid particle

The effect of a material's shape on its magnetic properties was theorised by Néel [25]. If a material's structure has no obvious easy axis, such as in the case of some cubic

structures, the shape anisotropy K_S will become the dominant factor. The shape of the material affects the demagnetizing field H_D which in turn defines the shape anisotropy. The demagnetizing field acts in opposition to the magnetization, creating magnetostatic energy within the sample. As the demagnetizing field is strongest at the poles of a material, an elongated shape reduces the demagnetizing factor N_d and so the magnetostatic energy, allowing for easier magnetization. The shape anisotropy is defined as [20]-

$$K_S = \frac{1}{2} \left(N_a - N_c \right) M_s^2 \tag{2.11}$$

$$N_c = \frac{4\pi}{a^2 - 1} \left[\frac{a}{\sqrt{a^2 - 1}} \ln \left(a + \sqrt{a^2 - 1} \right) - 1 \right] \tag{2.12}$$

$$N_a = \frac{4\pi - N_c}{2} \tag{2.13}$$

where N_a and N_c are the demagnetizing coefficients along axes a and c as shown in figure 2.4, and a is the aspect ratio of the particles. Given this value is also dependant on the saturation magnetization M_s, higher magnetization materials will produce stronger shape anisotropy. For magnetite, the cubic 420 emu/cc material used in this study, shape anisotropy becomes dominant for particle aspect ratios of greater than 1.05 [36]. The median aspect ratio for the particles used is between 1.1-1.2 (discussed further in chapter 6) and as such the shape anisotropy is dominant over the crystalline anisotropy.

Though other forms of anisotropy exist, they either produce a negligible effect (in the case of strain anisotropy), or are unrelated (such as exchange anisotropy found in ferro-antiferromagnetic bilayers). As such the total anisotropy of a system is the sum of its crystal anisotropy K_C and its shape anisotropy K_S. Only a small shape anisotropy can cause it to become dominant in cubic lattice structures.

2.3   Hysteresis in Fine Particles

The Stoner-Wohlfarth model [27] describes the reversal mechanism in magnetic at zero Kelvin by rotation of the magnetization vector. The model uses two assumptions, that the particles are single domain and that the moments in all of the particles remain parallel as they rotate (are coherent). The energy barrier to reversal is due to the anisotropy of the particles. In the description of the model, Stoner and Wohlfharth use prolate spheroid particles and as such the shape anisotropy is dominant. The anisotropy energy for a uniaxial single domain particle is given by equation 2.14 below, the angles for which are shown in figure 2.5

$$E_K = KV \sin^2 \theta \tag{2.14}$$

where θ is the angle between the easy axis and the magnetisation vector. If a field is applied at an angle φ to the easy axis of the particle, then a potential energy is acquired by the material due to the field

$$E_P = -HM_S V \cos(\varphi - \theta) \tag{2.15}$$

The total energy is the sum of the anisotropy energy E_K and the potential energy from the field E_P

$$E = KV \sin^2 \theta - HM_S V \cos(\varphi - \theta) \tag{2.16}$$

The magnetisation vector reaches equilibrium when the energy differential with respect to θ reaches its minimum

$$\frac{dE}{d\theta} = 2KV \sin \theta \cos \theta - HM_S V \sin(\varphi - \theta) \tag{2.17}$$

28
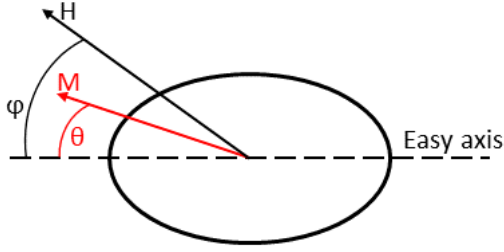
Figure 2.5: Magnetisation directions for uniaxial system with corresponding angles.

The minimum energy values are parallel to the easy axis, at 0^0 and 180^0, and the maximum is at 90^0 perpendicular to the easy axis. The difference between the two energies gives the energy barrier to reversal for the defined particle

$$\Delta E = KV \left(1 - \frac{H}{H_K}\right)^2 \tag{2.18}$$

A system with a cubic anisotropy has a more complicated anisotropy energy than the previously defined uniaxial case. Rather than equation 2.9 for the uniaxial system equation 2.16 below is required, with $\alpha_1, \alpha_2,$ and α_3 defined in equation 2.20-

$$E_K = KV(\alpha_1^2\alpha_2^2 + \alpha_2^2\alpha_3^2 + \alpha_3^2\alpha_1^2) \tag{2.19}$$

$$\alpha_1 = sin\gamma cos\theta \tag{2.20}$$

$$\alpha_2 = sin\gamma sin\theta$$

$$\alpha_3 = cos\gamma$$

The energy of the applied field E_P is similarly expanded from equation 2.15 to give

$$E_P = HM_SV \left[\cos\varphi\cos\Theta + \sin\gamma\sin\Theta\cos(\theta - \psi)\right] \tag{2.21}$$
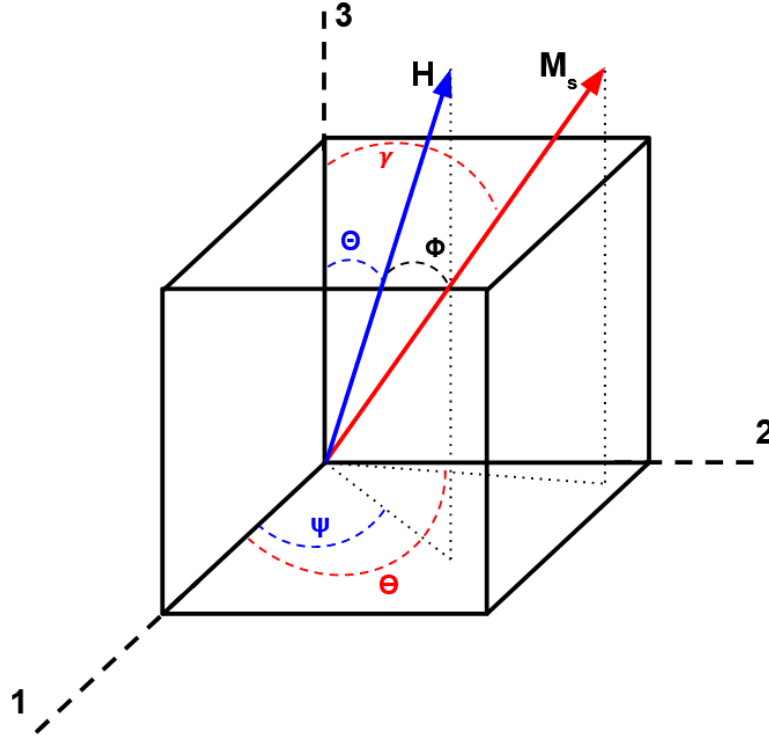
Figure 2.6: Magnetisation directions for a multiaxial system with corresponding angles.

As such, the energy of the multiaxial system in an applied field is given by equation 2.22;

$$E = HM_SV\left[\cos\gamma\cos\Theta + \sin\gamma\sin\Theta\cos(\theta - \psi)\right] + KV\left[\sin^2\gamma - \sin^4\gamma\left(1 - \frac{1}{4}\sin^2 2\theta\right)\right]$$
$$(2.22)$$

with the angles γ, Θ and ψ being those shown in figure 2.5. As with the uniaxial state the easy angles of magnetisation are found where the energy is minimised. In zero field (with a H value of zero) and partially differentiating with respect to γ and θ gives

$$\gamma_{min} = 0 \tag{2.23}$$

$$\gamma_{min} = \frac{\pi}{2}, \theta_{min} = 0, \frac{\pi}{2}, \pi, \frac{3\pi}{2}$$

$$\gamma_{min} = \pi$$

which are the angles of the easy directions. The easy direction is dependant on the sign of the anisotropy constant as described by Joffe and Heuberger [37]. Materials with a positive anisotropy constant have easy axes along the edges of the cube. Those with negative constants are along the body diagonals. As the material in this work have a negative anisotropy constant this case will be described in further detail.

2.4 Superparamagnetism

Néel theorised in 1949 that a particle below a certain volume would spontaneously reverse in zero field, as the thermal fluctuations experienced by the particle would overcome the anisotropy energy barrier [38]. In the presence of an applied field these particles would align towards the field, whilst the thermal energy would oppose this alignment. This is similar in behaviour to a classical paramagnet, with the exception that the moment of the particle is significantly stronger than a standard paramagnet's atoms or ions. This difference in scale led Bean and Livingstone to refer to its behaviour as superparamagnetism [39].

The magnetisation curves of superparamagnetic systems show no remanent magnetisation or coercivity at low frequencies. Additionally, magnetisation curves measured at different temperatures will superimpose if magnetisation M is plotted as a function of field over temperature H/T. The Langevin function (explained in greater detail in section 2.5) describes the magnetic properties of superparamagnetic materials.

Superparamagnetism is defined primarily by two critical factors, the volume and temperature of the particle. For a particle of a given volume there is a temperature above which it will begin to behave as a superparamagnet, which is known as the blocking temperature T_B. Nominally superparamagnetic particles brought below this temperature will begin to show hysteretic characteristics such as coercivity and remanence, and are known as blocked particles. Conversely, for a set temperature,

there is a volume at which superparamagnetic effects do not occur. Particles smaller than this critical volume V_P will exhibit superparamagnetic properties, while larger ones do not. Both T_B and V_P are based on the rate of relaxation of the magnetisation.

If a suspension of single domain particles is initially magnetised before the field is removed, the rate of decrease of magnetisation is dependent on the initial magnetisation $M(0)$ and the Boltzmann factor exp(-ΔE/kT). The Boltzmann factor gives the probability a particle can overcome the anisotropy energy barrier using its thermal energy. The rate of decay of magnetisation is therefore

$$M(t) = M(0)exp(\frac{-t}{\tau}) \tag{2.24}$$

where τ is the relaxation time, defined as the time taken for the remanent magnetisation to reduce by $1/e$. For a uniaxial system in zero field where $\delta E = KV$ the relaxation time is [40]

$$\tau = \frac{1}{f_0}exp\left[\frac{KV(1 - H/H_K)^2}{k_B T}\right] \tag{2.25}$$

where f_0 is the attempt frequency, defined as the average time between two attempts at a magnetic switch. This has a commonly accepted value of between 10^9 and 10^{10} depending on the material [41]. Bean and Livingston defined the relaxation time required for a particle to be considered superparamagnetic as 100 seconds, which is an arbitrary value approximately equivalent to the time taken for a remanence measurement [39]. As the relationship between particle volume and relaxation time is exponential, small variations in τ do not significantly alter the critical volume or temperature. Using a set value for the attempt frequency f_0 of 10^9 [42], the critical volume V_P or the critical temperature T_B can be calculated for a uniaxial system-

$$V_P = \frac{25kT}{K} \tag{2.26}$$

$$T_B = \frac{KV}{25k} \tag{2.27}$$

For a multiaxial system, the energy barrier to reversal is lower, with ΔE either being equal to $KV/4$ for $\langle 100 \rangle$ easy directions or $KV/12$ for the $\langle 111 \rangle$ easy directions. This leads to an increase in critical volume or reduction in critical temperature. For magnetite the easy directions are along $\langle 111 \rangle$, and so the multiaxial V_P and T_B can be calculated using equations 2.28 and 2.29 below.

$$V_P = \frac{300kT}{K} \tag{2.28}$$

$$T_B = \frac{KV}{300k} \tag{2.29}$$

2.5   Effects of Distributed Systems

2.5.1   Langevin Behaviour

As mentioned in section 2.4, the Langevin function describes the process for the magnetisation of classical paramagnets

$$L(\alpha) = \frac{M}{M_0} = \coth \alpha - \frac{1}{\alpha} \tag{2.30}$$

where M_0 is the inital magnetisation and α is $\mu H/kT$. There are two consequences of the Langevin function for classical paramagnets, the first being that for a sufficiently high value of α the paramagnet will saturate. The second is that for lower values of α the relationship between M and H will be linear. As the behaviour of classical paramagnets and superparamagnets is similar, superparamagnets can be described by the Langevin function as well[39]. As superparamagnets have an additional anisotropy term the energy of the superparamagnetic systems are more complex, defined by the

addition of the second term in equation 2.31 below

$$E = KV\sin^2\theta - \mu H\cos\varphi \tag{2.31}$$

where φ is the angle between the applied field vector and the easy axis. Should the system have zero anisotropy, the magnetisation process is described by the Langevin function $L(\alpha)$, with n_v being the number of atoms per unit volume;

$$M = \mu n_v L(\alpha) \tag{2.32}$$

Magnetocrystalline or shape anisotropy do cause deviations from the classical paramagnetic behaviours. While not enough to cause a remanence or coercivity, the magnetic moment of each particle will spend a majority of a period of time aligned with the easy direction of the particle if averaged. This causes an effective drag on the magnetic moments, resulting in the superpositioning of M as a function of H/T not occurring unless KV is significantly smaller than kT [43].

2.5.2 Hysteretic Properties of Fine Particle Systems

In real systems there are deviations from the standard Langevin behaviour described above, due to a size distribution of the particles. Susceptibility is partially dependant on the size of the particle - smaller particles are more thermally active and so harder to saturate. By summing the Langevin functions over the distribution of particle volumes V the magnetization M can be calculated, as shown in equation 2.33

$$M = \int_0^\infty L(\alpha)f(V)dV \tag{2.33}$$

where $f(V)$ is the particle volume distribution, with V_m is the median particle volume,

$$f(V) = \frac{V}{V_m} \tag{2.34}$$

Particle size distributions are generally lognormal [44], so hysteretic properties of fine particle systems are also lognormal.

$$f(V)dV = \frac{1}{\sigma(2\pi)^{\frac{1}{2}}V} exp\left(-\frac{(lnV)^2}{2\sigma}\right) dV \tag{2.35}$$

The critical volume for superparamagnetism is at some point in the size distribution, with some particles being superparamagnetic and some being too large to switch (also known as being blocked). Thus the total magnetization will be the sum of the magnetizations from the three regions shown in figure 2.7. Section 1 contains the smallest, superparamagnetic, particles. Section 2 contains the particles which reverse under the applied field H. Section 3 contains the particles that are too large to switch in field H, but would switch under a larger applied field.
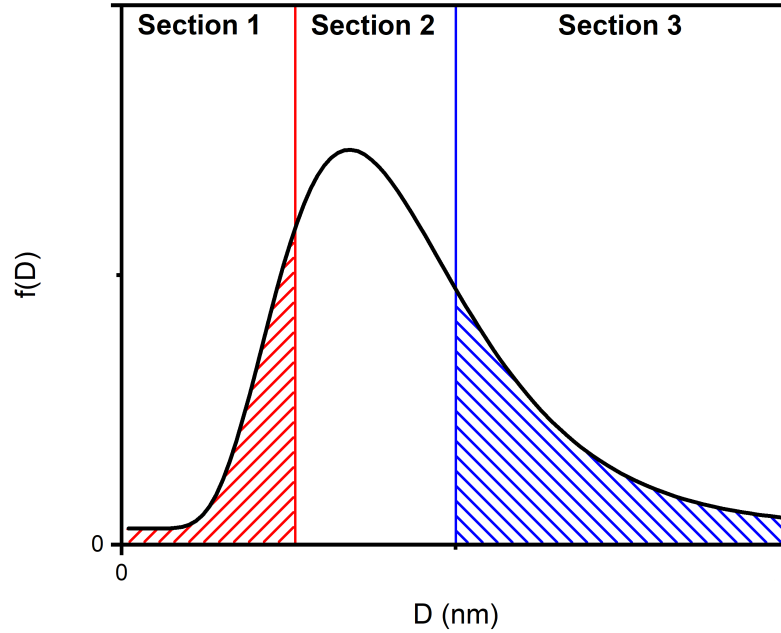
Figure 2.7: Example particle size distribution, with D as the particle diameter and f(D) being the distribution of the diameters. Section 1 contains the superparamagnetic particles, section 2 the particles able to switch magnetically in applied field H, and section 3 the blocked particles that are too large to switch.

The limits for each of the sections can be defined based on the critical volume for superparamagnetism V_P and the applied field H. The upper limit of section 1 defined here as $Z_p(0)$ is calculated using equation 2.36

$$Z_p(0) = \frac{V_p(0)}{V_M} \tag{2.36}$$

where

$$V_p = \frac{25kT}{K} \tag{2.37}$$

Using this as the upper limit for the sum of Langevin functions gives the magnetisation for the superparamagnetic volume of particles M_{SPM};

$$M_{SPM} = \frac{M}{M_S} = \int_0^{z_p(0)} L(\alpha)f(z)dz \tag{2.38}$$

The second section is bounded by the superparamagentic section $Z_p(0)$, and the upper limit of the blocked section $Z_p(h)$. $Z_p(h)$ is defined by the volume at which particles will switch in applied field H, known as the reduced critical volume $V_P(H)$ and is calculated using equation 2.39

$$Z_p(H) = \frac{V_p(H)}{V_m} \tag{2.39}$$

where

$$V_p(H) = \frac{V_p(0)}{1 - H^2} \tag{2.40}$$

The particles larger than $V_P(H)$ remain in their original orientation after field H is applied. As the value of H increases, so does the size of section 2 at the cost of section 3. As such, the magnetization of the blocked particles M_B is the sum of the

particles that reverse and those that do not in the applied field H

$$M_B = \frac{M}{M_s} = \int_{Z_p(0)}^{Z_p(H)} f(V)dV - \int_{Z_p(H)}^{\infty} f(V)dV \tag{2.41}$$

with the total magnetization for the system being the sum of the superparamagnetic and blocked particles

$$M = M_{SPM} + M_B \tag{2.42}$$

Those particles in section 3 that are too large to switch or rotate in the field have an effective contribution of zero as their randomised moments average out.

2.5.3 Coercivity and Remanence

The remanent magnetization of a system is defined as the magnetization of the particles in the system which have remained blocked after a saturating field has been removed. The proportion of these is given by the second term in equation 2.36, and given again in equation 2.43

$$\frac{M_R}{M_S} = \int_{Z_p}^{\infty} f(V)dV \tag{2.43}$$

The coercive field of a system H_c is the field at which the magnetization of reversed particles is equal and opposite to the blocked particles in the original orientation. For a previously saturated system upon which a negative field is applied, the reversed particles will consist of the superparamagnetic region and a number of blocked particles which have been given sufficient energy by the field to reverse.

$$\int_{z_p(H_c)}^{\infty} f(V)dV = \int_0^{Z_p(0)} L(\alpha)f(V)dV + \int_{Z_p(0)}^{Z_p(H_c)} f(V)dV \tag{2.44}$$

The coercivity of a system is the point at which the particles that remain in the initial orientation (term before the equal sign) are balanced by the superparamagnetic particles (first term after the equals) and the newly reversed blocked particles (final term).

2.5.4   Ordering Effects

Due to the separation between particles or groups of particles, the ordering process of fine particle systems differs from that of bulk systems. Bulk system ordering is a result of the exchange interaction between neighbouring spins. Equation 2.45 below defines the exchange energy E_{ex};

$$E_{ex} = -2J_{ex}\bar{S}_i \cdot \bar{S}_j \tag{2.45}$$

or

$$E_{ex} = -2J_{ex}S_iS_j \cos\phi$$

where J_{ex} is the exchange integral, S_i and S_j are the angular momentum of atoms i and j, and ϕ is the angle between their spins. The exchange interaction is still the primary ordering effect within particles in fine particle systems, but not between particles. The ordering is primarily controlled by the blocking of individual particles due to anisotropic energy barriers as discussed in section 2.5.2. Dipole interactions are present between particles but are limited by the concentration of fine particles within a system. If the concentration is small, dipolar interactions can be negligible.

2.6   Surface Effects

As a function of their size, nanoparticles have a significantly higher surface to bulk ratio. As a result any difference between the surface and bulk can modify the characteristics of a set of nanoparticles to a more considerable extent. The surface effects which contribute most to changing the properties of the magnetite nanoparticles used in this work are surface disorder and oxidisation. These will be described here, and their specific effects on the nanoparticles used in this work will be defined in

chapter 3.

Surface disorder arises through incomplete or broken crystal structures along the surface of a material, or at a material/material boundary [45]. This can come about in three ways, distortions of the lattice, defects along the surface or atomic dislocations. These are generally a result of crystal growth or changes to a surface material without changing the bulk. Lattice distortions occur when an ideal crystal structure cannot be formed due to external effects. Examples can include the boundary between two materials with different crystal structures compressing or stretching bonds. Surface defects refer to incomplete crystal structures at the surface. Atoms that cannot be formed into a complete crystal may form defects. These additional atoms can cause the structures around them to deform to accommodate, resulting either in newer structures or sets of incomplete crystals with different characteristics to the bulk [46]. Dislocations are defects which have a larger effect on a lattice as a whole. The most common form, edge dislocations, occur when an extra plane of atoms forms between two layers of a lattice. The resulting non-ideal lattice can effect the properties of the crystal as a whole.

While these faults can form as a function of how the nanoparticles are grown they can also come about as a result of later reactions. Reactive chemicals can cause larger scale changes to the surface of particles, altering the lattice at the surface but failing to penetrate deeper into the bulk. Should the new surface have a differing crystal structure to the original bulk material the lattice can come under strain and deform in the ways described above. This different crystal structure can also result in differing magnetic properties. These could be a total loss of magnetic properties from the surface, changes in anisotropy or variance in the easy axis. The former of these can be largely ignored - should the surface layers be magnetically dead they will not effect the magnetic properties. The latter two pose more of a concern. Variation in anisotropy or material easy axis can result in a phenomenon known as spin canting. This occurs when moments in a material deviate from their parallel alignments [?]. These misalignments complicate the magnetic behaviours of the particles, potentially requiring higher fields or temperatures to switch.
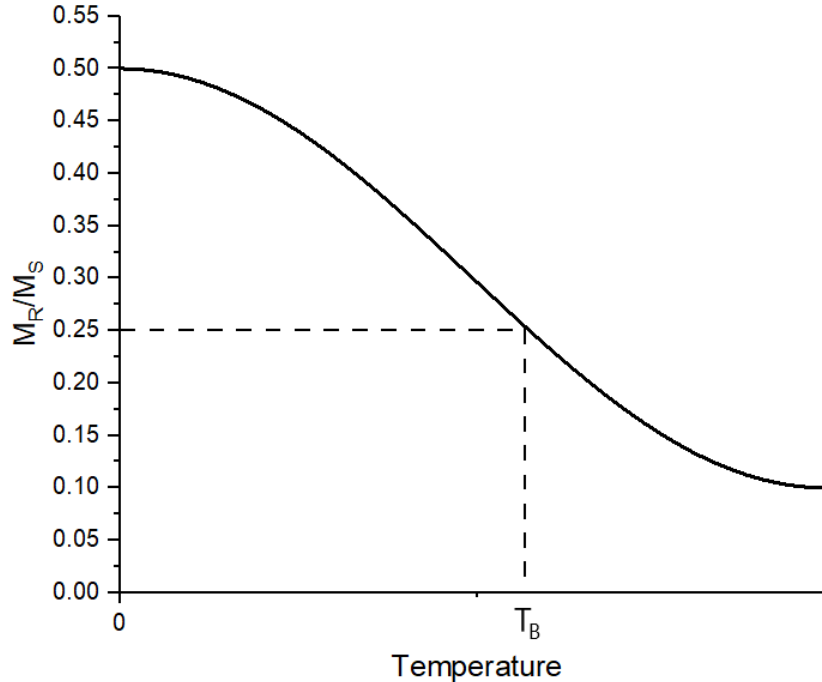
Figure 2.8: Example decay of remanence for a randomly distributed system with uniaxial anisotropy.

2.7 Temperature Decay of Remanence

As described in section 2.5.3, the remanence of a magnetized system is dependant on the superparamagnetic and blocked particles within the size distribution. If all the particles are superparamagnetic the remanence of a system will be zero, if all are blocked the remanence will be the same as the M_s. The variation in remanence as a function of temperature allows for the central region of the particle distribution to be explored.

The squareness of a system is taken as the normalisation of the remanent magnetization to the saturation magnetisation. Squareness is at its maximum value at 0 K. At this temperature the magnetization of all of the particles in the distribution are thermally stable. A randomly aligned system with uniaxial anisotropy, cooled in zero field has an expected squareness of 0.5 [27]. The measured value is slightly lower than this, for reasons that will be explained in section 6.3. This is not affected by the particle size distribution as at 0 K the particles are lower than their blocking temperature T_B. Assuming a narrow distribution of anisotropy constants across the sample, the remanence at a given temperature is given by equation 2.46 [40] -

40

$$\frac{M_r}{M_s} = 0.5 \left(1 - \int_0^{V_P(T)} f(V)dV\right) \tag{2.46}$$

where $V_P(\text{T})$ is the critical size for paramagnetism at the defined temperature and $f(V)$ is the particle volume distribution. As the temperature increases, the squareness value decreases. The increasing temperature allows larger particles to overcome their anisotropy energy barriers. When the temperature of the system has been raised sufficiently to lower the squareness to half of its original value (in this case 0.25 as shown in figure 2.7), the volume of superparamagnetic particles V_P is equal to that of the median particle volume V_m. If a value of V_m is known, equation 2.44 can be used to calculate an effective median value of the anisotropy constant K_m for the system.

$$K_m = \frac{\ln(t_m f_0) k_b T}{V_m} \tag{2.47}$$

t_m is the waiting time at zero field before a remanence measurement is made and f_0 is the attempt frequency. Additionally a variation in the coercivity of a sample with temperature in an applied field is given by

$$\frac{H_c(T)}{H_c^{max}} = \left[1 - \sqrt{\frac{\ln(t f_0) k_b T}{K V_r(T)}}\right] \cdot \int_{V_P(T)}^{V_{(crit)(T)}} f(V)dV \tag{2.48}$$

with H_c^{max} being the the coercivity of the system at a field large enough to saturate the sample, V_{crit} being the maximum volume that can be switched by an applied field. V_r is equivalent to V_m at low temperatures where all of the particles can be switched but otherwise is

$$\frac{\int_{V_P(T)}^{V_r(T)} f(V)dV}{\int_{V_P(T)}^{V_{crit}(T)} f(V)dV} = 0.5 \tag{2.49}$$

For a wider distribution of anisotropy constants a squareness value of half that at 0

K, it is likely that the temperature instead is that of the median value of the energy barrier to reversal. In such cases equation 2.46 needs to be expanded to include the variation in K

$$\frac{M_r}{M_s} = 0.5 \left(1 - \int_0^\infty \int_0^\infty g(K)f(V)\delta(K,V)dVdK \right) \tag{2.50}$$

where $\delta(K,V)$ is a delta type function with values of either one if a given particle becomes blocked at a specific temperature and zero otherwise. Equation 2.45 needs to be altered in a similar way to include the energy barrier to reversal instead of the volume used previously

$$\frac{H_c(T)}{H_c^{max}} = \left[1 - \sqrt{\frac{\ln(tf_0)kT}{\Delta E_r(T)}} \right] \cdot \int_{\Delta E_P(T)}^{\Delta E_{(crit)(T)}} f(\Delta E)d(\Delta E) \tag{2.51}$$

with ΔE_{crit}, ΔE_P and ΔE_r being equivalent to V_{crit}, V_P and V_r.

The method for measuring the temperature decay of remanence and calculating the anisotropy constant described by Gittleman [47] is described in section 4.1.4.

2.8   Temperature Dependence of Susceptibility

Wohlfarth [48] showed the initial susceptibility χ_i of a particle of volume V to be

$$\chi_i = \frac{M_{SB}^2}{3K} \tag{2.52}$$

for temperatures below the blocking temperature T_B, and

$$\chi_i = \frac{M_{SB}V}{3kT} \tag{2.53}$$

for temperatures greater than the blocking temperature, where M_{SB} is the bulk saturation magnetisation. Fine particle systems have a distribution of blocking tem-
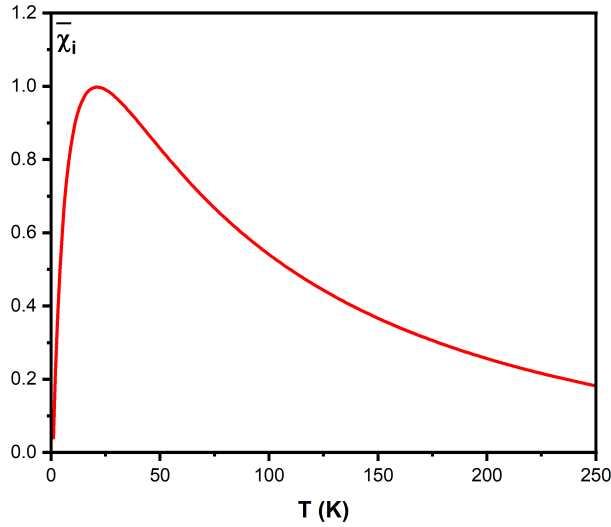
Figure 2.9: Example reduced initial susceptibility $\bar{\chi}_i$ of a fine particle system as a function of temperature.

peratures due to the distribution of particle sizes. Further to this, the initial susceptibility is a sum of the superparamagnetic and blocked particles, and so the initial susceptibility can be calculated using equation 2.54.

$$\bar{\chi}_i = \frac{M_{SB}V_m}{3kT} \int_0^{z_{p0}} zf(z)dz + \frac{M_{SB}^2}{3K} \int_{z_{p0}}^{\infty} f(z)dz \tag{2.54}$$

The term after the equals is the contribution from the superparamagnetic particles. The term after the plus is the contribution of the blocked particles. $\bar{\chi}_i$ is the reduced initial susceptibility given by χ_i/M_s. The limits of the integral are given by the critical volume of transition between blocked and superparamagnetic particles at the defined temperature. Z is the reduced volumes given by V/V_m, with f(Z) being its corresponding distribution. A graph of $\bar{\chi}_i$ as a function of temperature can be seen in figure 2.9

Superparamagnetic particles contribute more to the initial susceptibility than blocked particles, leading to the sharp peak in figure 2.9. Temperature increase does lead to a drop in superparamagnetic susceptibility as given by the Langevin function in section 2.5.1. The susceptibility peaks at a temperature T_g, which is related to the

blocking temperature T_B by the particle size distribution factor β [47].

$$T_g = \beta \langle T_B \rangle \tag{2.55}$$

This suggests that the blocking temperature can be measured through the decay of susceptibility, however the position is also dependent on the applied field and dipolar interactions within the sample. As the strength of dipolar interactions is increased (generally through increase in sample concentration), T_g increases alongside it. This is due to the generally demagnetising effects of the interaction field, modelled by Shtrickman and Wolfarth in 1981 [49].

An applied field will reduces the energy required for magnetic reversal. As such, system in an applied magnetic field will have a reduced blocking temperature compared to the same system in zero field. Wenger and Mydosh [50] defined this variation in blocking temperatures for an aligned system as shown in equation 2.56

$$T_{BH} = T_{B0}\left[1 - \frac{M_{SB}V}{kH_KT_{B0}}\right] \tag{2.56}$$

with T_{B0} and T_{BH} being the blocking temperature at zero field and an applied field of H respectively. Applying a constant to the anisotropy field can make equation 2.54 applicable to the non-aligned system [51].

2.9 Time Dependent Effects

Time dependant effects generally occur after a significant change in applied field. The original field leaves the magnetisation in an unstable state that can relax into a stable state through thermal activation of domains/particles over the anisotropy energy barrier. The Néel-Arrhenius law covers this relaxation for a single particle, though most systems have distributions of factors for both volume and anisotropy. By calculating the number of particles that reverse through thermal activation over a defined energy barrier between E and $E + dE$ the change in magnetisation can be estimated [52]. Integrating over this energy barrier distribution gives

$$\Delta M = M_P p k T \ln(t) \tag{2.57}$$

where M_P is the magnetisation per particle and p is a value proportional to the number of particles in the region between E and $E + dE$. O'Grady *et al* also showed the linear dependence of magnetisation on $\ln(t)$ for a system with a volume distribution [53]

$$M(t) = M_0 \pm \left(\frac{dM}{d\ln(t)} \right) \ln(t) \tag{2.58}$$

with $dM/dln(t)$ being known as the magnetic viscosity S, also defined by Gaunt[54] as

$$S = -\frac{dM}{d\ln(t)} = 2kTM_S f(\Delta E_C) \tag{2.59}$$

and E_C being the critical energy barrier.

The theoretical aspects of magnetic reversal will be discussed in two parts. This chapter has defined the magnetic properties of fine particle systems in the solid state. Next the differences between the solid state behaviour and that of a ferrofluid in the liquid state will be described.

Chapter 3

Properties of Ferrofluids

3.1 Properties of the Liquid State

Ferrofluids are the suspension of magnetic particles in a carrier fluid to create what is in effect a magnetic liquid. These systems are colloidal, and are generally composed of three major parts. These are the particle, a surfactant which coats and separates the particles to prevent aggregation, and the carrier liquid which holds the particles. The ferrofluids used in this study, HyperMAG A and C from Liquids Research Ltd, are magnetite nanoparticles with an oleic acid surfactant and deionised water as a carrier liquid. These are prepared using a modified version of the precipitation techniques based on the method of Khalafalla and Reimers [19]. This involves mixing iron salts in an alkaline solution to create a precipitate of magnetite (Fe_3O_4) and magnemite (Fe_2O_3) nanoparticles. The size of the particles can be controlled by which alkali solution is used, the temperature at which the reaction takes place and the rate at which the reactants are mixed. The median particle diameter is the primary difference between the two fluids. The size distributions were measured as part of this work, the technique of which is discussed in sections 4.2.1 and 4.2.3. HyperMAG A had a measured median diameter of 10.9 nm and HyperMAG C a median diameter of 12.3 nm.

3.1.1 Magnetisation in Ferrofluids

As the ferrofluid is a colloidal solution there are two ways in which magnetisation reversal can take place. These are the magnetisation of the particle rotating to follow the field, known as Néel relaxation τ_N, or the particle itself rotating to fit the field, known as Brownian relaxation τ_B. As such how a particle follows the field is dependant on its magnetic properties alongside the physical properties of the particle and the fluid it is in [3].

Néel relaxation occurs when a particle's magnetisation vector rotates to follow a field without the particle doing so physically. Equation 3.1 defines the Néel relaxation time for a particle

$$\tau_N = \frac{1}{f_0} \exp\left[\frac{KV\left(1 - \frac{H}{H_K}\right)^2}{kT} \right] \tag{3.1}$$

Brownian relaxation is the opposite - a physical rotation of the particle with a stationary magnetisation vector. The relaxation time for Brownian relaxation is given by equation 3.2

$$\tau_B = \frac{3V_h\eta}{kT} \tag{3.2}$$

where η is the viscosity of the carrier liquid and V_h is a particle's hydrodynamic size. The hydrodynamic size of a particle is the volume of the particle itself, as well as the volume of any surfactants, dispersants and carrier fluids attached to the surface. As these volumes of liquid will attempt to rotate with the particle they must be included in its effective volume.

The reversal mechanism for an individual particle is defined by which of the above relaxations is faster. The two possible mechanisms for relaxation give a combined relaxation time τ given by equation 3.3 [14]:

$$\tau = \frac{\tau_N \tau_B}{\tau_N + \tau_B} \tag{3.3}$$

For a given temperature the mechanism of reversal is defined by the size of the particle. Particles below a critical diameter will reverse through Néel relaxation, whereas larger particles will rotate though Brownian relaxation. This critical diameter will be discussed in greater detail in section 3.2 as it defines the heating mechanisms for the system.

3.1.2 Interactions in the Liquid State

Particles suspended in a ferrofluid experience several types of interactions, both magnetic and non-magnetic. To prevent aggregation the attractive forces (magnetic and van der Waals) need to be opposed by the repulsive force of the surfactant. These affect the magnetic properties of the suspended particles.

The primary non-magnetic interaction between particles is the van der Waals force, a general intermolecular interaction. Instantaneous polarisation of molecules, known as the London force, are the most prevalent of these. The motion of electrons within a molecule can cause an instantaneous dipole to appear. This can induce further dipoles on other molecules, causing a partial polarity on non-polar molecules. The opposite dipolar moments will become attracted, with the energy of this attraction E_{VW} being defined by equations 3.4 and 3.5 below, with A_{VW} being the Hamaker constant [55], r the particle radius and S_P the separation of particles. For $r_1, r_2 >> S_p$:

$$E_{VW} = -A_{VW} \frac{r_1 \cdot r_2}{6S_P(r_{1+2})} \tag{3.4}$$

and for $r_1, r_2 << S_p$:

$$E_{VW} = -16A_{VW} \frac{r_1 \cdot r_2}{9S_P} \tag{3.5}$$
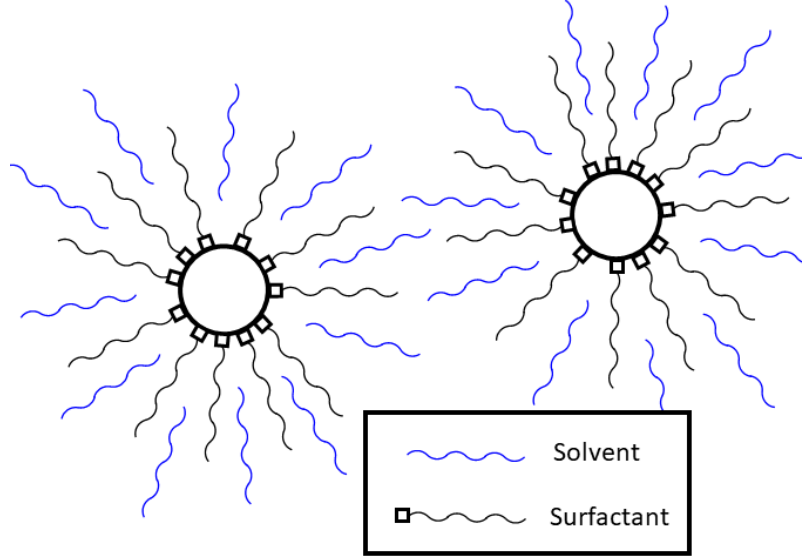
Figure 3.1: Schematic of magnetic nanoparticle with attached surfactant chains. Diagram recreated from Kaiser *et al.* [57].

As the particles are magnetic, there are also magnetic interactions. Magnetic dipole interactions are the primary inter-particle interaction, as mentioned briefly in section 2.5.4. As the particles are magnetic, each acts as a dipole and as such is affected by the moment of the surrounding particles. The energy of this interaction E_D is given by

$$E_D = \frac{\mu_1 \cdot \mu_2}{r^3} \tag{3.6}$$

with μ_1 and μ_2 being the magnetic moments of adjacent particles and r being the distance between them. As the attractive dipolar energy is inversely proportional to the cube of the distance between particles a lower concentration will significantly reduce the aggregation within a sample. These can still be noticeable at low or medium fields, appearing as reductions in the expected susceptibility or magnetisation [56].

Surfactant coatings are used to oppose these attractive forces using entropic and enthalpic effects. The structure of the surfactant molecules provide this repulsion through their long chain structure, with one end bonded to the particle and the other out in the carrier fluid. These provide repulsive entropic effects through the compression of the chains should two particles come close enough. The compression
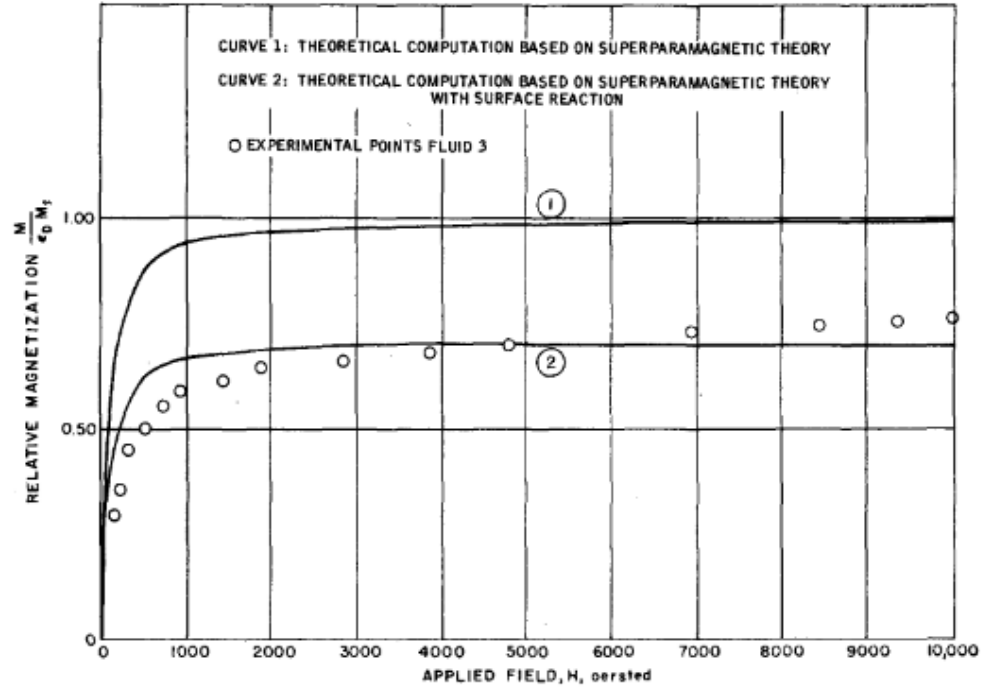
Figure 3.2: Magnetisation curve for a water based ferrofluid using magnetite nanoparticles and an oleic acid surfactant. Curve 1 shows the theoretical magnetisation assuming no surface change to the particle. Curve 2 shows the magnetisation assuming a reduced particle volume due to surface reaction with the oleic acid. Reproduced from Kaiser *et al.* [57].

reduces the possible number of configurations the surfactant chains can fill, and as such increases the free energy of the system causing repulsion. A diagram for these can be seen in figure 3.1.

The enthalpic repulsion comes about as a result of solutions of the free ends of the surfactant chain and the carrier fluid. As the ends of the chain approach each other, the effective local concentration of the surfactant increases. This causes a small repulsion interaction that is significantly smaller than the entropic repulsion [58].

As both magnetite particles and oleic acid surfactants are common in the field, several studies have been completed on the resulting surface effects. These are done through a comparison of the measured magnetisation curve of a ferrofluid and a theoretical curve based on its particle size distribution [44]. An example of this, taken from Kaiser *et al.* [57], can be seen in figure 3.2. The new surface does effect the expected magnetic response of the ferrofluid, with the measured magnetic

size distribution being smaller than the physical size distribution measured through electron microscopy [59]. The surface material formed by the oleic acid and magnetite bond is a non-magnetic iron oleate. As such the more complicated magnetic effects such a surface may have can be ignored. This additional material should be removed for the purpose of calculating magnetic characteristics such as anisotropy constants and particle elongation. Kaiser *et al.* suggests reducing the diameter of particles by 16 $\mathring{A}$ (twice the unit cell thickness of magnetite), Chantrell *et al.* by 15 $\mathring{A}$.

3.1.3 Aggregates

As with fine particle systems, ferrofluids exhibit superparamagnetism in the liquid state. This is independent of the mechanism of magnetisation as even blocked particles can rotate through Brownian rotation. Aggregation of particles within a fluid can cause a break in this behaviour as particles can become large enough to affect magnetisation reversal and bulk rotation.

If the above interactions are not sufficiently balanced, either due to a high concentration of particles or incomplete surfactant coating, clusters of particles may form known as aggregates. These can alter the physical an magnetic properties of the system depending on how it has formed. The interaction that caused the aggregate to form defines the stability and effect on the system. Primary aggregates form due to Van der Waals forces overcoming the surfactant repulsion. These effectively become single large particles and can not be re-separated. Secondary aggregates come from magnetic dipole interactions and are not permanent. These can be broken up through high fields and/or high temperatures. As such the magnetisation of ferrofluids can vary with both field and temperature as secondary aggregates break up and reform.

3.2 Magnetic Hyperthermia

Magnetic hyperthermia is a medical procedure aiming to cause the death of cancerous cells within tumours via the application of highly localised heating using magnetic

nanoparticles. The general aim is the targeted heating of tumours to temperatures of 42 ^{0}C or above [60] for a time period of between 30 and sixty minutes [61]. This process was first trialled in 1957 by R.K. Gilchrist *et al* [62]. The treatment is completed using high frequency (between 50 kHz and 200 kHz) alternating magnetic fields with an applied field strength of between 180 and 200 Oe [4]. Human trials of this therapy have been completed in Germany [5], an example of which is shown in figure 3.3.

Before going into the details of the mechanisms of magnetic hyperthermia, the limitations will be discussed. These are primarily the unwanted side effects of high frequency, high field magnets on the human body. In much the same way a time-varying magnetic field can induce a current in muscles and nerves. This has been reported as having caused discomfort and potential heart arrhythmias. There are two general field and frequency thresholds for these effects. The first, from Reilly [63], was concerned with the high frequencies and fields used by Magnetic Resonance Imaging (MRI) scanners. The limits proposed to prevent nerve and muscle excitation were to not exceed a dB/dt value of 72 Ts^{-1}, or 0.72 MGs^{-1} in the CGS regime. For a frequency of 100 kHz this results in a proposed field maximum of 7.2 G.

In addition, Atkinson *et al.* define a maximum vale for the product of applied magnetic field and frequency [15]. This maximum is the point at which the currents induced in nerves result in discomfort and/or pain. The value for this is given as 4.85×10^8 $Am^{-1}s^{-1}$, or 6.1 MOe s^{-1} in CGS. For a frequency of 100 kHz this results in a proposed field maximum of 61 Oe.

For both of the above cases, neither the clinical trial or the systems designed to measure hyperthermia (which will be described further in chapter 5) use these maxima. Johannsen *et al.* use a maximum field strength of 225 Oe (18 kAm^{-1}) [5], close to four times the maximum suggested by Atkinson. The maximum fields used by the other hyperthermia systems go from 800 Oe to 1600 Oe, though the frequencies of these systems vary more widely. As such the results do not appear to be widely accepted.

The natural cooling mechanisms of the body are an additional concern for the therapy. Tissue perfusion and blood flow both provide active cooling to the body [64]. The cooling power of each is complicated to accurately predict as they vary with

Figure 3.3: Magnetic Resonance Imaging (MRI) scan of an enlarged prostate immediately before treatment, after six 5 minute treatments and six weeks after treatment respectively. Red circles define the location of the prostate gland, with the black dots being the inserted ferrofluid. Images from Johannsen *et al.* [5].

location and temperature differential. Several studies have attempted to define an equation for the cooling rate [64, 65], resulting in equation 3.7 below;

$$c_t \rho_t \frac{dT}{dt} = P_e + \Lambda \Delta T - W c_b \rho_b (T - T_b) \tag{3.7}$$

where c_t and c_b are the specific heat capacity of the tissue and blood respectively, ρ_t and ρ_b are the density of the tissue and blood respectively, $\Lambda \Delta T$ is the heat conduction term for the tissue, W is the blood circulation term and T_b is the temperature of the blood. As the values for most of the terms are variable the heating requirements for maintaining the required 42° vary, though the generally accepted value of 100 mW cm^{-3} is suitable for most cases [61].

Magnetic heating comes about through three mechanisms, depending on operational frequency, particle size and applied field [14]. These mechanisms are heating through susceptibility loss P_{AC}, hysteresis P_{hys} and rotation P_{stir}, with the total heating power P_{total} being the sum of these mechanisms (equation 3.8).

$$P_{total} = P_{AC} + P_{hys} + P_{stir} \tag{3.8}$$

The size and field dependence comes about through the difference between superpara-
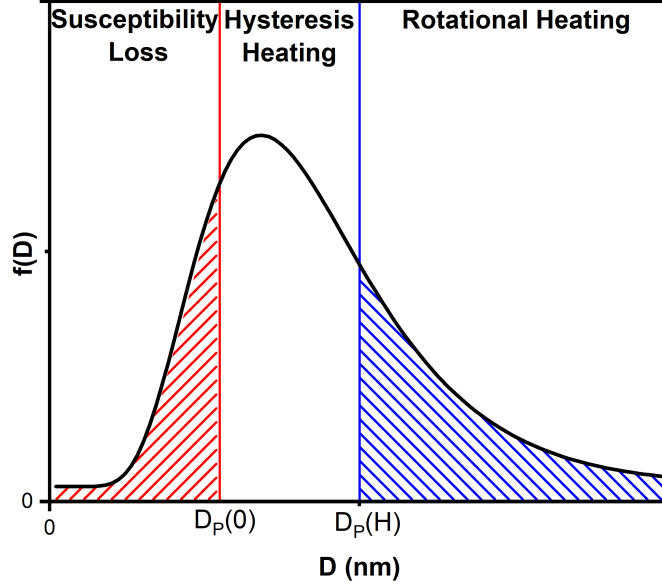
Figure 3.4: Distribution of particle sizes with boundaries based on heating mechanism.

magnetic and blocked particles. At a defined frequency and field superparamagnetic particles will rotate (or if unable to, magnetically switch) to follow the field as needed due to being below the threshold for thermal stability. These have a diameter below the critical diameter for superparamagnetism $D_P(0)$, given by equation 3.9 [39].

$$D_P(0) = \left(\frac{6kT \ln(tf_0)}{\pi K} \right)^{\frac{1}{3}} \tag{3.9}$$

Particles with a diameter below $D_P(0)$ are superparamagnetic and only contribute to the heating through susceptibility loss [14]. Particles larger than $D_P(0)$ are blocked, with an energy barrier too high to switch magnetisation freely. These can be switched by a sufficiently large field allowing them to overcome this energy barrier. For an applied field H the critical diameter that allows for magnetic reversal $D_P(H)$ is given by

$$D_P(H) = \left(1 - \frac{HM_S}{0.96K} \right)^{-\frac{2}{3}} D_P(0) \tag{3.10}$$

with the factor 0.96 occurring as result of the easy axes of the particles being randomly distributed [66]. Particles with a diameter above $D_P(H)$ cannot switch with the applied field H and will instead attempt to rotate to follow the field - while the average field is zero, the RMS field is not. This will lead to the eventual alignment of the particles with the RMS field. This gives rise to rotational heating due to the friction of the particles and their surrounding fluid.

Particles with a diameter $D_P(0) < D < D_P(H)$ have sufficient energy from the field to switch, and as such contribute to hysteresis heating. The sections of the distribution and their equivalent heating mechanisms are shown in figure 3.4.

The heating provided is generally quantified through the measurement of the specific absorption rate SAR. This represents the power generated per unit mass of magnetic material in the solution used, and is calculated in this work by

$$SAR = \frac{c\rho_c}{\phi_{Fe}} \frac{\Delta T}{\Delta t} \tag{3.11}$$

with c being the specific heat capacity of the colloid, ϕ_{Fe} being the density of iron per ml of solution, ρ_c being the density of the colloid and $\Delta T / \Delta t$ as the heating rate. There is no consideration within this to the specific heat capacity of the sample holder which will take a proportion of the heating generated by the sample. In addition the procedure used to measure the SAR can vary from group to group, resulting in different SAR values for the same sample [67]. The SAR equation is also variable, with different groups adding variables deemed important [68][69][70]. Overall SAR values should only be compared for samples measured with the same measurement system with the same technique [71].

3.2.1 Susceptibility Loss

Susceptibility losses arise due to a separation between the applied field H and the moment of the sample m. At lower frequencies it is possible for the superparamagnetic particles to follow the field precisely. As this frequency increases a separation appears between m and H as the particles fail to rotate at adequate speeds due to
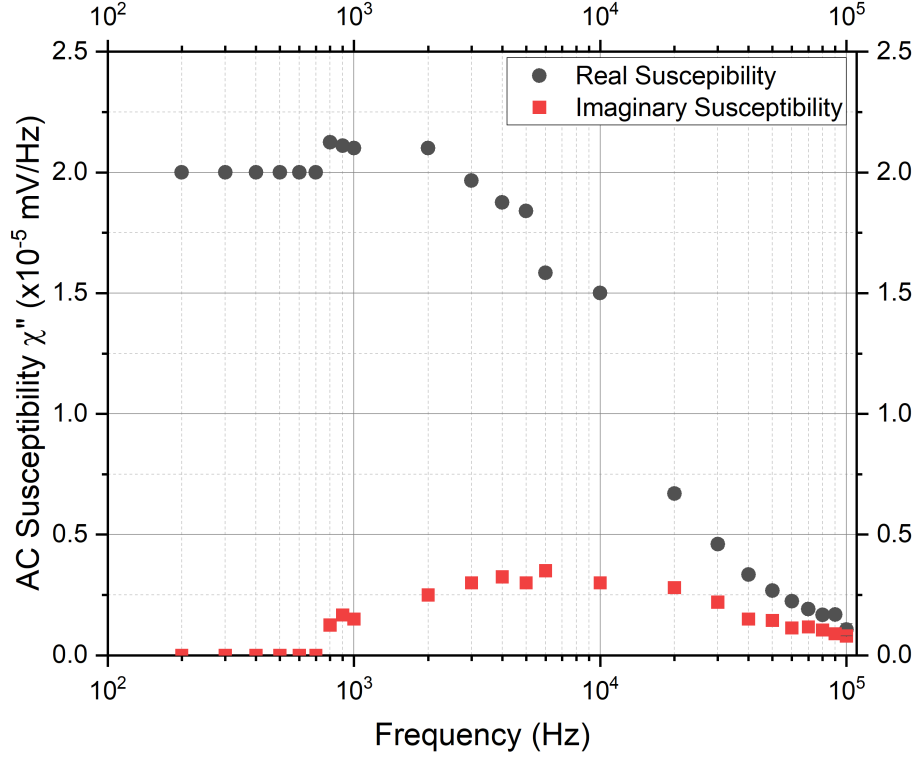
Figure 3.5: AC susceptibility as function of frequency for HyperMAG C, measured in an AC susceptometer built in group.

the limits from Brownian rotation [1]. This creates a magnetostatic energy, which is released in the form of heat. The heating power through susceptibility loss P_{AC} is given by

$$P_{AC} = \pi f \chi'' H^2 \tag{3.12}$$

with χ'' being the complex part of the AC susceptibility, which can be calculated using equation 3.13.

$$\frac{\chi''}{\chi_i} = \frac{2\pi f \tau}{1 + (2\pi f \tau)^2} \tag{3.13}$$

At higher frequencies (10^5 Hz) there is a significant drop in the AC susceptibility as shown by figure 3.5. As such it provides the smallest contribution to the heating at the frequencies generally used for magnetic hyperthermia.
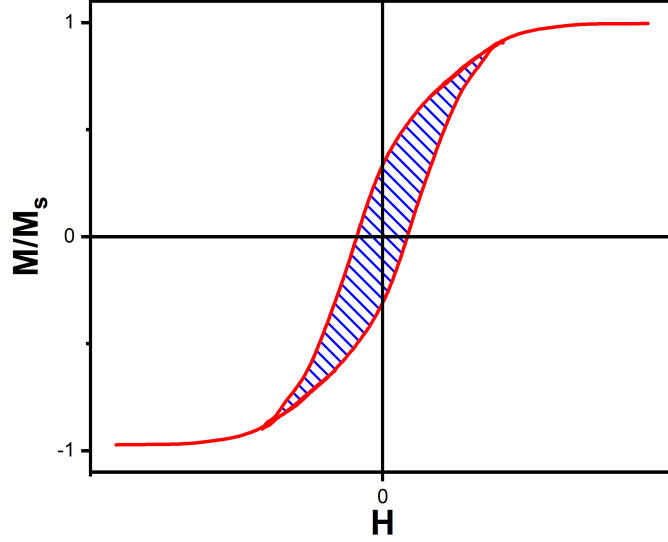
Figure 3.6: Example hysteresis loop with shaded area showing magnetostatic energy lost to heating.

3.2.2 Hysteresis Heating

Hysteresis heating is the second contributor to the total hyperthermia output. This mechanism arises from the blocked particles irreversibly switching their magnetic moment in response to the field rather than physically rotating. The hysteresis heating power of the particles P_{hys} is proportional to the area enclosed by the hysteresis loop at a set field and frequency, as shown in figure 3.6

$$P_{hys} = 2M_s f \int_{V_P(0)}^{V_P(H)} H_c(V) f(V) dV \qquad (3.14)$$

where $H_c(V)$ and f(V) are the coercivity and volume distributions across the particles. The variation of H_c with particle size can be seen in equation 3.15.

$$H_c = H_K \left[1 - \left(\frac{6 \ln(t f_0) kT}{\pi K D^3} \right)^{\frac{1}{2}} \right] \qquad (3.15)$$

57

This equation assumes a perfect sample, and is not applicable should the sample have any defects. Equations 3.10, 3.14 and 3.15 assume a non-distributed anisotropy constant for the particles. The importance of the distribution of anisotropy constants in magnetite samples has been shown in work completed by McGhie [72]. This would likely result in a lower value of P_{hys} than that calculated using a uniform K. The technique used to define the anisotropy distribution for the HyperMAG samples used in this work is described in section 4.

3.2.3   Rotational Heating

The final heating mechanism for the particles is rotational or viscous heating. This is a result of the particles being too large to switch attempting to physically rotate to follow it. The calculation of the heat generated by the frictional drag on the particle P_{stir} is extremely complex for multiple reasons. The drag coefficient is not known for the surfactant/carrier fluid boundary, or how the surfactant behaves in the case of aggregates. Similarly the flow of carrier fluid around the nanoparticles is likely to be turbulent, further complicating any calculations. The drag may also cause an effect similar to susceptibility loss in larger particles as the particles lag behind the field. The use of a solenoidal field with a finite RMS value will also likely result in aggregates and larger particles gradually aligning with the field. This could cause a non-linear reduction in P_{stir} as a function in time. As such, there is currently no way to effectively calculate or estimate the rotational heating.

This lack of an estimate for the heating rate presents a concern for the development of dosage information for the medical applications of magnetic hyperthermia. An experimental program described by G Vallejo-Fernandez *et al* [14] tried to quantify the proportion of P_{total} that the stirring contributes. This was done through the comparison of the SAR of HyperMAG A, B and C in two isoparaffin oils (Isopar M and Isopar V) as well as in a wax. The wax served to effectively immobilize the particles removing the stirring component of the heating. The SAR, measured using the Magnetherm system described in chapter 4, showed a drop in SAR of between 30% and 40% from the Isopar M samples to the wax samples, as shown by figure 3.7.

If the heating from rotation can provide up to 40% of the total heating, but cannot
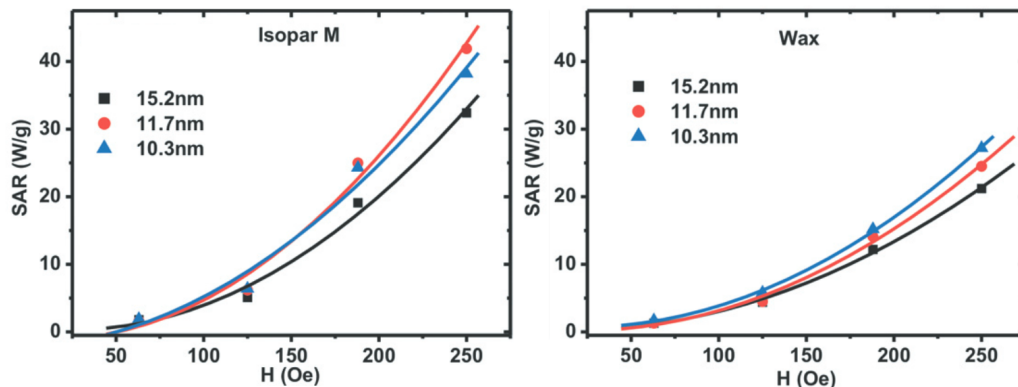
Figure 3.7: Specific absorption rates for HyperMAG A (blue), B (red) and C (black) at 111 kHz in both Isopar M and a wax measured by G Vallejo-Fernandez *et al.* [14]

be calculated or estimated, this presents an issue for the creation of dosage values. If the effects cannot be consistently measured or quantified an alternative solution is the removal of this aspect of the heating through the immobilization of the particles in a solid medium.

3.2.4 Particle Immobilization in Polymer Spheres

As mentioned above, the heating mechanism used by the particles is linked to both the size of the particle and the applied field strength. Given the difficulty of calculating the rotational heating and its impact on the overall SAR value, ideally this mechanism would be suppressed or removed. In this study two techniques have been employed to attempt to reduce the power of rotational heating. The first of these is an increased field strength compared to current hyperthermia models [5], from 200 Oe to above 400 Oe. This increases the value of $D_P(H)$ and so reduces the number of particles following the field via rotation. The second technique is the immobilization of the nanoparticles using larger polymer spheres, images of which are displayed in figure 3.8. This uses the variation of Brownian relaxation time as a function of volume to reduce the stirring. The larger the particle the longer it will take to rotate as shown by equation 3.2. Figure 3.9 shows the variation of relaxation time with particle diameter. From this, a sphere with a diameter of 100 nm would have a Brownian relaxation time of approximately 0.4 ms, and for the sphere's used in this study (300 nm) the relaxation time increases to 80 ms.
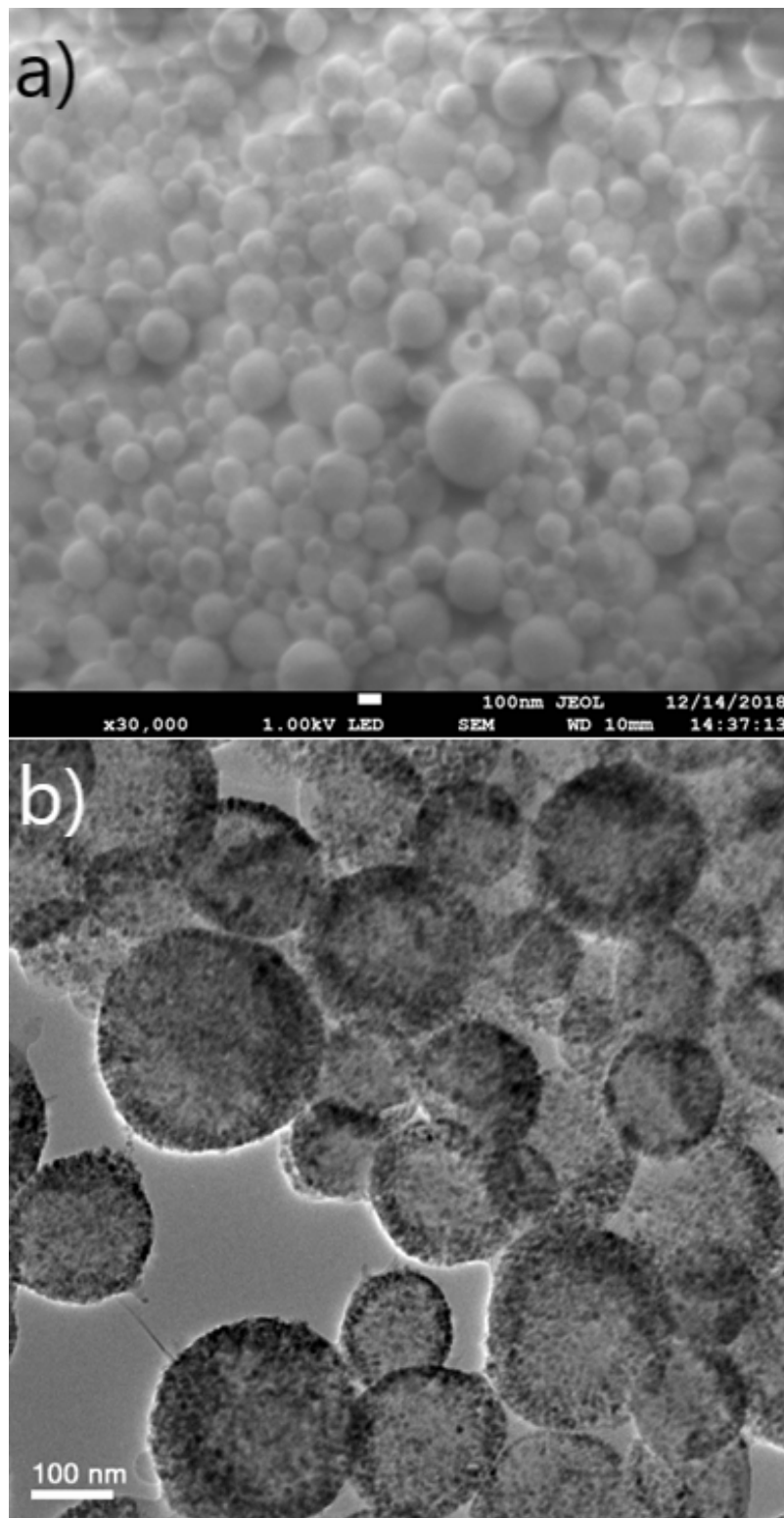
Figure 3.8: Images of polymer spheres taken using a) a Scanning Electron Microscope to image the spheres taken by Dr Edward Jackson, and b) a Transmission Electron Microscope to show the encapsulated particles.
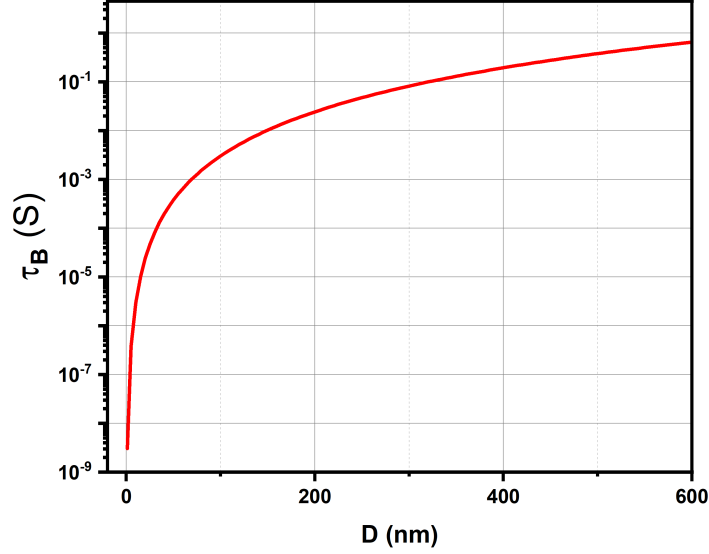
Figure 3.9: Brownian relaxation time as a function of object size in deionized water.

At the frequencies commonly used for magnetic hyperthermia the spheres themselves will be effectively immobilized due to the difficulty in attempting to follow the field. As such the stirring will be effectively removed as a heating mechanism, through the immobilization will likely cause further effects to the heating. Given the magnetite particles are locked in their orientation and can not follow the field there will likely be an increase in the heating through susceptibility loss. The polymer used has a specific heat capacity of between 1300 and 1500 J/kg^{0}C (approximately 1/3 that of deionized water). This should not affect the heating rate of the system by much, but the additional material transition may reduce the heating rate of the fluid. The spheres will likely have a reduced effective surface area compared to the nanoparticles individually, providing another possible reduction in heat rate.

Chapter 3 concludes the descriptions of the theoretical aspects of magnetic reversal in the solid and liquid state, as well as the primary mechanisms of magnetic hyperthermia. The next chapters will cover the experimental procedure for the primary results of the thesis.

Chapter 4

Evaluation of Magnetic Nanoparticles

In this chapter the main experimental techniques for the characterisation of the magnetic nanoparticles will be described. Vibrating Sample Magnetometers (VSMs), both in York and the University of Zaragoza, were used to evaluate the magnetic properties of the samples. Physical characterisation was completed using both a Transmission Electron Microscope (TEM) and a Scanning Electron Microscope (SEM) at the University of York Nanocentre. Finally a hydrodynamic size measurement completed using Photon Correlation Spectroscopy (PCS) and a high frequency heating test completed using a Magnetherm system, both competed at Liquids Research Ltd in Bangor, Wales.

4.1 Magnetic Evaluation

4.1.1 Vibrating Sample Magnetometer

Vibrating sample magnetometers (VSM) are one of the most versatile magnetic measurement systems in use. The general form is unchanged since its description in 1956 by Forner [73]. A uniform magnetic field is generated using large coil windings around

pole pieces. The sample is vibrated vertically in a uniform magnetic field to induce a voltage in sensing coils. The field is measured using a Hall probe, and current altered to achieve the desired field.

The voltage induced in the sensing coils is given by Faraday's law of induction, described in equation 4.1.

$$V_i = -N_c \frac{d\phi_f}{dt} \tag{4.1}$$

$$\phi_f = (H + M) \cdot A_c \tag{4.2}$$

where V_i is the induced voltage, N_c is the number of turns in the sensing coil, ϕ_f is the magnetic flux from the sample and t is time. The sample is vibrated using a linear actuator so as to produce a time varying ϕ_f. The sample's total magnetic flux is based on the sum of the field applied by the VSM, H, and the sample's magnetisation, M, multiplied with the area of the detection coil A_c (equation 4.2). When combined with equation 4.1, the voltage induced in the coils can be summarised as:

$$\int V_i dt = -N_c A_c \cdot M \tag{4.3}$$

As the external field is invariant during the time of measurement, only the sample's magnetization contributes to the induced signal in the coils. The primary magnetometer for this project was a Lakeshore Model 8600. This system, a schematic of which is shown in figure 4.1a, is comprised of a set of four Mallinson sensing coils, an electromagnet and variable separation of the pole pieces, and a continuous flow cryostat. The magnet is water cooled and can reach fields of 2 T provided the pole pieces are at their lowest separation. The Model 10 has a noise floor of 5 μemu, which can be reduced to 0.5 μemu with a 10 second per point averaging time. The sample is vibrated at 80 Hz, with full user control over the amplitude of the vibration.

The cryostat is a Lakeshore 86-CRYO system that can be installed depending on the measurement procedure. It is rated for liquid nitrogen (LN_2) and argon use,

allowing for a range of temperatures between 100 K and 450 K. When using liquid nitrogen, the cryostat has a temperature stability of $\pm 0.2K$. This is a continuous flow open system as a closed cryostat can affect the sensitivity of the vibrations through contact with the vacuum seal. The temperature is controlled from within the VSM software using a PID controller (proportional integral derivative).

Given the raw output of the VSM is in the form of a voltage rather than a defined magnetisation value, the system needs to have both the H field and signal response components calibrated regularly. The H field calibration requires the removal of the VSM gaussprobe to confirm two defined reference points. The first is a null field zone, the second is a defined permanent reference magnet. Both of these are checked beforehand using an external LakeShore 425 model gaussmeter. The signal (the magnetic moment of the sample) response requires a calibration standard dependant on the sample being measured. The standard needs to be as close in shape to the sample in question as possible, to ensure no difference in demagnetization factor (chapter 2). The shape used in this case is defined in chapter 5.

The location of the sample within the field volume is also critical for minimising error. The sample should sit centrally within the field profile and between the sensing coils. The sample has to be in this ideal location, not the sample probe, where the probe sits to allow for this will change depending on the dimensions of the sample. The Lakeshore 8600 VSM has the vibration unit mounted on a translation stage with manual dials for movement in the three axis directions to allow for careful placement of the sample. While the orientation of the sample will depend on what characteristics are being measured, throughout this work samples are orientated parallel to the field lines (direction X in figure 4.1W).

The process for ensuring the sample is placed correctly is called saddling, the procedure for which is as follows. The calibration standard is mounted on the sample probe and placed within the VSM. The VSM should be set to show moment as a function of time. The field should be the same as the maximum used in any measurements to follow. The micrometer dials are then adjusted to move the sample into the correct location based on the sample signal. In the X direction (left right on figure 4.1W) the sample should be moved to the point at which the signal is minimal. As the sample approaches a pole piece the field experienced by the sample (and so the induced signal in the sensing coils) will increase, as shown in figure 4.1X. In both Y
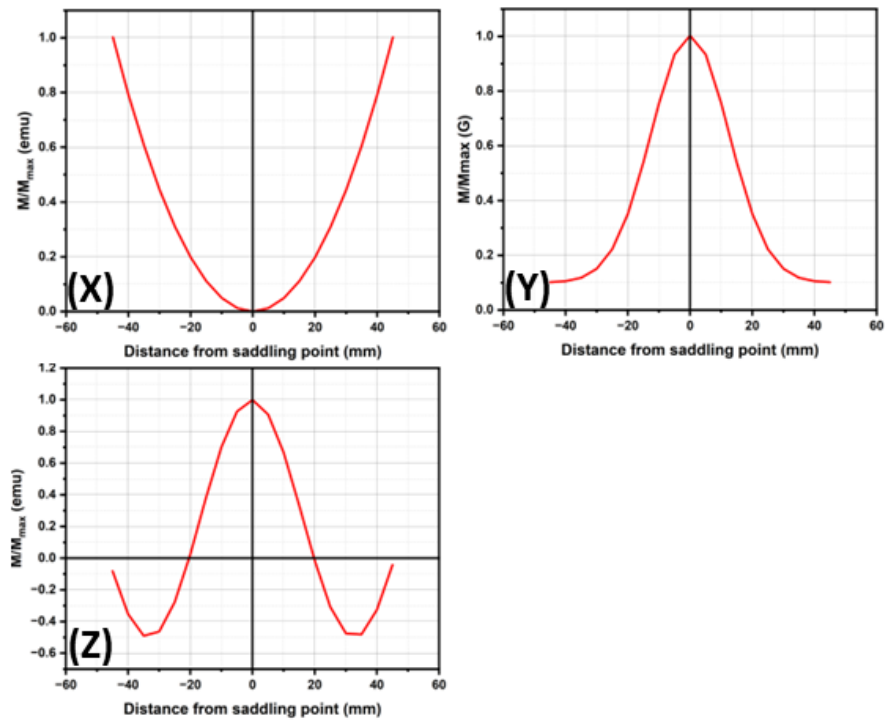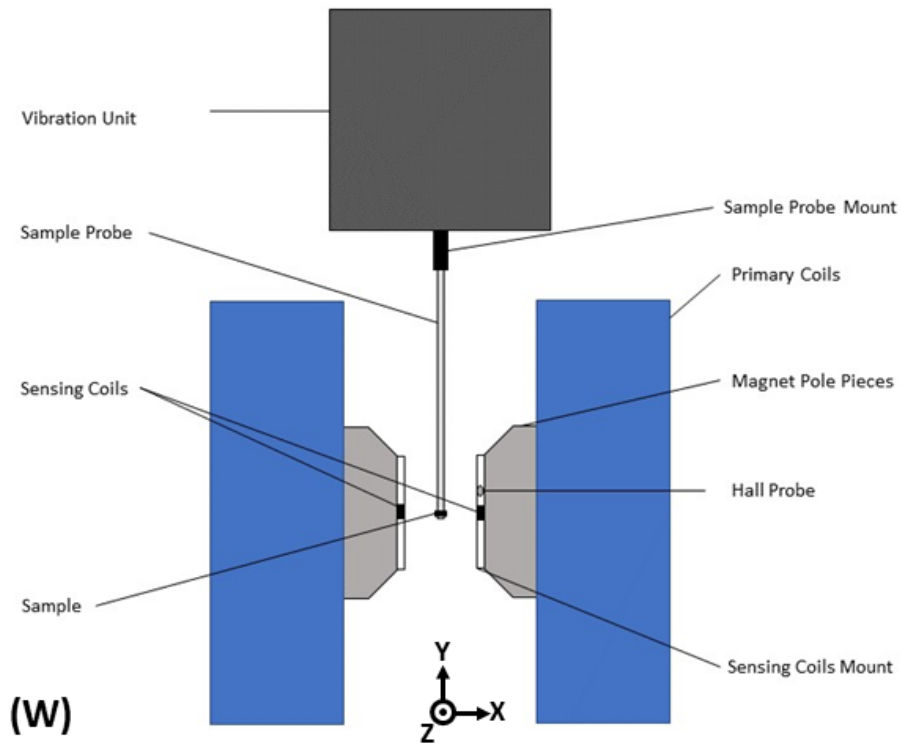
Figure 4.1: (W) Schematic diagram of the Lakeshore 8600 Vibrating Sample Magnetometer, with saddling profiles in X (X), Y (Y) and Z (Z) directions. Saddling profiles recreated from the Lakeshore Model 8600 manual [74].

(forwards and backwards, figure 4.1Y) and Z (up and down, figure 4.1Z) the sample signal should be maximised, as moving away from the sensing coils will reduce the signal. All three of the axis directions should be adjusted several times to confirm that the calibration standard is saddled correctly. While this should not need to be repeated between samples, this process should be completed before using a VSM as a previous user may have had samples with different dimensions.

The material of the calibration standard should also aim to provide a similar magnitude of response to the sample. In this case a palladium (Pd) rod was machined into shape and placed inside the same tubing used for the ferrofluid samples, 5 mm long by 1 mm diameter. Palladium is a Pauli paramagnet and as such has a defined magnetic susceptibility which is independent of temperature of $5.26 \times 10^{-6} cm^3 g^{-1}$ [56]. The calibration standard is saddled between the sensing coils and a magnetization curve is measured. The gradient of the curve is compared to the expected gradient, as defined by the mass of the Pd sample. A calibration factor is then calculated and applied to all further measurements. This calibration factor generally lies in the region of -260 to -290 emu/V. The signal response calibration is completed before each set of measurements.

Due to the small distance between the coils, specialist sample holders are required. The sample must fit comfortably into the opening of the cryostat (8 mm), whilst also keeping a sufficiently high aspect ratio as to minimize the demagnetizing factor N_d. Given these constraints the sample dimensions were chosen to be 5x1 mm, holding a volume of 4 μl of fluid. The N_d value for this aspect ratio is 0.055, based on values listed in Stoner and Wohlfarth [27]. The sample holder was made of a piece of silicone tube, outer diameter 2 mm, inner diameter 1mm. For each sample a 6 mm section was cut and one end sealed using epoxy resin. 4 μl of fluid was inserted using an Eppendorf micropippete. The other end was then sealed with epoxy resin.

Two main varieties of measurements were completed on VSM systems for each sample. The first were simple room temperature magnetisation curves to measure the magnetization in DC. These were compared to the high frequency measurements discussed in chapter 5 to ascertain M_s for the samples. The second were remanence measurements at low temperatures, completed by C Marquina *et al.* at the University of Zaragoza [75].
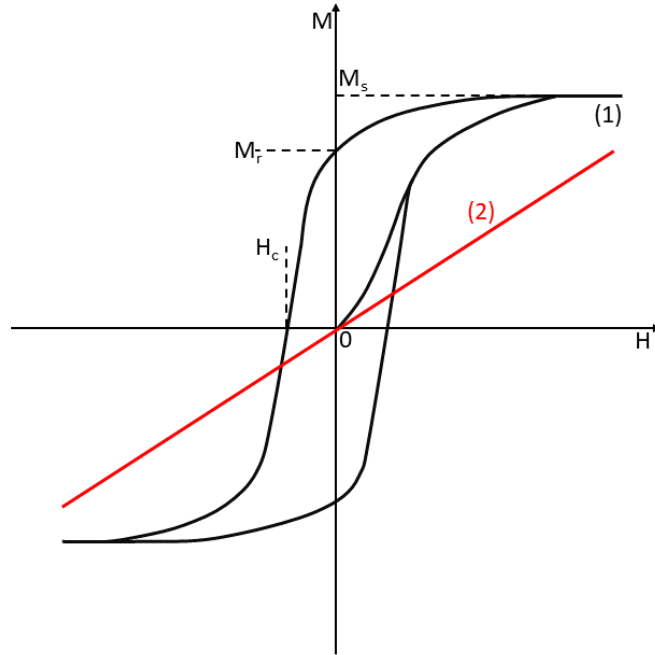
Figure 4.2: Characteristic magnetisation curves for a ferromagnetic (loop 1) and paramagnetic (line 2) sample.

4.1.2 Magnetisation Curves

A magnetization curve (or hysteresis loop) is a measurement of the magnetization M of the sample as a function of the applied field H. DC magnetization curves provide some of the key characterizations of the fluid, the saturation magnetization M_s, the coercivity H_c and the remanent magnetisation M_r. These are defined graphically in figure 4.2 for a ferromagnetic sample - paramagnetic samples have no values of H_c or M_r. The saturation magnetisation is defined as the point at which all of the moments within the sample are aligned with the applied field, and as such no more magnetization can take place. Having saturated the sample, the coercivity is defined as the field required to return the magnetization to zero, and the remanent magnetisation is the magnetisation of the sample once the applied field is reduced to zero. Both of these are dependant on the measurement conditions, as will be discussed in section 6.

4.1.3 Temperature Decay of Remanence

The second characterisation is the determination of the anisotropy constant K through the measurement of the temperature decay of remanence. The mathematics of this is described in section 2.6. The measurement process was initially designed by Gittleman [47], but has been completed more recently by Tari *et al* in 1979 [40], and by McGhie *et al* in 2017 [72].

200 μl of HyperMAG A and C samples were cooled in zero field to a temperature of 1.8 K using a SQUID magnetometer equipped with a continuous flow cryostat - these measurements were completed at the University of Zaragosa. At this temperature a hysteresis loop was measured with a maximum applied field of 50 kOe to establish the field required to saturate the particles at this temperature and their coercivity. The hysteresis loop of the HyperMAG samples closed at approximately 2 kOe, so 5 kOe was established to be suitable to fully saturate the samples and as such was used as the saturating field for the remainder of the experiment. After the hysteresis loop the sample was re-saturated, then the field was removed and the remanence measured after 100 seconds. From here the temperature was raised in steps of 2-5 K. For each step the sample was resaturated, the field was removed and the remanence measured after a wait of 100 seconds.

The temperature at which the remanence has reduced by half was noted. This was used in conjunction with the measurement of the particle size and shape distributions (as described in section 4.2.3). A comparison was made between the expected remanence using a single anisotropy constant based on equation 2.41 (repeated below)

$$\frac{M_r}{M_s} = 0.5 \left(1 - \int_0^{V_P(T)} f(V)dV \right) \tag{2.41}$$

and the expected remanence for a distribution of anisotropy constants using equation 2.43 (repeated below)

$$\frac{M_r}{M_s} = 0.5 \left(1 - \int_0^\infty \int_0^\infty g(K)f(V)\delta(K,V)dVdK \right) \qquad (2.43)$$

and the measured outcome.

4.2 Electron Microscopy

Physical analysis of both the HyperMAG and polymer sphere samples was required. Electron microscopy was first used in 1932 by Knoll and Ruska [76]. As there was a variation in size and material of the two samples, different techniques were used to image them. For the unmodified magnetic nanoparticles a Transmission Electron Microscope (TEM) was used. A Scanning Electron Microscope (SEM) was used to image the polymer sphere sample, as the polymer appears transparent to the TEM and the SEM gives a much wider field of view for objects of approximately 500 μm in size.

4.2.1 Transmission Electron Microscopy

A JEOL JEM-2011 TEM was used in this study. This model uses a lanthanum hexaboride (LaB$_6$) tip to produce the electrons via thermionic emission. This beam of electrons then passes through two condenser lenses - the first to converge the beam and the second to determine the spot size before hitting the condenser aperture. This removes any electrons scattered too far from the primary beam path. After the three condenser aspects of the TEM, the beam interacts with the sample. The electrons are scattered an amount based on the density and composition of the material directly in their path. The objective lens reassembles these into a diffraction pattern of the whole sample, the optional objective aperture again remove any electrons scattered off the beam path. The diffraction pattern is converted into an image by the intermediate and projector lenses before being projected onto the screen. A schematic diagram of the TEM can be seen in figure 4.3).

The TEM can be used in three different ways to produce an image. Dark and bright
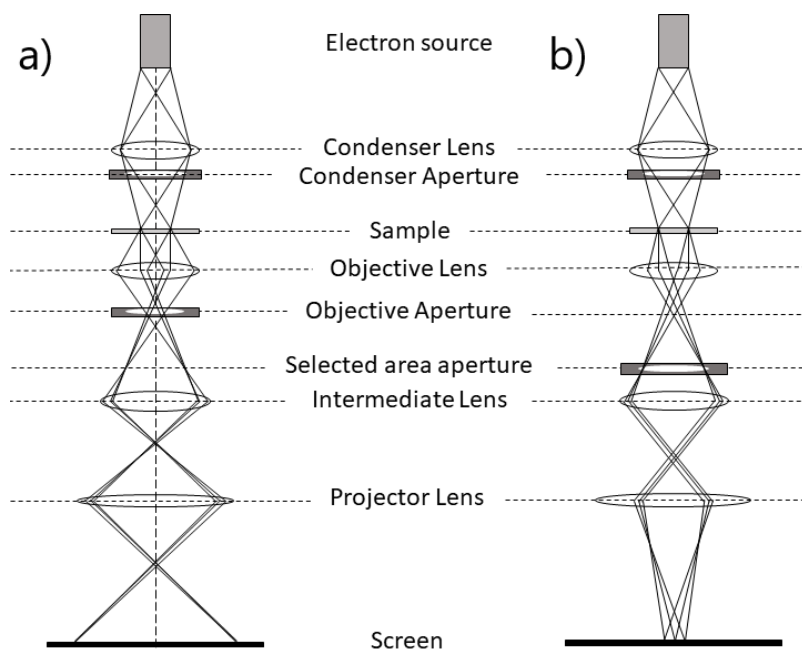
Figure 4.3: Schematic diagram of a Transmission Electron Microscope to create either an image (a) or a diffraction pattern (b).

field imaging use the objective aperture to control which level of electron scattering provide the majority of the image. When bright field imaging, the objective aperture blocks all electrons but those of the centre of the diffraction pattern. These images show low density areas as light as these contain the least scattered electrons, and the higher density areas as dark. An example of bright field imaging can be seen in figure 4.4. Dark field imaging is the opposite, with the objective aperture only allowing a specific set of scattered electrons through. The third technique is High Resolution TEM (HRTEM), which (provided the resolution of the TEM is high enough) can be used to measure atomic spacings and distances.

TEM samples were made by initially diluting the ferrofluid by a factor 10-1 in deionised water. This reduced the aggregation of the dried sample allowing for cleaner imaging. A small volume of the diluted fluid was then pipetted onto a 400 mesh carbon coated copper TEM grid. The solution was left to dry off. The TEM samples were made as close to the time of measurement as possible to minimize risk of contamination. Images were taken over a wide area of each grid to acquire a more accurate measure of the particle size distribution. For each particle size analysis a distribution of at least 500 particles was used so as to accurately measure the standard deviation σ.

70
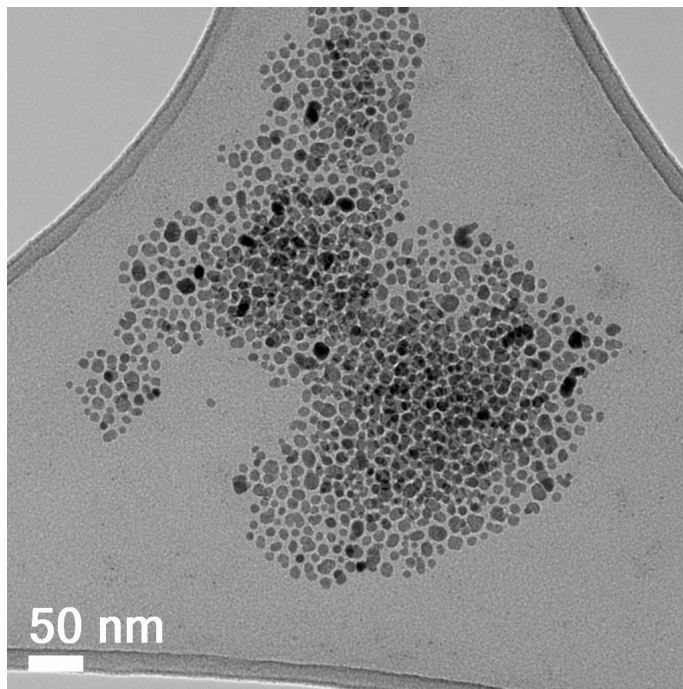
Figure 4.4: Bright field image of HyperMAG A nanoparticles taken on JEOL JEM-2011 TEM.

4.2.2 Scanning Electron Microscopy

Similarly to the TEM, the SEM uses a focused beam of electrons to create an image. The primary difference is in how the electron interactions are used to produce an image. Whilst in TEM the electrons pass through the sample and the major cause of contrast is the degree to which the electrons are scattered, SEM scans the electron beam across the surface of a sample and measures the results of the interactions caused. For the purposes of the imaging completed in this work only the secondary and backscattered electrons are relevant [77]. Both are the result of electron collisions with the surface of the sample, with the primary difference being the energy of the scattered electrons. Secondary electrons are the primary contributors to SEM surface imaging. They are the result of inelastic scattering and as such have lower energy than the incident beam. Their lower energy means that only the secondary electrons from the surface of the sample are able to escape and be collected by the detectors. This provides surface detail but limited information about sample composition. Backscattered electrons come from elastic collisions and so have the same energy as the electron beam. These are primarily used for sample composition analysis, however are relevant to the surface imaging process as they cannot be
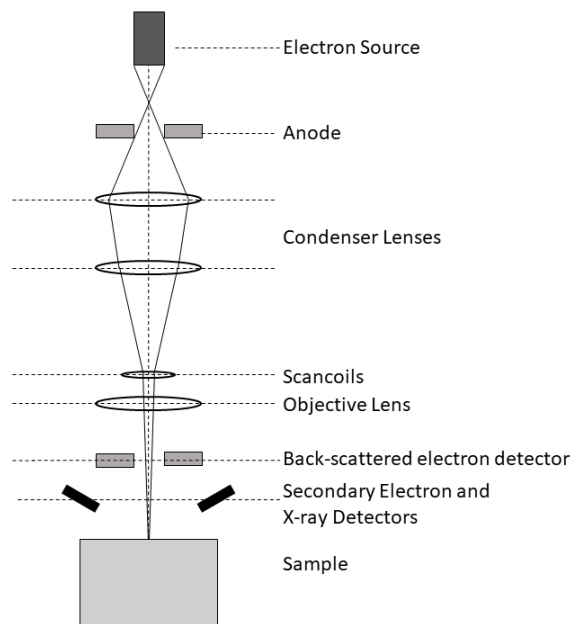
Figure 4.5: Schematic diagram of an SEM

removed from the detection process.

The primary detector used for secondary electrons is the Everhart-Thornley detector [78]. This uses a small metal grid to accelerate the low energy secondary electrons to a scintillator. Any technique to reduce the number of high energy back scattered electrons would result in much more significantly reduced secondary electron detection. Applying a negative bias to the accelerator prevents secondary electrons being detected. Backscattered electrons are also measured in an upper detector should sample composition be needed.

For the purposes of the size analysis, only the lower electron detector data was required. A JEOL 7800F Prime SEM was used to take the images used in the polymer sphere size analysis, a schematic of which can be seen in figure 4.5. The magnification range for the JEOL 7800F was between 100x and 50,000x, though a magnification of 15,000x was used for all images taken. An example image of the polymer spheres described in chapter 3 can be seen in figure 4.6.
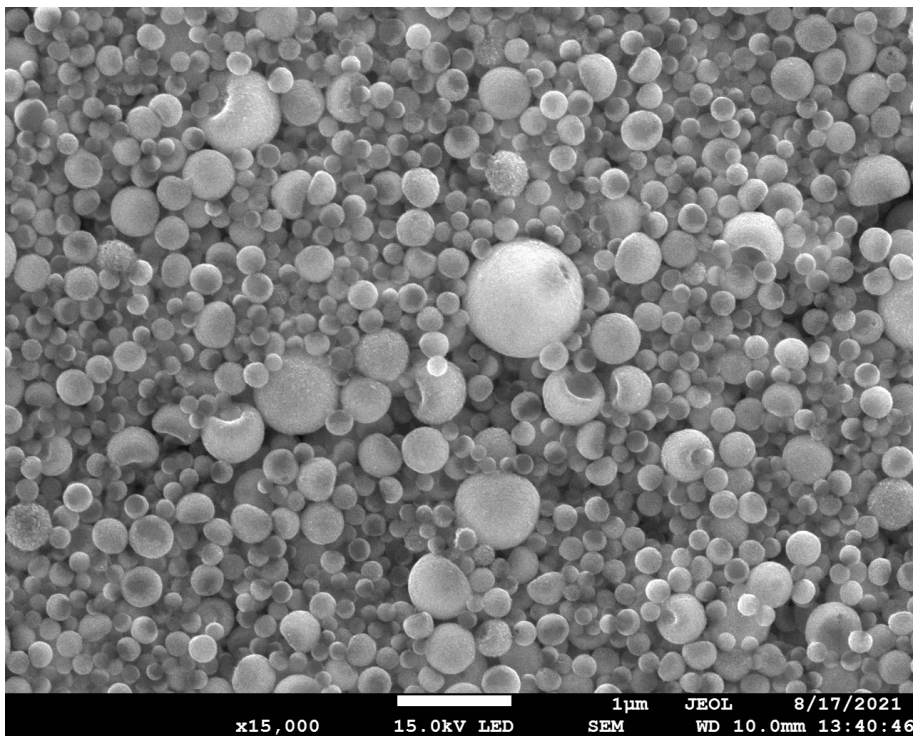
Figure 4.6: Image of polymer spheres taken on JEOL 7800F Prime SEM.

Each of the samples for the SEM were prepared by pipetting 10 μL of suspended polymer spheres onto an aluminium SEM stub. These were left to dry out, leaving the polymer spheres on the surface of the target. A strong permanent magnet was held over the surface of the stub before being inserted into the SEM to pull any loose particles away.

4.2.3 Particle Size and Shape Analysis

After images of the samples had been obtained either on the TEM or SEM, the grain size analysis was completed using a Zeiss particle size analyser. This functions by using a lightbox with a variable aperture to approximate the diameter of a particle via the equivalent circle method. This interfaces with LabView via an NI DAQ interface. For each particle the diameter is saved as a ratio of the measured aperture diameter and the maximum aperture diameter. This is saved within the LabView software in bins, which were 2% of the maximum diameter. The scale bar provided by the SEM or TEM is measured and used to convert the bins back to μm or nm.

A shape analysis was also required for the HyperMAG samples and was completed using imageJ [79] (an image processing and analysis software). For each particle the long and short axis were measured using the line tool and converted into nanometres from pixels. This gave an elongation and equivalent circle diameter for each measured particle. This will be discussed further in chapter 6.

4.3   Additional Measurements

4.3.1   Heating Power of Magnetic Nanoparticles

In addition to the magnetic and physical characterisation of the samples, the heating power was also measured. This was achieved using a modified Nanotherics Magnetherm system described by Drayton *et al* in 2017 [80]. This system uses a 55 mm long, 17 turn, two layer coil with an inner diameter of 50 mm. This generates a 180 Oe alternating field driven at 111.5 kHz by an RF oscillator. A schematic diagram of the modified sample cell and primary coil is shown in figure 4.7.

The modifications for the system improve three areas - heat losses, convection heating and field uniformity in the sample space. Within the field profile of the primary coil there is a volume of 10 mm tall by 20 mm wide in which the field is uniform to 10%. The provided sample holders were the same length as the coil (55 mm), resulting in different volumes of the sample experiencing differing field strengths. A sample cup with 20 mm diameter allows for 3 ml of fluid in the area of field uniformity. A stirrer with an electric motor was used to counteract the effects of convective heating.

For the heat losses, the primary concern were the losses to the environment. The original sample holder had a thin wall and as such the losses to the environment could vary significantly from measurement to measurement depending on the external temperature. By significantly increasing the volume of material between the sample and the environment, the temperature difference between the two points is minimised.

In addition to the expanded cell walls, a joule heating calibration was performed using
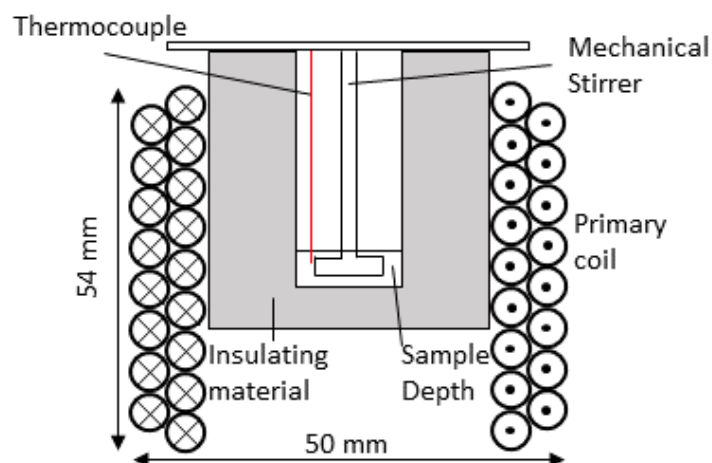
Figure 4.7: Schematic diagram of the modified Nanotherics Magnetherm system.

a bank of six 1 Ω resistors. These were placed into a sample cup containing 3 μl of deionised water. For six power values between 1.75 W and 0.5 W the temperature was measured as a function of time, the results of which are shown in figure 4.8. This allowed for precise comparisons to be made between the heating rate of measured fluids and that of defined wattages.

This measurement was completed once for each of the nanoparticle samples (Hyper-MAG A and C) as well as the polymer sphere samples. Based on the work Vallejo-Fernandez *et al* in 2013 [14], the expected heating from the immobilized particles should be approximately half that of the equivalent mobile particles.

For each sample, 3 ml of fluid was pipetted into the cup. The thermocouple and stirrer were positioned in the fluid, and set up within the coil. A datalogger was used to measure the temperature of the fluid every second for 300 s. The heating rate produced was compared to the initial slope of the joule calibrations in figure 4.8 to get a heating power in Watts. When this was completed the sample was removed and left to cool back to its starting temperature. This was to be repeated five times for each sample to confirm repeatability. The thermocouple, stirrer and cup were washed in de-ionised water between samples to prevent contamination.
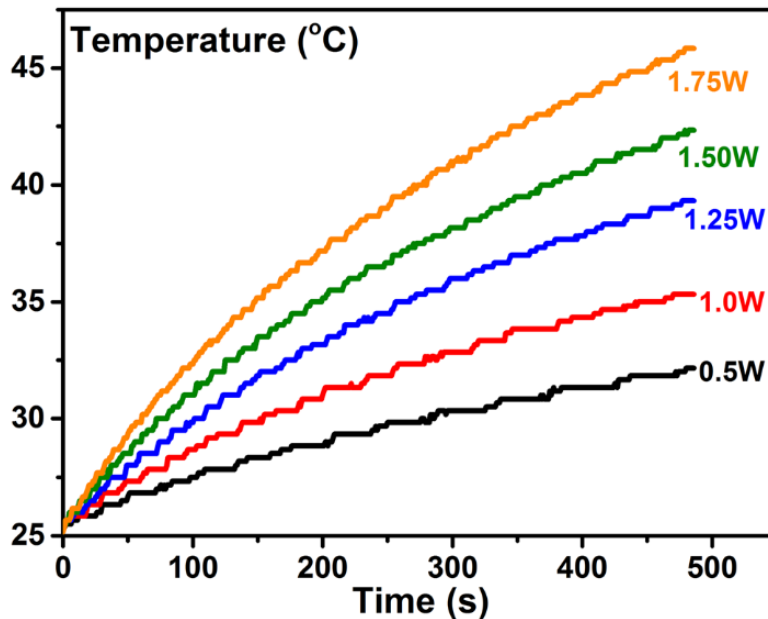
Figure 4.8: Joule heating rates for various wattages across six one ohm resistors in series, from Drayton *et al.* [80].

4.3.2   Hydrodynamic Size Distribution

Having completed a particle size analysis on the solid aspects of the particles using either the TEM or SEM, photon correlation spectroscopy (PCS) was used to find the distribution of the particles hydrodynamic volume V_h. Each of the particles is coated in dispersants to prevent aggregation (in this case oleic acid), which may also pull along some of the carrier liquid. As the particle attempts to rotate, the dispersant and captured carrier fluid will attempt to follow the particle. This increased volume is the hydrodynamic size, which is important for calculations of movement within the fluid. The hydrodynamic volume will vary greatly from particle to particle depending on the number of layers of dispersant and carrier liquid. This can vary further if aggregates have formed, creating a larger median hydrodynamic size than particle size.

The photon correlation spectroscopy was completed using a Malvern Instruments Zetasizer system. This work was completed by the author at Liquids Research Limited in Bangor. The process works by shining a monochromatic light source through a polariser, followed by the sample, followed by a second polariser. The nanoparticles and their dispersant coating will scatter the light, causing interference with

the scattering from other particles. This causes a "speckle" pattern of constructive and destructive interference. This pattern will change over time due to the particles undergoing Brownian motion. If the light source is pulsed, information about the particles movement can be calculated using the variation of speckle intensity over different pulses. At extremely short pulse intervals particles do not have time to move, so the correlation between two pulses is high. At longer pulse intervals the correlation decays at an exponential rate based on the diffusion coefficient. The sum of the exponential decays for each of the particles forms the autocorrelation function shown below, and is used to extract the required data.

$$g^1(q;\tau) = \int G(\Gamma) \exp(-\Gamma\tau)d\Gamma \qquad (4.8)$$

where q is the wave vector of the light source used, τ is the delay between pulses and Γ is the decay rate, given by equation 4.9.

$$\Gamma = q^2 D_t \qquad (4.9)$$

D_t in this case is the translational diffusion constant, which is used to determine the hydrodynamic size using the Stokes-Einstein equation. Rearranging for the hydrodynamic radius R_H gives

$$R_H = \frac{kT}{6\pi\mu D_t} \qquad (4.10)$$

This process was completed for each of the two nanoparticle sizes, but could not be completed for the immobilized nanoparticles as the polymer spheres are too large for the process to function.

The PCS is the final piece of commercially available equipment used in this work. This chapter has described each of the major pieces of equipment and explained how it was used and for what purpose. The next stage is to present the high frequency B-H looper along with its design and construction.

Chapter 5

B-H Looper Design and Construction

The primary aim of this project was the design and construction of a high frequency B-H looper. The system should be able to reach fields of above 400 Oe at a range of frequencies between 45 kHz and 120 kHz. These frequency and field values envelop those used by the systems currently in clinical trials.

Several designs for high frequency hysteresis systems have been published, including (but not limited to) S Slade *et al.* in 1996 [81], L Lacroix *et al.* in 2008 [82] and P Lenox *et al.* in 2017 [17]. These systems all follow a similar general form - a low turn, low inductance primary coil containing two sensing coils [16][83][84][85] to measure the sample signal and field value. The system described by P Lenox *et al.* in 2017 is shown in figure 5.1 as an example. The variations in these systems comes primarily in how they overcame the major limiting factors - coil heating, high frequency current requirements and field strength. These systems provided a good baseline to start the design for the looper described below. The common denominator for most of these systems is a low turn count (with the highest being 120 by V. Connord [16] and the lowest being 9 by E Garaio [86]), resulting in a large current being required to achieve the desired field given by:

$$H = \frac{\mu_0 I n_c A_c}{l_c} \tag{5.1}$$
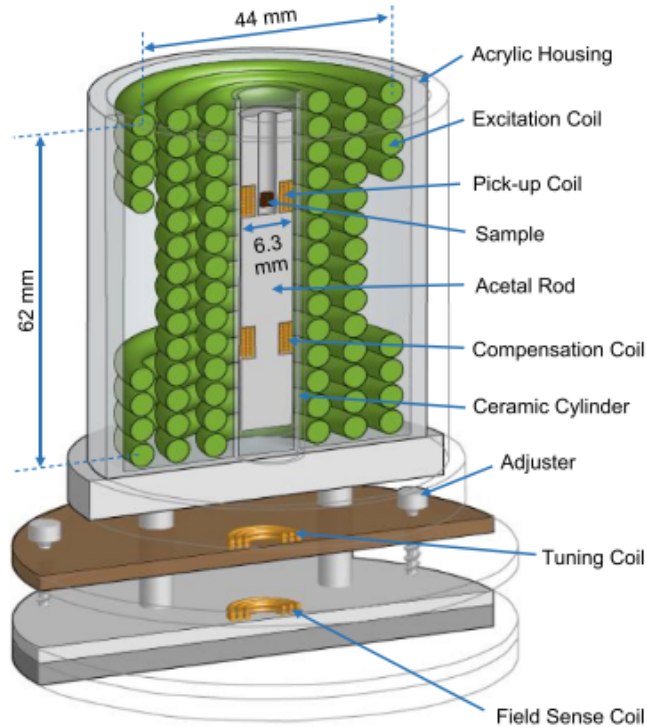
Figure 5.1: Schematic diagram of high frequency magnetic applicator described by P Lenox [17]

where n_c is the number of turns of the coil, A_c is the cross sectional area of the coil and l_c is the length of the coil. Using V Connord as an example, the 100 mm long system required 25 A of current to be driven at 95.4 kHz to reach the 460 Oe described in his paper. This has two consequences for the system, the first being that amplifiers that can reach such currents in AC are expensive and so a transformer may need to be included in the design, and secondly that such high currents cause substantial heating within the system.

5.1 Primary Coil

Initially two primary design routes were taken for the high frequency B-H looper. One was a solenoid design as described above, using an open air primary coil to drive the field in the sample space. The second was a novel "split coil" design based on using a large ferrite core inside the solenoid to focus the field into the sample space. The circuit design for driving the primary would be mostly unchanged, being formed

Figure 5.2: Schematic diagram of split coil B-H looper, with the main body made of soft ferrite and the shaded areas being the primary coils.

of an LCR circuit driven by an AC linear amplifier as described in section 5.2.

The aim of the split coil design was to reduce the current requirement of the system by using a horseshoe shaped core to focus the field into the sample space. An example schematic for this system can be seen in figure 5.2. The field would be generated by up to three sections of coil placed on the greyed out areas. This would be focussed through the core to the sample space in the "top" of the horseshoe. A hole drilled through the core in the right arm would allow for easy insertion of the sample without having to remove the sensing coils. For this system to work a suitably soft material in a bespoke design was required. Due to the high frequencies required standard magnetic cores such as iron or steel are not sufficiently soft. Soft ferrites, such as those used in transformers and radio antenna function at the required frequencies and so these were trialled. While the materials themselves were cheap, a bespoke design for the split coil setup was financially and temporally costly and so this setup was put on hold.

The solenoid setup was initially similar to Connord's design. A 140 mm coil comprised of 136 turns of 1 mm diameter wire, with an inner diameter of 25 mm. This required a current of 40 A to reach a field of 500 Oe, much like Connord's, but had a significantly larger sample space due to the longer primary coil. This initial system design was not possible as no amplifiers were available within budget that could reach

Figure 5.3: a) Heating rate of 25 mm diameter primary coil on PEEK former with 300 CFM fan b) Heating rate of 9 mm diameter carbon fibre former with 300 CFM fan.

both the frequency and the current required. The number of turns was doubled, resulting in a system which only required 20 A of current to reach the same field. A test system was built using a PEEK former that followed these specifications.

The second major problem to overcome was heating. As no extra insulation was used for the wires the system should not be raised above 45°C - beyond this the ceramic wire coating may break down. The PEEK former was tested using the DC power supply for a VSM and the temperature was taken as a function of time for 300 seconds or until the temperature reached 45°C for currents up to 10 A. The heating rates can be seen in figure 5.3a. For these the temperature of the external coil was measured while the current was applied, until either the cutoff temperature was reached (45 °c), 300 seconds had passed or the same temperature was measured for 10 consecutive seconds. The system was heating up far too rapidly, and was unlikely to be usable. Various layer numbers and currents were trialled to reduce this, but as the layer numbers increased so did the difficulty of cooling the inner layers. The penultimate cooling solution attempt resulted in a split copper coil former, with each of the end plates being water cooled to help cool the inner layers. The copper former was cut down the middle lengthways and a thin sheet of plastic placed between them to remove Eddy currents within the metal. This was combined with a 300 CFM Sanyo Denki 9GV1412P1G001 computer fan to cool the outside.

Given this was not sufficiently effective to reduce the heating, the primary coil was
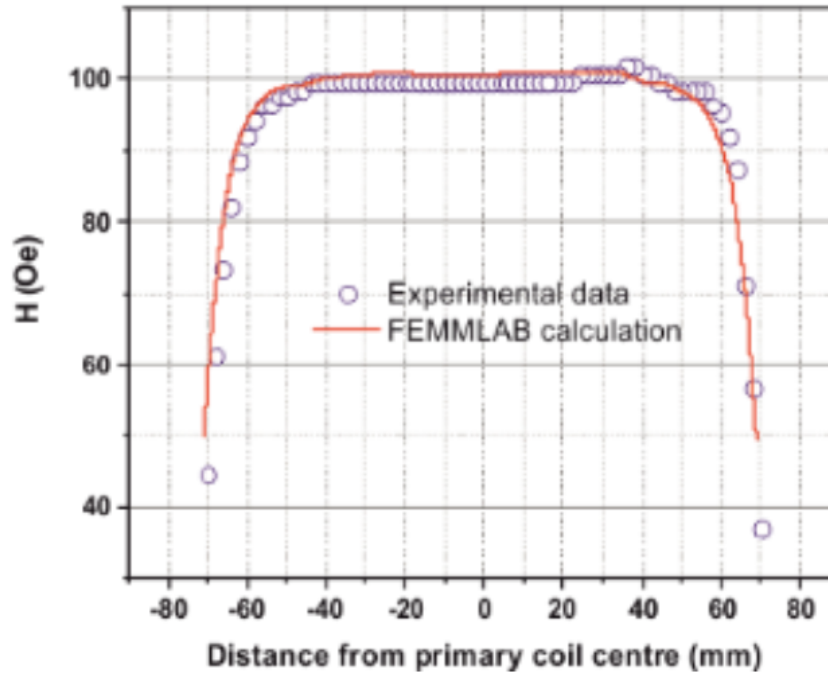
Figure 5.4: Field uniformity of primary coil from FEMMLab simulations and DC measurement.

redesigned. By cutting the diameter from 25 mm to 9 mm, the length of wire (and therefore resistance) was reduced by over half. This reduced the sample and secondary coil space, but allowed for higher currents at lower temperatures. The heating rate can be seen in figure 5.3b. The final setup was a three layer, 280 turn coil which could achieve fields of 27 Oersteds per amp. The field uniformity across the length of the coil was simulated using FEMMLab, a finite element simulation software and measured using a Hall probe mounted on a translating mount (figure 5.4). The uniformity was shown to not drop below 5% of the maximum for distances of 55 mm from the centre, and not drop below 10% of the maximum for distances of 60 mm.

The high frequencies achieved by the system required taking the skin effect into account. The skin effect describes the tendency of high frequency AC current to travel along the surface of a conductor as opposed to the bulk. An effective equation for skin depth δ (how much of the conductor used by the current in meters) is shown in equation 5.2.

$$\delta = \sqrt{\frac{2\rho}{(2\pi f)(\mu_0 \mu_r)}} \tag{5.2}$$

δ is the skin depth in meters, ρ is the resistivity of the conductor and μ_r is the variable permeability of the conductor. As the resistance of the wire is inversely proportional to its area, the effective resistance of the wire is dependent on the skin depth. Assuming copper wire is used ($\rho = 1.68 \times 10^{-8}$ Ωm, $\mu_r = 1$), the skin depth for a current driven at 200 kHz is 0.146 mm, and using a wire with a larger radius than this will give rapidly diminishing returns. Using the 280 turn coil as an example, a solid wire setup had a effective resistance of 0.4 Ω in DC, which was raised to 4.5 Ω at 150 kHz.

In the majority of systems mentioned above this problem is resolved using low turn count copper piping at high current. As only the surface of the conductor is used there is no need to keep the bulk of the material. The higher resistance per unit length is mitigated using fewer turns for the primary coil, the resulting loss in field strength is countered by significantly higher current values. As the primary coil is comprised of pipes, coolant can be passed through the primary coil to avoid overheating. This solution, while extremely tidy, was not possible in this case as high current value amplifiers at high frequency were outside of the budget.

The other solution was offered by V Connord's setup [16]. In this case Litz wires were used to comprise the primary coil. Litz wire is a continuous conductor comprised of a defined number of woven strands of wire. The strands are insulated from each other using a ceramic lacquer. As the strands are effectively singular the skin effect can be mitigated by ensuring the strands are of a sufficiently small thickness, while increasing the number of strands can change the resistance of the Litz wire as a whole. Using Litz wire allowed for higher turn counts without a significant increase in heating at higher frequencies. This system uses a 200 strand, 0.071 mm diameter Litz wire with a effective resistance of 0.46 Ω.

With a field of 27 Oe/A, over 15 A would still be required to reach the expected saturation point of 400 Oe. This would cause the primary coil to reach the higher temperatures too quickly. The proposed solution was the inclusion of ferrite cores as with the split coil design. Three manganese zinc (Fair-Rite Material 78 [87]) soft
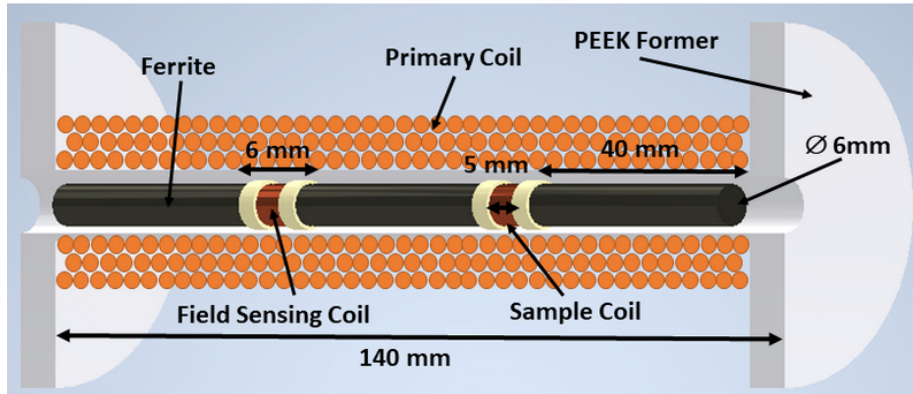
Figure 5.5: Schematic of primary coil setup with ferrite cores and secondary coils.

ferrite rods, 40 mm long and 6 mm wide, were simulated using FEMMLab software. These were placed on either side and between the sensing coils to maximise the signal. Varying the gap between the cores gave different maximum fields. The chosen separation, 6 mm, allowed for simulated fields of 450 Oe at 2.5 A of current, and measured fields (the process for which is described in section 5.3) of 415 Oe.

The inclusion of the ferrite rods increased the field per amp for the system by a factor 6, from 27 Oe/A to 165 Oe/A. The reduced current requirements allowed for a significantly longer run time for the primary coil when employing the computer fan. The ferrite cores did have some trade offs, which are discussed in section 5.5.

Based on the above, the final design for the primary coil is a 280 winding, three layer coil composed of 200 strand 0.071 mm Litz wire on a 140 mm long, 10 mm outer diameter polyether ether keytone (PEEK) former. Inside this former are three 40 mm by 6 mm ferrite rods and two 6 mm by 6 mm secondary coils which will be described in detail in section 5.3 below. A diagram for this setup can be seen in figure 5.5.

5.2   Primary Coil - Electronics

The initial specifications of the system defined the desired frequency range to be between 50 kHz and 120 kHz, a range including the commonly used frequency of 110 kHz [80]. As with previous systems a resonant circuit was used to drive the primary

Figure 5.6: Capacitor bank of six sets of six 3.28 nF capacitors in series with a total capacitance of 10.98 nF, used for 62 kHz frequency.

coil. The resonant circuit was a simple inductor-capacitor-resistor (LCR) circuit powered by a high frequency amplifier (Dr. Hubert A1110-16-E). The resonant frequency f_r of an LCR circuit is defined by the capacitance C of the capacitors used and the inductance L of the coil or inductor. This can be calculated using equation 5.3 below;

$$f_r = \frac{1}{2\pi\sqrt{CL}} \tag{5.3}$$

In this case the inductance was higher than previous systems due to the increased turn count and inclusion of the ferrite cores. The coil's inductance without the ferrites was measured to be 86 μH and 660 μH with the ferrites. This has two noticeable effects on the system currently. The first effect is a smaller capacitance value for each defined frequency. As an example, the capacitance required for a 70 kHz resonance with the ferrites is 8.9 nF, or 89 nF without the ferrite cores. The second effect is an increased power requirement from the amplifier, and as such an increased voltage across the capacitor-inductor gap.

Operating Frequency (kHz)	Capacitance required (nF)
47	17.6
62	11.0
74	7.0
89	4.9
111	3.1

Table 5.1: Table of capacitances for required operating frequencies

Rather than single capacitors for each of the required frequencies, capacitor banks were fabricated. A combination of series and parallel wired capacitors allowed for a higher precision of total capacitance, as well as solving problems caused by the increased voltage across the capacitor-inductor gap. Spreading the increased voltage load across several sets of capacitors in parallel reduces the maximum for any individual capacitor. Using this setup running at 2.5 A, 62 kHz as an example, a single capacitor would result in a voltage drop of just under 600 V. Using the bank shown in figure 5.6 each capacitor only receives a voltage of around 99 V. Not only does this reduce the risk of damage to the capacitors, but it also reduces the heating the capacitors experience due to power losses across the board. With too few capacitors the high wattage can cause the capacitors to heat up, resulting in a variance in the capacitance and therefore the resonance frequency. A table of the capacitances of the constructed banks and their equivalent resonance frequencies can be seen in table 5.1.

5.3 Secondary Coils

As with previous systems, a pair of sensing coils were used to measure the magnetisation of the sample. The secondary coils have an induced EMF ϵ based on the variation of the field in time as shown in equation 5.4. In an ideal case two identical coils wired in opposition will have a summed ϵ of zero. When a magnetic sample is inserted into one of these coils its inductance will change, and as such the summed ϵ will vary. The now non-zero summed ϵ of the opposed coils will be purely due to the effect of the sample.
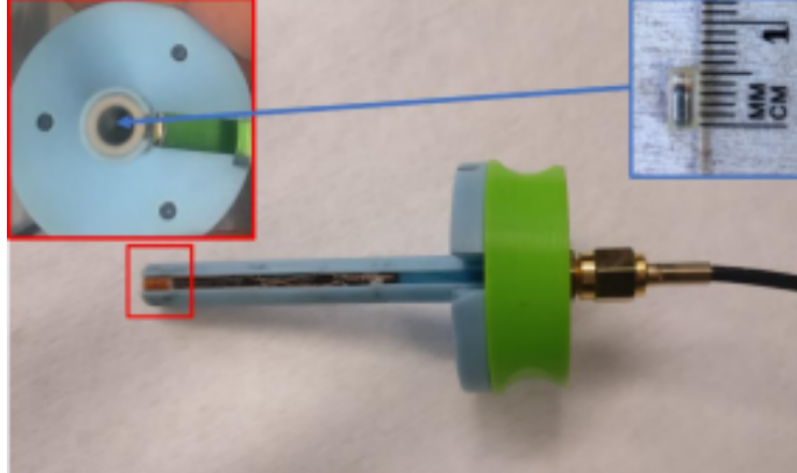
Figure 5.7: Image of a secondary coil with a 40 mm ferrite core and former. Inset is an image of the sample space.

$$\epsilon = -N\frac{\delta\phi}{\delta t} \tag{5.4}$$

Due to the required spacing of the ferrite rods the space for the secondary coils was limited to 6 mm. The design used for the formers used a 6 mm former with an inset 0.5 mm deep 0.5 mm from the outside edges. The inset allowed for a coil 5 mm long and 0.5 mm high should multiple layers be needed. Initially a high turn count was used to mitigate the low expected sample volume however this was discovered to be unnecessary. The coils used for the sample were comprised of 39 turn, two layer coils of 0.25 mm diameter copper wire. These produce a signal of approximately 80 V at 47 kHz, 2.50 A when in isolation. An image of the secondary coil, former and ferrite can be seen in figure 5.7.

With the coils complete, the next stage was to measure the field in the sample space. Given both the high frequency and limited access to the sample space a Hall probe could not be used. A field sensing coil was constructed to calibrate against a Hall probe in DC. An additional sensing coil was constructed with a 155 turn count. This increased turn count was required for the measurement of induced ϵ at DC or 70 Hz frequencies.

The standard equation for the field measured by a sensing coil is given in equation 5.5 below

$$B = \frac{\phi}{\mu_0 n_c A_c} \tag{5.5}$$

where n_c is the turn count of the coil and A_c is the cross sectional area of the secondary coil. There are several adjustments to make to this for use in the field calibration. The first and simplest is conversion from SI to CGS, using a multiplier of $\mu_0 10^8$.

$$B = \frac{10^8 \phi}{n_c A_c} \tag{5.6}$$

Secondly, as the measured output of the coil is an ϵ in volts, the equation needs to take Faraday's law into account. Substituting ϕ with an ϵ that has been integrated with respect to time allows for a voltage input.

$$B = \frac{10^8}{n_c A_c} \int \epsilon dt \tag{5.7}$$

The final addition is a form factor f_f for the coil. The higher winding count on the coil has ensured it was less and less likely to be perfectly wound, resulting in a drop off in expected signal. The form factor is a proportion of the expected signal that is lost to mis-windings, with a value between one and zero where one is a perfectly wound coil with no unexpected losses. This can be calculated by the ratio of the field measured by the coil and the expected field H_{ex}, either measured by a precalibrated source such as a Hall probe or from a known field source

$$f_f = \frac{10^8}{H_{ex}} \frac{1}{n_c A_c} \int \epsilon dt \tag{5.8}$$

To calculate the form factor the field of the primary coil without the ferrites was measured at five different currents at 70 Hz using a Hall probe and the uncalibrated field sensing coil. For each current value a form factor was calculated for the coil, and these were then averaged to give a form factor of (0.70±0.05). This was then checked at high frequencies with the ferrites (62 kHz) and without the ferrites (149 kHz). As each of the terms before the integral is constant they can be combined into

a single calibration factor σ_c, defined in equation 5.9.

$$\sigma_c = \frac{10^8}{H_{ex}} \frac{1}{n_c A_c} \tag{5.9}$$

For the 155 turn coil this calibration factor was measured to be $(3.2\pm0.2)\text{x}10^{-8}$ VsOe^{-1}. To confirm the calibration the 155 turn coil was used to measure the output of the field for comparison to the finite element software FEMMLab, as mentioned previously. The field was generated by a 4 A current at 70 Hz, which the 155 turn coil measured as 643 Oe across the sample space enclosed by ferrites. The FEMMLab simulation for the field defines the average field across the 6 mm gap between ferrites as 638 Oe, with a standard deviation of 29 Oe (4.5%). The samples used only use the central 4 mm of the 6 mm gap due to the demagnetising field which will be discussed in detail later in this section. As such the field amplitude experienced by the sample is 619 Oe, with a standard deviation of 13 Oe. The field uniformity deviates by approximately 2% across the sample space. This calibration factor was used to measure the field values shown in figure 5.8.

At higher currents there is a noticeable break from the linear behaviour expected between the field and the current. This is due to the ferrite cores saturating. As the domains inside the cores approach maximum alignment their field amplification drops off. Additional current applied to the core will return to following the non-amplified field/current ratio of 27 Oe/A as described in section 5.1.

As mentioned above, the sample space was limited by how close the ferrite rods needed to be to maintain field. The sensing coils measure a space 5 mm long and 5 mm across. Two further factors had to be considered, minimising the demagnetising field H_D while maximising the sample volume to ensure a reasonable signal to noise ratio. The demagnetizing field for the sample is dependant on the aspect ratio as discussed in section 2. This variation can be seen for figure 5.9 for one of the samples used in this work, using equation 2.8.

An aspect ratio of 3:1 (4 mm long, 1.3 mm wide) was chosen as a compromise between the sample space, demagnetizing field and sample volume. This aspect ratio permits a 4 mm long sample which will fit comfortably within the 5 mm sensing coil when the adhesive seal is taken into account. The 3:1 aspect ratio gives a demagnetizing
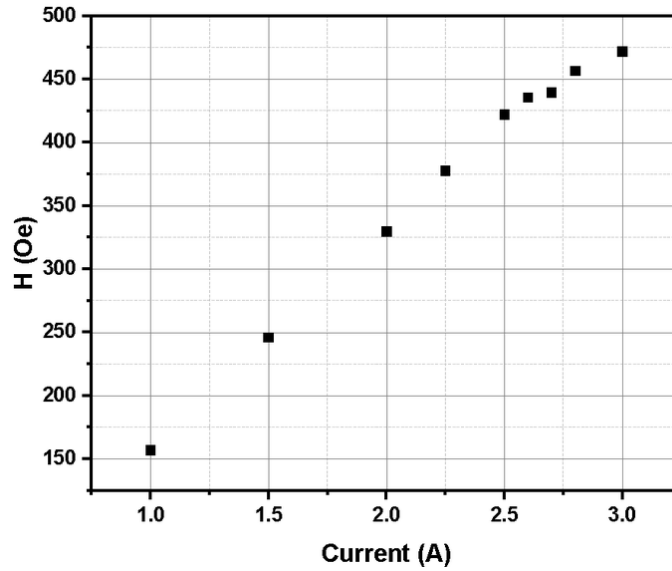
Figure 5.8: Field measured using calibrated 155 turn sensing coil as a function of operating current.
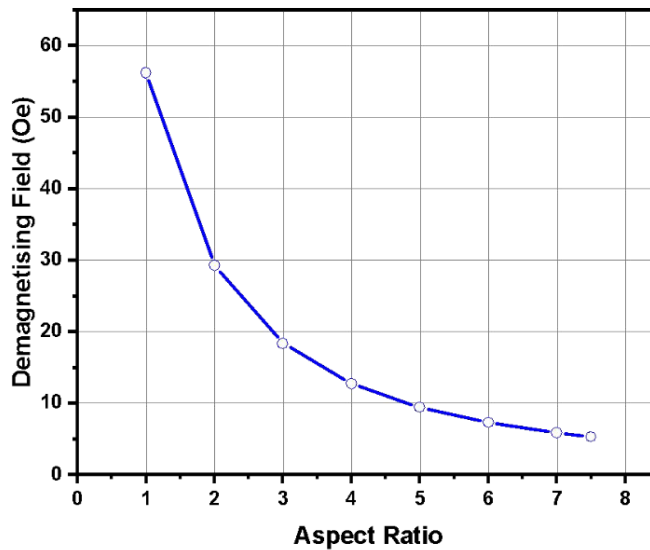
Figure 5.9: The demagnetizing field H_D as a function of the aspect ratio for a suspension of magnetite nanoparticles dispersed in water with a concentration of 13.4 G.

field of 4% and a sample volume of 7 μl. Increasing the aspect ratio to 4:1 (4 mm long and 1 mm wide) would decrease the demagnetizing field to 3% but halve the sample volume to 3 μl with a similar drop in the signal-to-noise ratio. As such the samples were made using a 5 mm long piece of silicone tubing with a 1.3 mm internal diameter. The tube was sealed at one end using a silicone cement. 7 μl of fluid was added using a Fisherbrand Elite adjustable volume pipette (2-20 μl $\pm$0.1 μl with 0.02 μl increments) before the other end was sealed using the same silicone cement.

5.4   Sensing Coil - Electronics

With the secondary coils designed the next stage was to correctly measure their output. Signal balancing was required to ensure that the final output signal of the setup was purely a sample signal not contaminated by differences in the coils or defects in the ferrite rods.

Initial thought on coil balancing was to place the two coils in series opposition, as is commonly the case with AC susceptometers and some other systems worldwide [16][83]. As the coils are counterwound, the signal from the field sensing coil sums with the equal and opposite sample coil signal to create a zero value for all fields. When the sample is inserted the signal output of the sample coil is altered by the change in inductance, and the resulting signal is purely that of the sample. This, however, requires the sensing coils to be near identical as any differences in phase or amplitude of the signal cannot be accounted for. During testing of this setup using the coils described in section 5.3, a phase difference of up to 20° was noticed leading to a null signal of up to 140 mV in a 300 Oe field. The sample signal for the same setup was measured to be 310 mV, giving a signal-to-noise ratio of just over 2.

Given the coils are only 38 turns, the cause of the phase and amplitude difference are unclear. However it made it clear that a system was needed to alter the output of the field sensing coil to more accurately match that of the sample coil. Two solutions were initially trialled, electronic and digital balancing. In the case of electronic balancing the amplitude and phase of the field sensing coil was adjusted manually using variable resistors to adjust the gain of a series of buffer amplifiers. This will be described in more detail in section 5.4.4. Digital balancing employed the mathematics functions

available within the oscilloscope software, described in section 5.4.2.

5.4.1   Electronic Balancing

The electronic balancing setup was designed to allow the variation of the phase and amplitude of the field sensing coil so as to properly align with that of the sample coil. Examples of automatic electronic balancing setups for AC susceptometer systems have been defined [88] using the driving signal for the primary coil as a guide with which to shift the secondary signals. However the higher voltage in both the primary circuit and output of the secondary coils lead this to be considered unsuitable. As such a manual system was constructed using a three stage circuit.

The balancing circuit was a three stage setup using a variable phase shifter described on page 89 of The Art of Electronics by Horowitz and Hill [89]. A variable resistor allowed for manual real time shifting of the field sensing coil signal to match that of the sample coil signal by up to 180^0. A slight adjustment to this added a small gain of 1.5x. The gain allowed for the second part, a variable potential divider, to reduce the amplitude back down to that of the sample coil signal. Finally a differential amplifier was constructed to output the difference between the two signals. Additional buffer amplifiers were placed throughout to prevent signal feedback. A schematic for this setup and a comparison of the null and sample signals are shown in figure 5.10.

While the null output was better than that of purely opposed coils, several issues with this system led to it being passed up in favour of digital balancing. The primary concern was the amplitude of the sample signal. As mentioned in section 5.3 the output of a single coil could be as high as 80 V. This would cause serious damage to the operational amplifiers that were not rated to higher voltages, which required equivalent power inputs. The secondary coil output signals could be attenuated, however this would also attenuate the sample signal which is already small in comparison to the raw output.

The second major issue was the system being required to stay on while the balancing was completed. While the coil heating was less of an issue due to the low currents the ferrites would still warm slightly due to hysteretic heating and eddy currents within the cores as mentioned in section 5.1. This would cause variations in the field
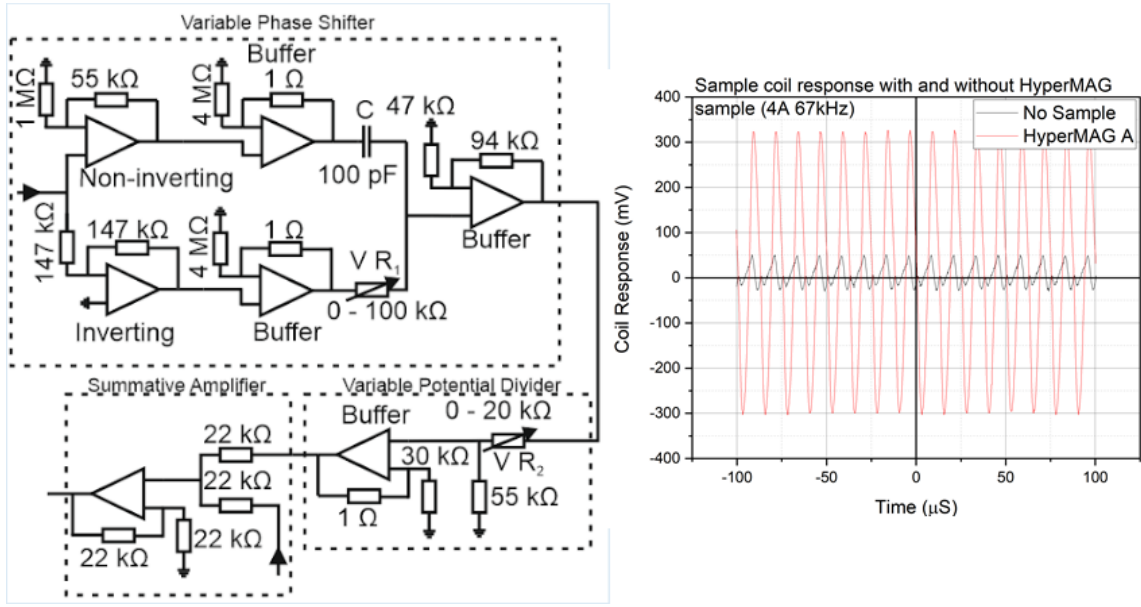
Figure 5.10: Schematic diagram for complete balancing setup (a) and comparison between null signal (black) and sample signal (red) for HyperMAG A ferrofluid (b).

or heating of the sample itself.

5.4.2 Digital balancing

A further two techniques were trialled within the oscilloscope (PicoScope 3000 series) software for balancing the signal. The first was completing the same steps as the digital balancing within the software - adjusting the phase and amplitude of the field sensing coil manually and subtracting one from the other to get the sample signal. This had similar issues to the electronic balancing as the raw output of the signal required attenuation to be suitable for the scope as well as the system needing to be on to see the adjustments. The null signal was also higher than the digital balancing at as high as 500 mV at the higher frequencies.

The second technique used the software's ability to save a signal as a reference waveform and apply functions to these saved signals. In this case, the coils were wired in opposition and the measured output was saved as a reference. The system could then be turned off, reducing heating issues, while the rest of the balancing was completed. The difference between the reference signal and the opposed signal would be measured in a different channel (line A in figure 5.11).
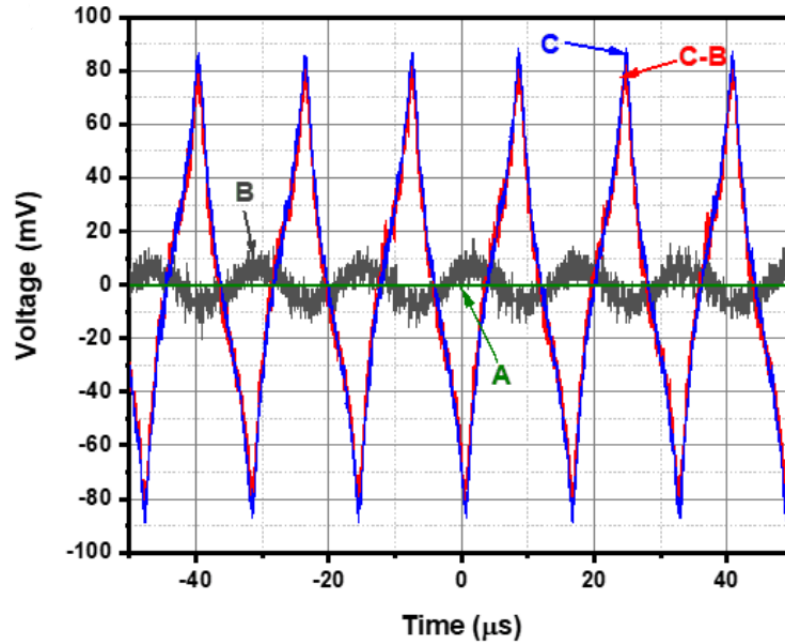
Figure 5.11: Example of digital balancing.

As the coil mount would be placed slightly differently each time it was added or removed, this null signal of effectively zero was inaccurate. The sample coil was added and removed a couple of times and the effective null was re-measured (line B). With the null recorded, the sample could be inserted into the sample coil. The recorded null signal could then be removed from the sample signal (line C) to give the sample output (line C-B). This technique allowed for minimising the time in which the system was on, while also having a suitably small signal to noise ratio (3x at the highest frequency and field).

5.4.3   Additional Effects of the Ferrite Cores

The ferrite cores did come with some downsides as mentioned in section 5.2. Prolonged use of the ferrite cores causes them to heat up independently of the primary coil due to hysteretic heating and eddy currents within the material. Changes of temperature affects the maximum flux density of the material drastically, with a loss of 200 G from 25^0C to 30^0C as shown in figure 5.12 from the Fair-Rite material 78 datasheet. The result of this could be seen in the output of the field sensing coil, with measurements at different core temperatures resulting in differing outputs as
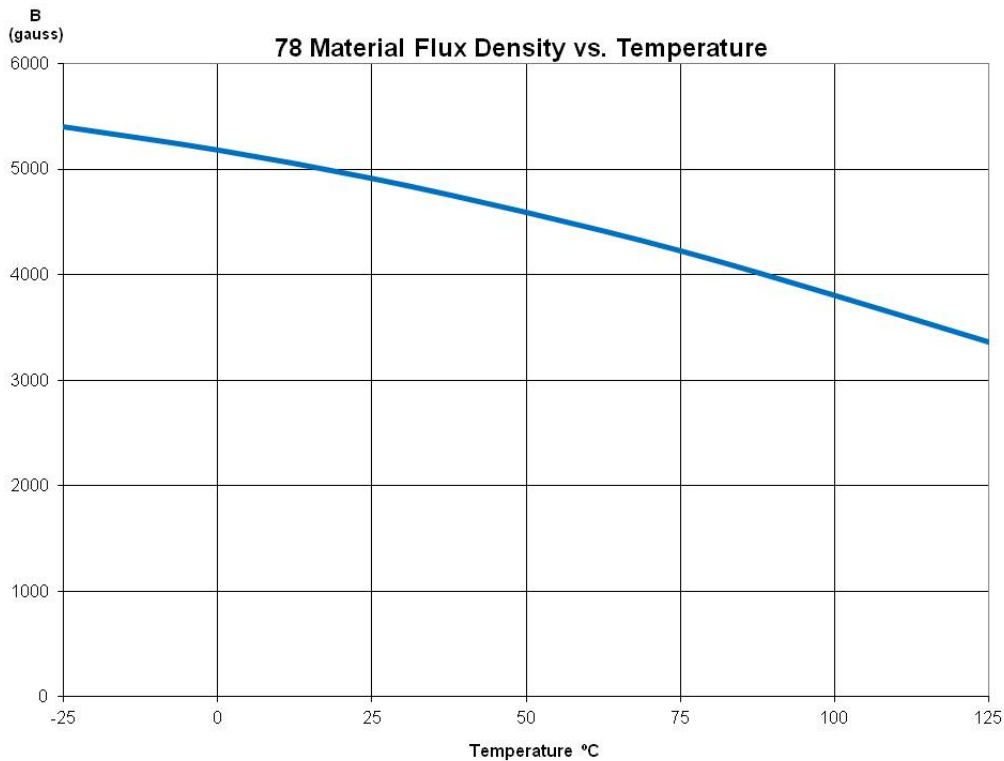
Figure 5.12: Flux density of Fair-Rite Material 78 as a function of temperature, from the datasheet [87].

can be seen in figure 5.13.

The placement of the cores within the primary coil prevented easy access with air or other cooling systems (figure 5.4). The central core in particular was inaccessible without removing it or the coils. As such the simple solution was to minimise the time in which the system was on to reduce the heating, and allow adequate time between measurements to allow the cores to cool. The required cooling time is dependant on the field and frequency of operation. Fields of less than 150 Oe required cooling time is a minute or lower, reaching a 30 minute cooling time for fields higher than 350 Oe.

An additional problem that arises at higher frequencies and fields is the appearance of higher order harmonics in the null and sample signals. Figure 5.14 is an FFT (fast fourier transform) of a sample signal measured at 320 Oe, 111 kHz. Harmonic peaks appear at odd integers of the measurement frequency. While they are present at all measurement frequencies (figure 5.15A) the amplitude is only high enough to affect sample signals at high fields (above 300 Oe) and/or at the higher frequencies

95
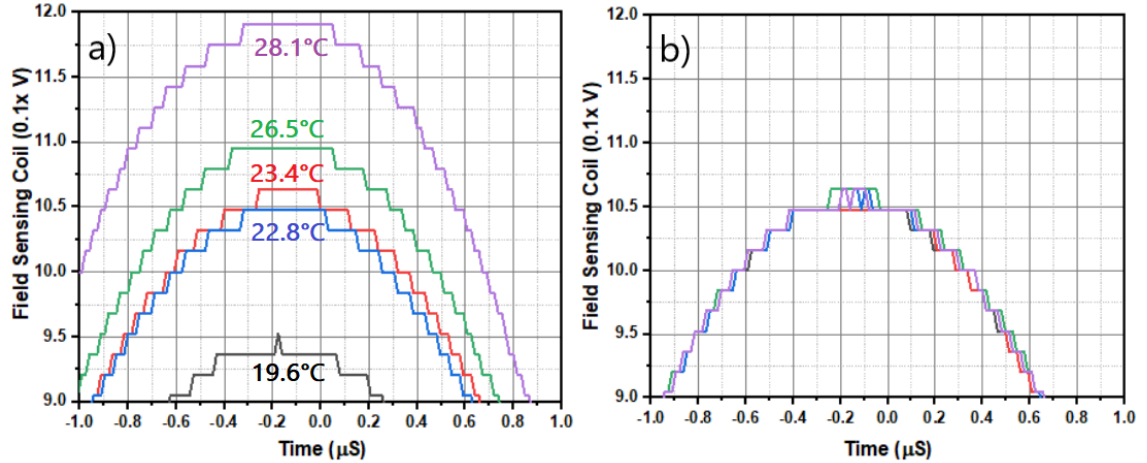
Figure 5.13: Peak of the field sensing coil output with a) different ferrite core temperatures and b) similar core temperatures.

(89 kHz and above). In most cases the harmonic signal is uniform and visible in both the sample and null signals, taking multiple measurements and averaging the null and sample signals removes the harmonics. An example of this can be seen in figure 5.15B.

For the higher frequencies there may be some remanent aspects of the harmonics. In this case a low pass filter is employed in the analysis stage, at a value of 1.5x the measurement frequency. This is shown in figure 5.15C.

As a result, the signal-to-noise ratio varies with the frequency of operation, with a SNR of 8 at the lower frequencies and 3 at the higher frequencies. This variance is shown in figure 5.16. Although the SNR drops significantly over the frequency range, at the higher frequencies it is in line with ratios presented by other systems [86]. As an example, the system presented by V. Connord provides a SNR of 3x at 55 kHz but does not define its variation over other frequencies [16].

5.5   Measurement Procedure

With the balancing setup completed, a description of the measurement procedure for the setup is as follows. An image of the full setup can be seen in figure 5.17.
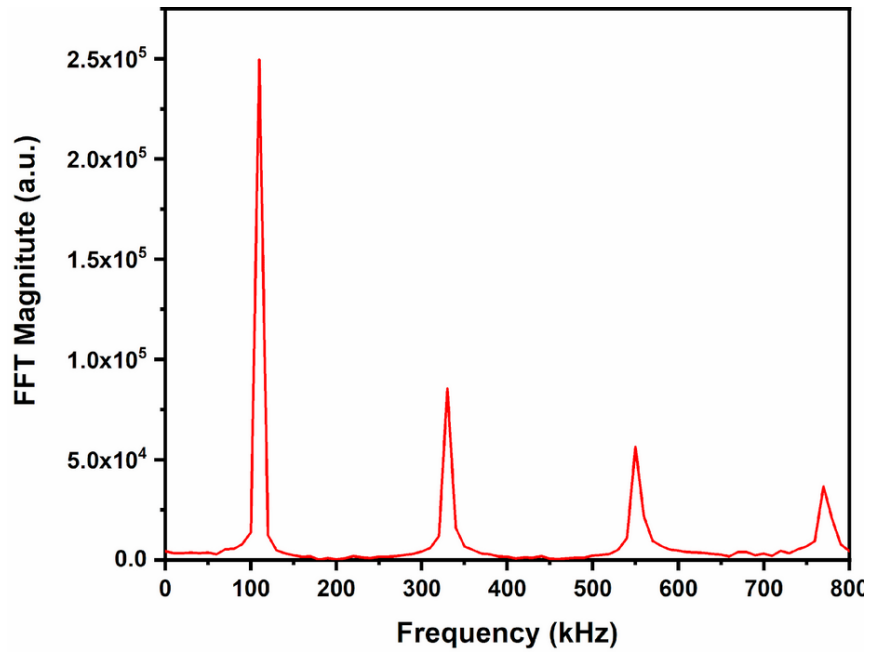
Figure 5.14: Fast fourier transform of sample signal at 320 Oe, 111 kHz. Harmonic peaks at 333 kHz, 555 kHz and 777 kHz are observed.
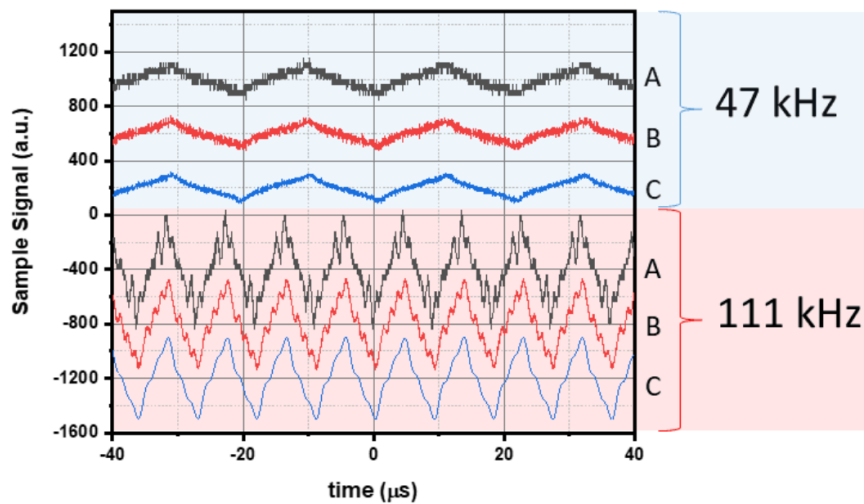
Figure 5.15: Sample signals at 320 Oe for 47 kHz and 111 kHz. In both cases, A is a single sample signal, B is the signal averaged 5 times, and C is the averaged signal passed through a low pass filter.
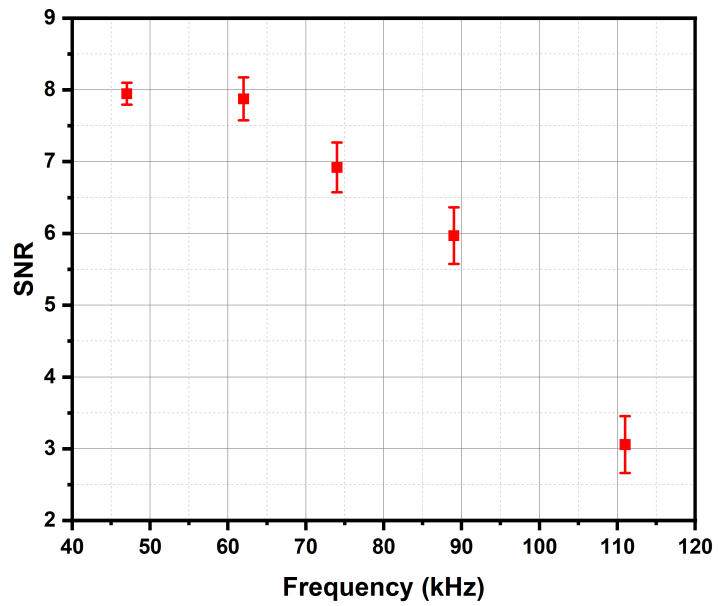
Figure 5.16: Signal-to-noise ratio for each used frequency of the B-H looper for a HyperMAG C sample measured at 400 Oe.
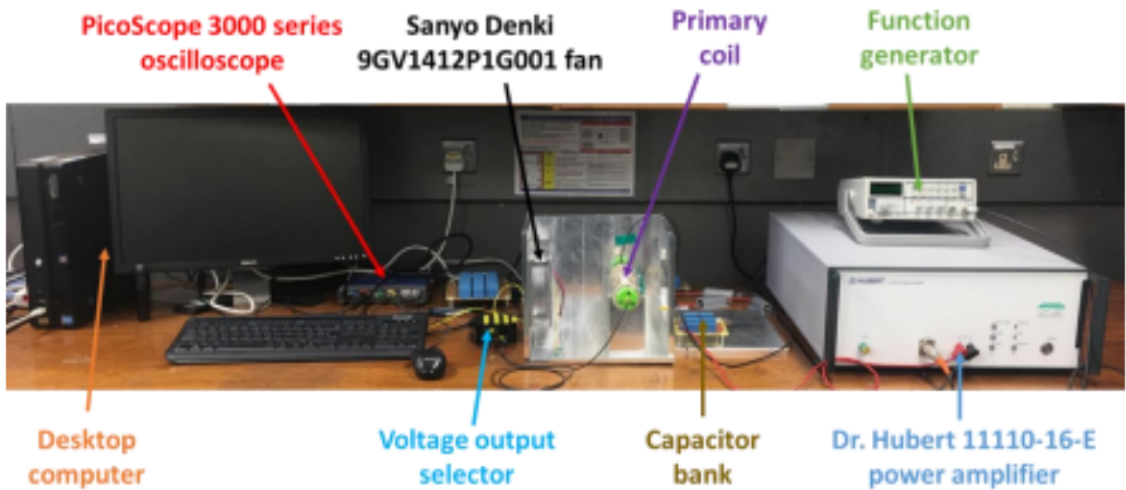
Figure 5.17: Image of full setup for the B-H looper system.

The sample was made using a 5 mm long 1.3 mm internal diameter silicone tube. One end is sealed using a silicone cement. Once dry, 7 μl of sample fluid is inserted using an Eppendorf micropipette. The other end is then sealed using the silicone cement.

With the sample prepared, the capacitor bank for the chosen frequency is connected. The frequency of the signal generator is varied to confirm the system is at resonance after which the field is brought to the desired value.

With the primary coil set up, the opposed signal can be measured across the oscilloscope. This should be saved as a reference, and a mathematics function set up to remove it from the opposed output resulting in the null signal (figure 5.11 line A). The empty sample coil is removed and reinserted into the primary coil and the new null signal measured (figure 5.11 line B). The sample coil is removed again, the sample is placed inside after which the coil is reinserted. The sample signal (figure 5.11 line C) is saved. The output of the field sensing coil by itself is also saved to confirm the ferrites are stable and to be used to generate the field axis. The whole process up until this point is repeated four additional times to confirm repeatability.

Once all of the sample, null and field data has been collected it must be converted from voltages to field and magnetizations. As with the field sensing coil calibration the average ϵ for the field is integrated with respect to time. Generally the integrated output has a clear slope, which is removed by applying equation 5.10 below.

$$y' = y - (-m)x \tag{5.10}$$

where y' is the slope adjusted signal, y is the original signal, m is the slope to be removed and x is the x-axis, in this case the time. With this completed the only major change is using the calibration factor σ_c to adjust the amplitude from VS to Oe.

The averaged and null removed sample signal goes through the same process without the calibration factor - if the harmonics are still visible after the null subtraction the low-pass filter is applied. The sample signal is then plotted as a function of the calibrated field from above to form the hysteresis loops. An example of these loops
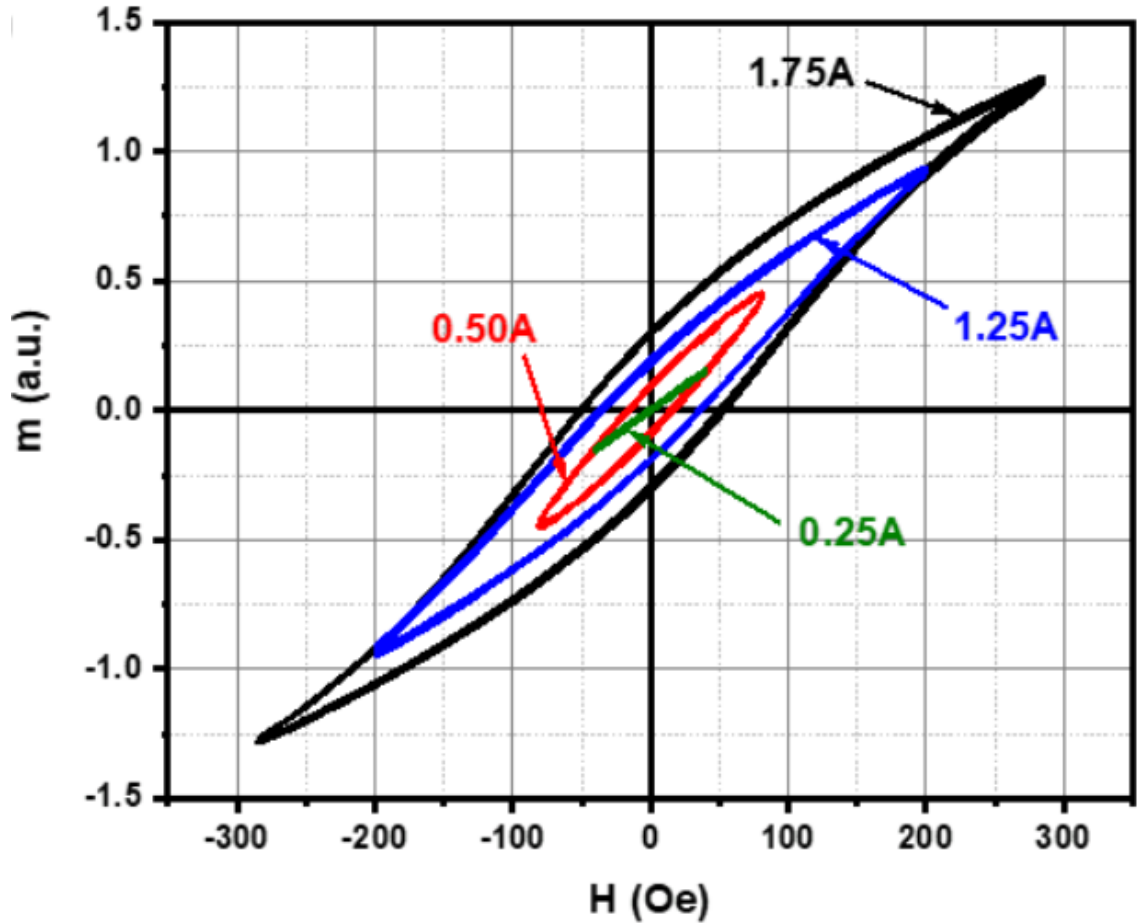
Figure 5.18: Hysteresis loops of 7 μl HyperMAG A measured at 40, 80, 200 and 280 Oe using a driving frequency of 47 kHz.

at four fields at 47 kHz are shown in figure 5.18. These loops were measured using 7 μl of HyperMAG A fluid. Fields beyond 280 Oe at this frequency give a higher value of m, but no further increase in coercivity which will be discussed further in chapter 7.

Overall, the B-H looper presented in this study holds several advantages over other systems. The use of the ferrite cores reduces the current requirements by an order of magnitude over other systems, with no major cooling requirements. A sample volume of 7 μl provides a signal to noise ratio of up to 8 at lower frequencies, 3 at higher. The lower value of signal to noise still outclasses other systems, with M. Raspaud providing a signal-to-noise ratio of 2. The comparatively low current requirements also allow for much less aggressive cooling and reduce the cost of the device considerably.

With the B-H looper functional the next chapter is the preliminary magnetic and physical characterisations. These cover most of the equipment and processes described in chapter 4. The primary areas of interest are the physical and hydrodynamic size distributions of the particles as well as the distribution of anisotropy constants. High frequency characterisations using both the B-H looper and the Magnetherm system are completed in chapter 7.

Chapter 6

Characterisation of Magnetic Nanoparticles

6.1 Particle Size Analysis

The particle size analysis for the HyperMAG A and C samples was completed as described in chapter 4. Figure 6.1 shows bright field (a and b), HRTEM (c and d) and diffraction pattern (e and f) images of HyperMAG A and C taken using the JEOL JEM-2011 TEM described in section 4.2.1. The near full completed rings in images e) and f) show the random orientation of the particles - a single crystal would show a single spot for each of the ring diameters visible. The diameters of each of the rings can be measured to give a d-spacing which corresponds to a known crystal direction, denoted by Miller indices.

Using the image manipulation software ImageJ [79], the diameter of the rings in images e) and f) of figure 6.1 were measured. This gives a diameter in reciprocal space, which was halved to give a reciprocal radius before being inverted for a radius. These radii were compared to the known lattice spacings provided by Joint Committee on Powder Diffraction Standards (JCPDS). The card number for magnetite is JCPDS 75-0033. This gives the known Miller indicies of magnetite and their radii. A comparison of the measured radii in nm and their Miller indices is shown in table 6.1.
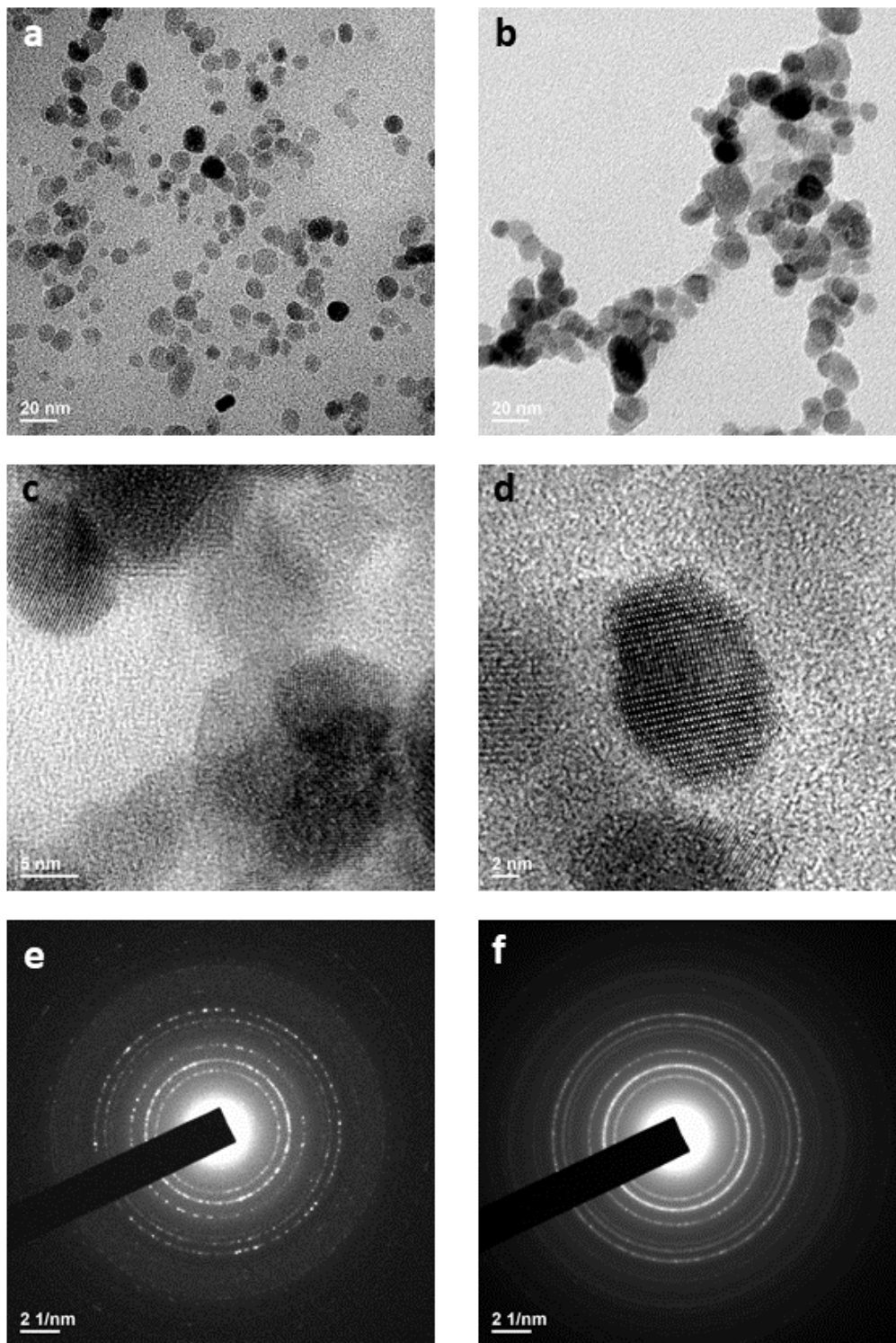
Figure 6.1: general results of TEM imaging for HyperMAG A and C.

HyperMAG A Diffraction Pattern Radius (nm)	HyperMAG C Diffraction Pattern Radius (nm)	<hkl>	JCPDS Values Radius (nm)
0.493	0.474	111	0.483
0.284	0.307	220	0.296
0.246	0.255	311	0.252
0.244	0.243	222	0.241
0.146	0.144	400	0.148

Table 6.1: The radii for each of the diffraction pattern rings shown in figure 6.1, with their corresponding values and Miller indices from the Joint Committee on Powder Diffraction.

The particle size distributions were completed using the Zeiss Particle Size analyser described in section 4.2.3. For each sample 500 particles were measured to ensure an accurate calculation of σ. The particle sizes were binned, and the distribution was normalised to the total volume of particles measured f(D). The median diameter D_m was calculated through the lognormal equation below

$$D_m = \exp\left[\frac{\sum(N_D \ln(D))}{N_T}\right] \tag{6.1}$$

where N_D is the number of particles with diameter D, and N_T is the total number of particles in the distribution. The standard distribution σ was calculated using the mean of the squared values of diameter $((\bar{X}^2))$ and the square of the mean of the diameter $((\bar{X})^2))$ as shown in equation 6.2.

$$\sigma = \sqrt{(\bar{X}^2) - (\bar{X})^2} \tag{6.2}$$

Figure 6.2 shows the particle size distributions for HyperMAG A and C, with the calculated values of D_m and σ. These are 10.9 nm with a standard deviation of 0.27 for HyperMAG A, 12.3 nm with a standard deviation of 0.23 for HyperMAG C. These are much closer in size to the sizes quoted by Liquids Research, which are given as 10.3 nm and 15.2 nm for A and C respectively [18]. While the particle diameters are much closer than expected the volume is the more relevant metric.
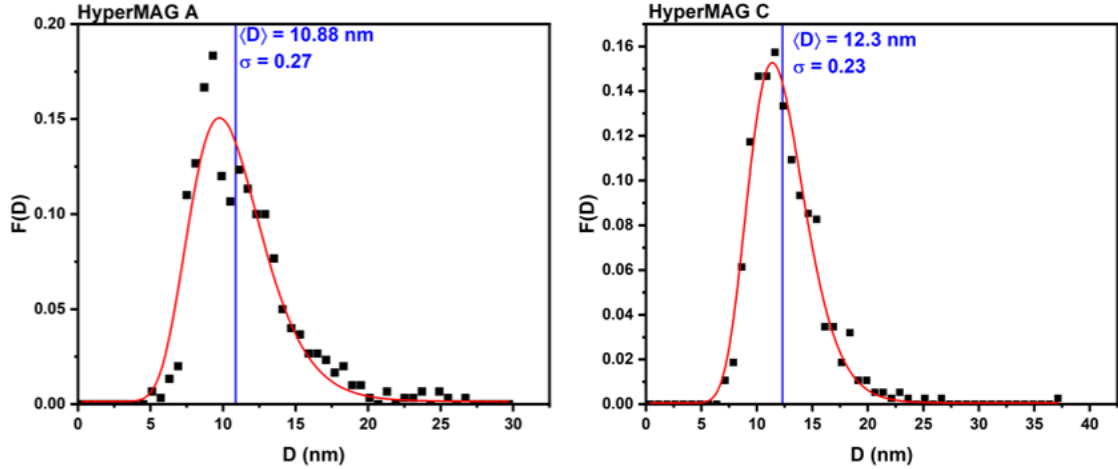
Figure 6.2: Particle size distributions for HyperMAG A and HyperMAG C. The red line is a lognormal fit.

These diameters give a median particle volume of 5400 nm^3 for HyperMAG A and 7800 nm^3 for HyperMAG C.

The polymer sphere sample was imaged using the JEOL 7800F Prime SEM described in section 4.2.2. The same process was used to measure the sphere diameters and the distribution as above. An image of the polymer spheres and the size distribution can be seen in figure 6.3. The measured polymer sphere size is 310 nm with a standard distribution of 0.58. Aggregation is not a concern with the spheres and so they are not coated in surfactant. As such the hydrodynamic size can be assumed to be the same as the physical size. A particle size of 310 nm gives a Brownian relaxation time τ_B in the region of 80 ms seconds. This should be immobile at frequencies used by both the B-H looper and clinical trials.

In addition, the hydrodynamic size for the particles was measured using Proton Correlation Spectroscopy. The analysis for this was completed in the software of the Zetasizer system used. The distributions can be seen in figure 6.4. The median hydrodynamic diameter was measured to be 66.7 nm, standard deviation of 0.19 for HyperMAG A and 89.9 nm, standard of 0.17 for HyperMAG C. These are smaller than the quoted 100 nm for both HyperMAG A and C [90]. The quoted hydrodynamic size would give a τ_B of 3 ms, compared to the calculated values of 0.1 ms for HyperMAG A and 1 ms for HyperMAG C. This relaxation time is significantly higher than for the physical nanoparticle sizes which are at the μs scale. Comparisons of τ_B can be seen in table 6.2.

105
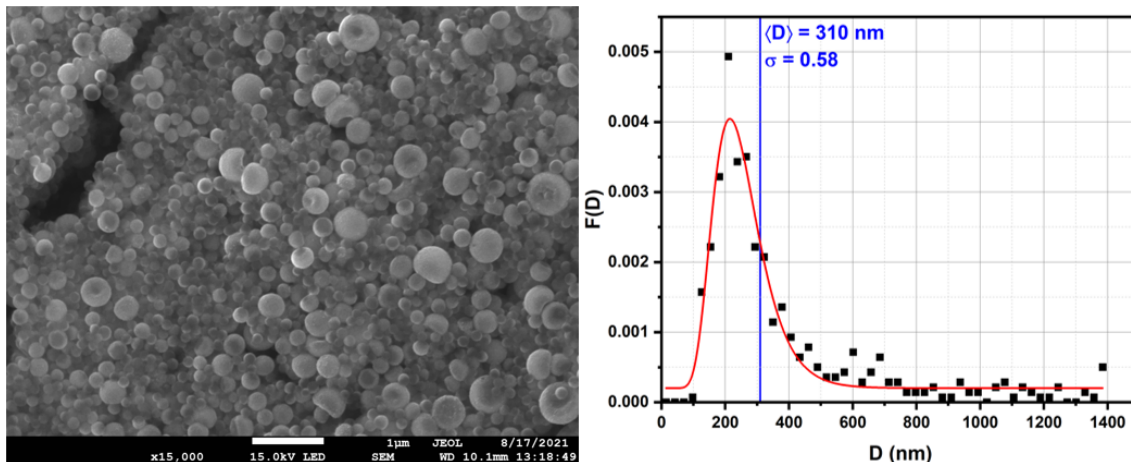
Figure 6.3: SEM image of the polymer spheres and a particle size distribution of the spheres with median diameter and standard deviation.

Sample	Physical Size <D> nm	σ	τ_B	Hydrodynamic size nm	σ	τ_B
HyperMAG A	10.9	0.27	10^{-6}	66.7	0.19	10^{-4}
HyperMAG C	12.3	0.23	10^{-6}	89.9	0.17	10^{-3}
Polymer Sphere	310	0.58	10^{-1}			

Table 6.2: Table comparing the physical and hydrodynamic sizes of HyperMAG A, HyperMAG C and the polymer sphere samples.
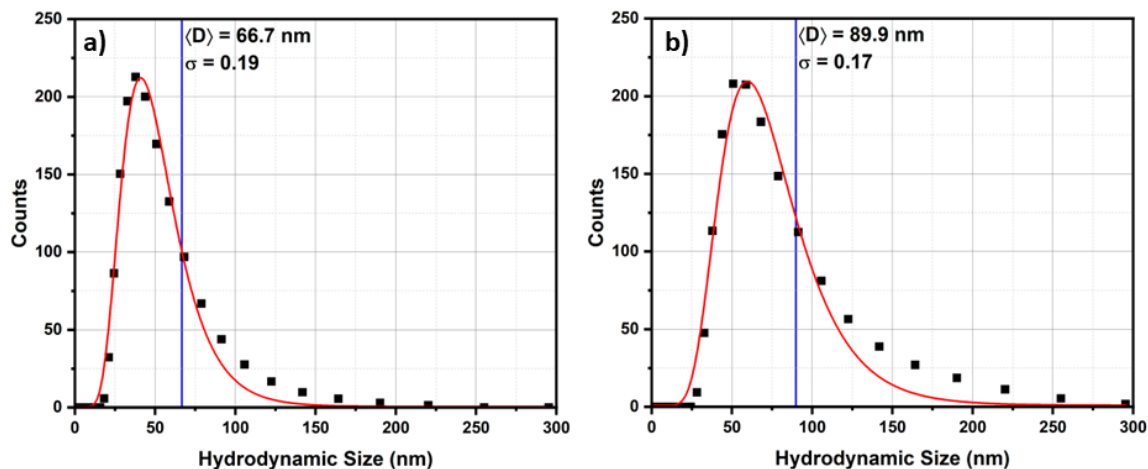
Figure 6.4: Hydrodynamic size measurements of (a) HyperMAG A and (b) Hyper-MAG C measured on a Malvern Instruments Zetasizer, with median diameter and standard deviation. Th red line is a lognormal fit.
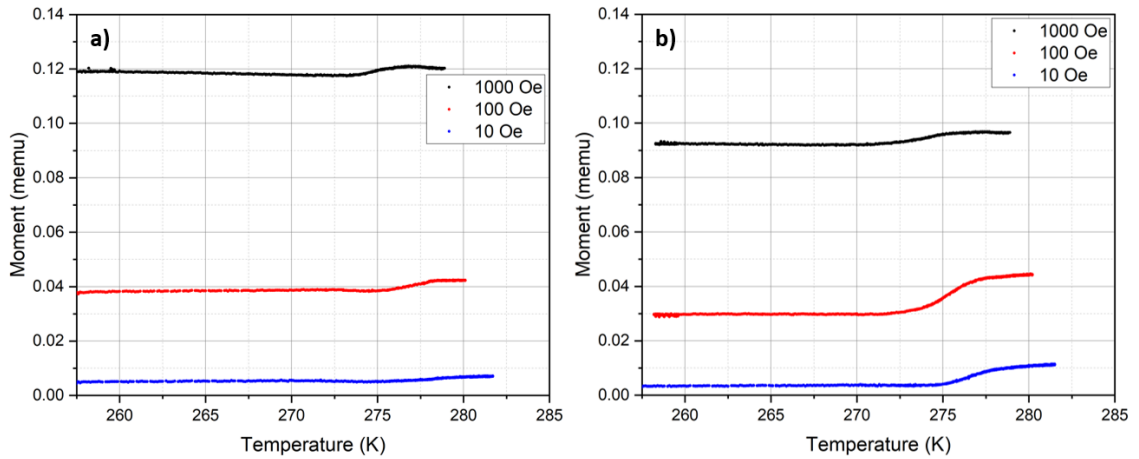
Figure 6.5: variation of moment for HyperMAG A (a) and HyperMAG C (b). In both cases the black line is a field of 1000 Oe while the sample is warming up, the red line is 100 Oe and the blue line is 10 Oe.

6.2 Mode of Magnetisation

Measurements to confirm the primary mode of magnetisation were completed in the Lakeshore 8600 VSM by freezing the samples in zero field, then applying a set field and allowing the temperature to slowly rise back above freezing[91]. As both the HyperMAG A and C samples are water based, the minimum temperature used was 230 K. The Microsense VSM described in chapter 4 was used as only a DC field was needed.

Each sample was cooled to a temperature of 230 K in zero field and left to sit at temperature for 5 minutes to ensure the carrier fluid had frozen completely. A field of 10 Oe was applied and the cooling removed, allowing the temperature to slowly rise back up above freezing. The moment and temperature were measured to define the change in magnetisation as the sample melted. This process was repeated at 100 Oe and 1000 Oe for each sample. Figure 6.5 shows the variation in magnetisation with respect to temperature for each of the samples.

For both of the samples at all measured fields, the magnetisation stays stable until the temperature reaches the melting point of the carrier fluid at 273 K. The rise following the melting of the carrier suggests that Brownian relaxation is the primary mode of magnetisation for both of the samples. Any dip following the peak is likely due to Curie-Weiss behaviour, though the temperature was not raised high enough

107
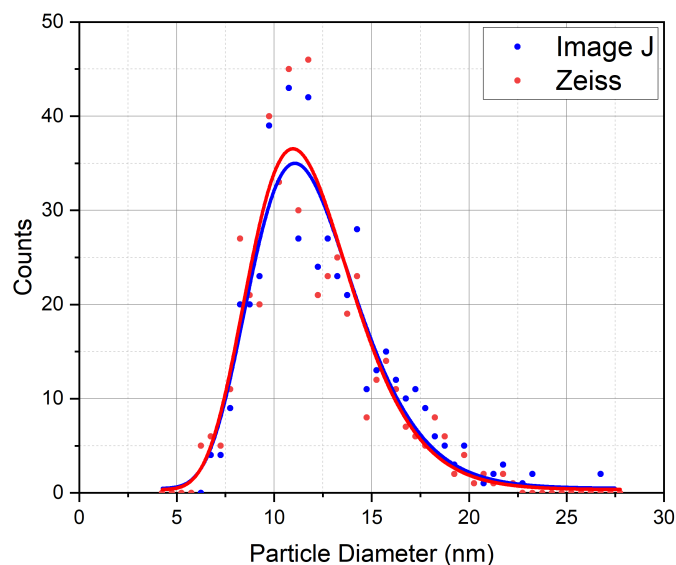
Figure 6.6: Comparison of the size distributions for HyperMAG C using the Zeiss Analyser (red) and ImageJ (blue).

to confirm.

6.3   Determination of the Anisotropy Constant

As mentioned in chapter 4, the method for determining the anisotropy distribution required both a size distribution (section 6.1) and a shape distribution. Using the image analysis software ImageJ allowed for the simultaneous measurement of a particle's size and its elongation for comparison. The two methods for particle size analysis are compared in figure 6.6, with lognormal fits applied. These are in good agreement, with the median particle diameter for the Zeiss analyser measuring at 12.3 nm and 12.1 nm for the ImageJ technique.

The particle elongation was measured in ImageJ by measuring the length of each particle in pixels along the long axis, and its width in pixels along a line approximately perpendicular to the long axis. Figure 6.7 shows this elongation as a function of particle size for HyperMAG A and C. The error bars in the figure show the standard deviation after binning the data.
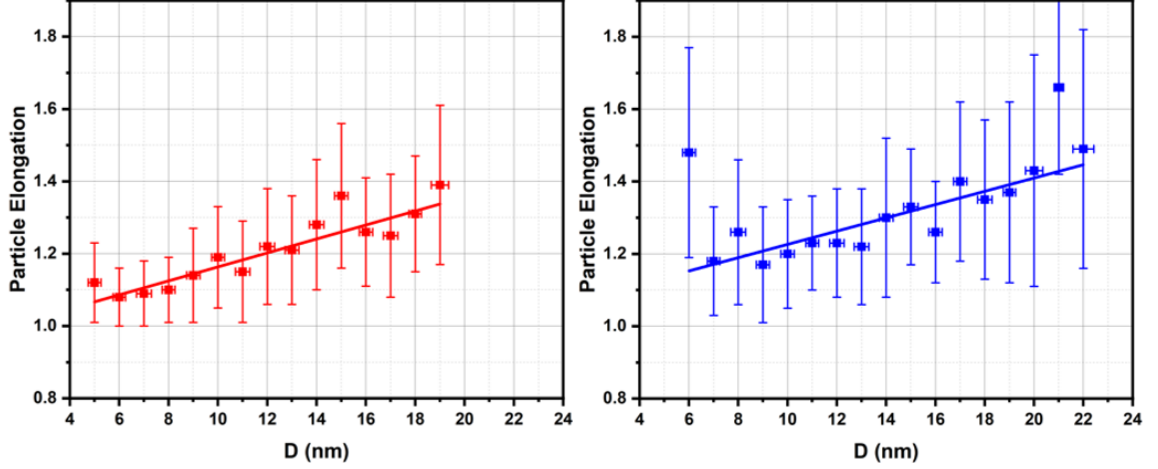
Figure 6.7: Particle elongation as a function of particle size for HyperMAG A (red) and C (blue).

There is a general increase in particle elongation as particle size increases, as does the standard deviation in particle size. However the standard deviation in particle elongation does not vary significantly with particle size. Assuming the shape anisotropy is dominant and a Gaussian distribution of anisotropy constants a value for K_m was calculated for each sample using equation 2.8, repeated below for clarity-

$$K_S = \frac{1}{2}\left(N_a - N_c\right) M_s^2 \tag{2.8}$$

with a value of 420 emu/cc used for M_s. This gave K_m values of 1.6×10^5 erg/cc for HyperMAG A and 1.3×10^5 erg/cc for HyperMAG C. The temperature decay of remanence was then measured to determine the distribution of anisotropy constants. This was completed using the process described in chapter 4, using a SQUID magnetometer at the University of Zaragoza.

HyperMAG A and C were cooled in zero field to a temperature of 1.8 K. At this point hysteresis loops including the initial magnetising curve were measured to ascertain the coercivity H_c for each sample. The measured values of H_c were 294 Oe for HyperMAG A and 298 Oe for HyperMAG C. Figure 6.8 is the measured loop for HyperMAG C. Given the sample is composed of randomly orientated uniaxial particles, the expected coercivity of the samples would be approximately $0.96 K_m/M_s$. Using the values of K_m above this gives theoretical H_c values of 320 Oe for HyperMAG A (7% difference) and 310 Oe for HyperMAG C (1%).
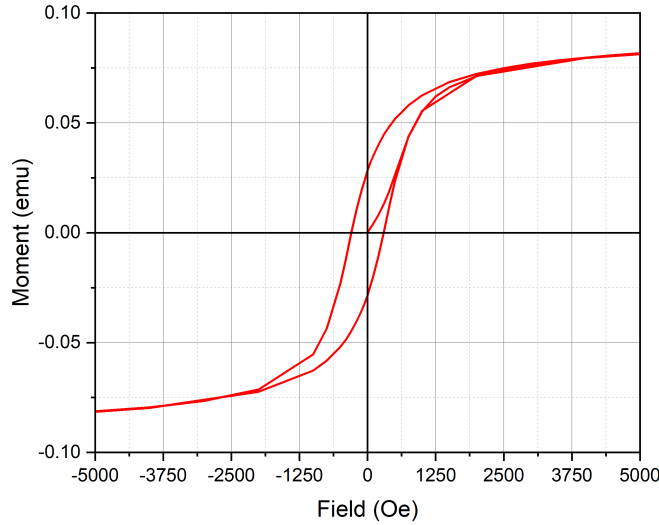
Figure 6.8: Hysteresis loop of HyperMAG C measured on a SQUID magnetometer measured at 1.8 K.

It should be noted that the loop squareness is lower than the expected $0.5M_s$ expected from the Stoner-Wohlfarth model. This is due to the bonding of the surface particles of the particle to the surfactant. This bond results in a magnetic dead layer. The surfactant bonds with the Fe^{2+} ions, forming a layer of Fe^{2+} around the magnetite core [?]. These Fe^{2+} ions are paramagnetic which increases the value of M_s.

Assuming a two atom dead layer around the surface of each nanoparticle [72], the effective median particle diameter would reduce by approximately 15 Å. This reduces the effective particle diameter to 10.0 nm and 11.4 for HyperMAG A and C respectively. This results in a median particle volume of 4500 nm^3 instead of 5,400 nm^3 for HyperMAG A, a reduction of 16%. Similarly the particle volume of HyperMAG C is reduced to 6700 nm^3 from 7800 nm^3, a reduction of 14%. The remanence would therefore also be expected to be smaller by a similar proportion. As such the expected starting values of M_r should be $0.42M_s$ for HyperMAG A and $0.43M_s$ for HyperMAG C. Low temperature hysteresis loops gave values of M_r of $0.41M_s$ for both HyperMAG A and C.

The temperature T_B at which the remanence had reduced by 50% from its value at 1.8 K was (52 ± 2) K and (62 ± 2) K for HyperMAG A and C respectively. These result in a median anisotropy value of 1.58×10^5 erg/cc and 1.29×10^5 erg/cc for HyperMAG

110
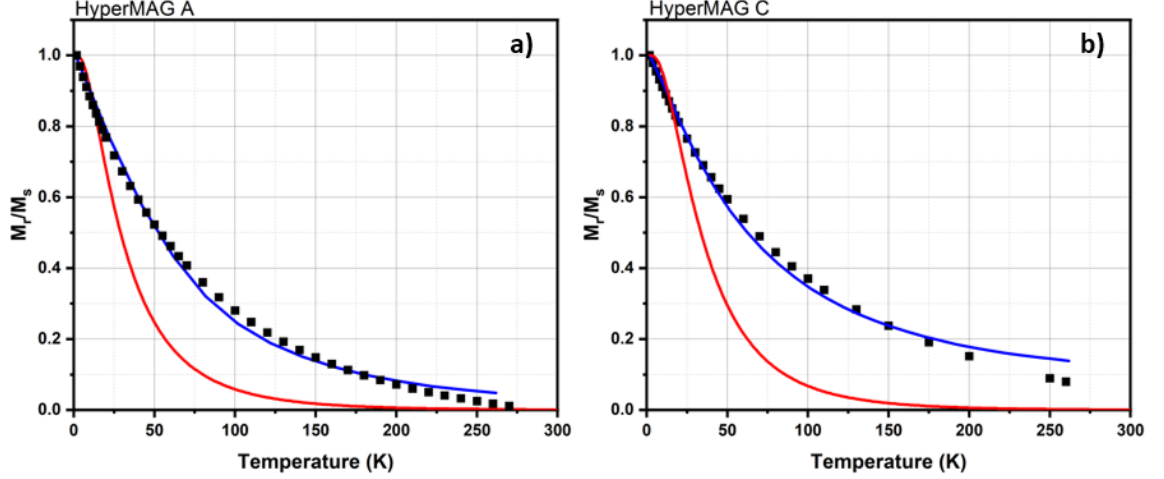
Figure 6.9: Temperature decay of remanence curves for a) HyperMAG A and b) HyperMAG C. In both cases the red fit uses only the median value for the anisotropy constant K while the blue fit uses a distribution of K values.

A and C. Figure 6.9 shows the temperature decay of remanence curves for the two samples, alongside theoretical fits assuming a single anisotropy constant (red line) and a distributed anisotropy constant (blue).

The theoretical fits were calculated using equation 2.41 for the single value of K, and equation 2.45 for the distributed value of K. These were slightly modified for a normalised value of M_r, giving equations 6.3 and 6.4 below for the uniform and distributed cases:

$$\frac{M_r}{M_{rmax}} = \left(1 - \int_0^{V_P(T)} f(V)dV\right) \qquad (6.3)$$

$$\frac{M_r}{M_{rmax}} = \left(1 - \int_0^{\infty} \int_0^{\infty} g(K)f(V)\delta(K,V)dVdK\right) \qquad (6.4)$$

In both the uniform and distributed cases C++ code was used to generate the theoretical fits in figure 6.9 based on measured parameters. This code was written by Dr Gonzalo Vallejo-Fernandez [75]. These used the measurements defined earlier in this study, D_m and K_m from this chapter with their standard distributions, magnetite's M_s of 420 emu/cc, a t_m of 100s and f_0 equalling 10^9 Hz as defined previously. For the uniform case (red line) the single value of K_m was used, resulting in the poor fit.

The distributed case (blue line) by generating variations in particle elongation (and so shape anisotropy) across the size distribution. A minimum value of K at $1.1\text{x}10^5$ erg/cc was used to represent the point at which the magnetocrystilline anisotropy of magnetite becomes the primary contributor. Given the difference in the quality of the fits it is clear that the distribution of anisotropy has a significant impact on the HyperMAG samples.

This chapter has been the inital results chapter, focusing on the physical and low frequency magnetic characterisations of the nanoparticle samples. The physical and hydrodynamic sizes of HyperMAG A and C have been presented through the use of a Transmission Electron Microscope and Photon Correlation Spectroscopy. The size of the polymer spheres have also been measured through the use of a Scanning Electron Microscope. The majority of the chapter has been focussed on determining the anisotropy (both constant and distributed) for the HyperMAG samples. This required two major measurements. The first was a particle shape analysis in which the elongation of particles was measured as a function of their size. This provided median values of the anisotropy constant K_m, 1.6×10^5 erg/cc for HyperMAG A and 1.3×10^5 for HyperMAG C. This was followed by measuring the temperature decay of remanence with the use of the SQUID magnetometer at the University of Zaragoza. Using the value at which the remanence had reduced by half gave values of K_m of 1.58×10^5 for HyperMAG A, and 1.29×10^5 for HyperMAG C. Modelled data using this uniform K was then compared with a distributed K and the measured remanence, with the latter giving a much closer fit. Chapter 7 will be primarily about the high frequency measurements of specific absorption rate.

Chapter 7

High Frequency Characterisation of Magnetic Nanoparticles

As discussed in chapter 3, accurately calculating the heating output of the magnetic particles in an applied field requires two factors. The first is the removal of viscous or rotational heating, the second is the confirmation that hysteresis heating can be accurately calculated and is the primary contribution if the particles are immobilised. With this in mind the heating measurements were completed in two stages; measurement of the SAR using the Magnetherm system described in chapter 4, and calculation of the expected SAR from hysteresis heating using the B-H looper in chapter 5.

7.1 Magnetherm Measurements

Each sample was measured three times at the maximum field of 180 Oe. This was to ensure repeatability in the heat rates, the averages for which can be seen in figure 7.1. The heating rates are non-linear - this is expected as it is shown by Drayton *et al.* [80] who completed the modifications to the system. This non-linearity arises due to the wall thickness of the measurement cell. As the fluid heats a temperature gradient will rise between it and the cell wall. As this gradient increases the losses to the cell wall increases alongside. At lower values of ΔT the temperature differential will be

minimal provided the fluid and cell are at thermal equilibrium prior to beginning the experiment. These lower values of ΔT provide the most linear responses.
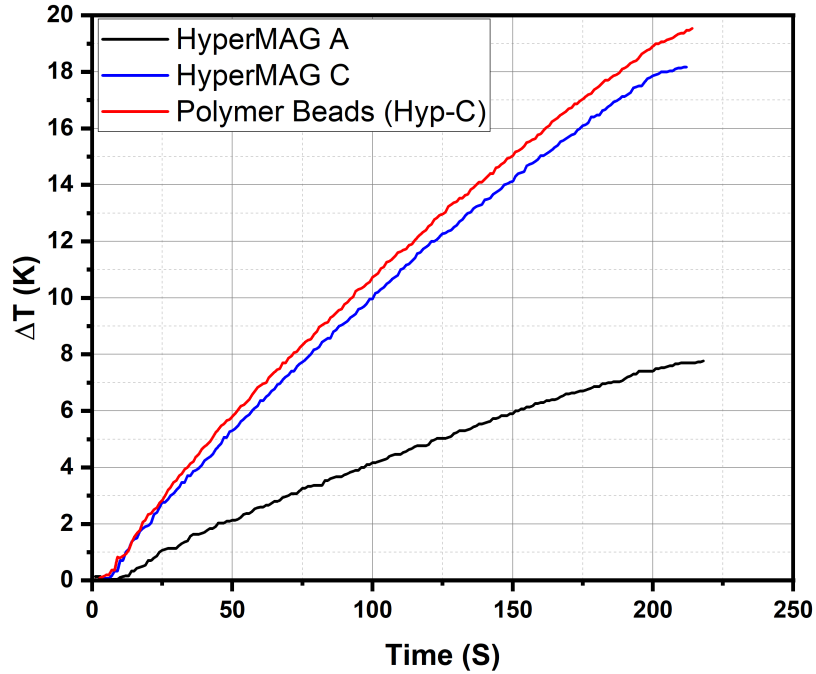
Figure 7.1: Heating rate of HyperMAG A, C and the polymer sphere samples in a 180 Oe, 111kHz field.

Using the initial 50 seconds [67] of the change in temperature and equation 3.11 (repeated below), values for the SAR were calculated for comparison with the hysteresis heating in the next section.

$$SAR = \frac{c\rho_c}{\phi_{Fe}} \frac{\Delta T}{\Delta t} \tag{3.11}$$

For HyperMAG A and C the colloid is just deionised water, and as such the specific heat capacity is 4.184 J/gK and the density of the colloid is 1 g cm^{-3}. The concentration of iron oxide particles that was supplied with the samples was 10 mg cm^{-3} for HyperMAG A and 5 mg/cm^3 for HyperMAG C. This gives SAR values of 30.7±042 Watts/gram for HyperMAG A and 41.4±0.4 Watts/gram for HyperMAG C. The errors on these values were calculated through the combination of the minimum read values on the data-reader (0.01 s and 0.1 ^{o}K), giving an error of ±0.1.

Sample	$<D>$ nm	Surfactant	Field Oe	Frequency kHz	ϕ_{Fe} mg ml^{-1}	SAR W g^{-1}
VF-A	10.3	Isopar M	180	111.5	20	20±1
D-A	10.3	Water	180	111.5	5	21.8±0.4
H-A	10.9	Water	180	111.5	10	30.7±0.4
VF-C	15.2	Isopar M	180	111.5	20	16±1
D-C	15.2	Water	180	111.5	5	44.5±0.7
H-C	12.3	Water	180	111.5	5	41.4±0.4

Table 7.1: Comparison of Magnetherm SAR results to those in literature. Samples VF-A and VF-C are from Vallejo-Fernandez *et al.* [14], samples D-A and D-C are from Drayton *et al.* [80], and samples H-A and H-C are HyperMAGs A and C respectively.

This was compared with the standard deviation of the three measured results for each sample which gave an error of ±0.4. The higher value of error was used.

For the reasons described in the section on hyperthermia in chapter 3, a comparison of these SAR values to the wider literature is unlikely to provide further insight. Differing measurement systems and protocols have been shown to provide different SAR values for the same samples in similar conditions [71]. Vallejo-Fernandez *et al.* [14] and Drayton *et al.* [80] use the same SAR calculation as in this work focussing on the density of iron over weight of magnetic nanoparticles. Additionally they use the same Magnetherm system for their measurements, though Vallejo-Fernandez uses an unmodified system. A comparison between the SAR presented in their papers and this work's results can be seen in table 7.1.

Vallejo-Fernandez *et al.* use an unmodified Magnetherm system to measure oil and wax based nanoparticles. Although this is not stated specifically in the text, the values of median diameter given are that of the HyperMAG range. As such samples A and C (noted on table 7.1 as VF-A and VF-C) are used for comparison with HyperMAG A and C (H-A and H-C). The specific heat capacities of the Isopar M oil are given as 2206 Jkg^{-1}K^{-1}, approximately half that of water, and the density is 0.78 g cm^{-1} instead of 1 g cm^{-1}. however the concentration is 20 mg/cm^3, which is double that of the HyperMAG A used in this work.

The stated SAR values used a field of 250 Oe, 30% larger than the field used in this work. An approximate vale of SAR at 180 Oe was gathered from the fit of figure 4,

Vallejo-Fernandez *et al.* [14]. These values are 20 Wg^{-1} for VF-A and 16 Wg^{-1} for VF-C, though the error is considerable given how they have been acquired. The SAR values are significantly smaller than the values measured in this work, VF-A 35% smaller and VF-C 60% smaller. This is likely due to the issues with the unmodified Magnetherm system, identified in chapter 4. The fluid not uniformly sitting inside the field would result in a much reduced dT/dt as well as increased heat losses to the surroundings.

Drayton *et al.* is a much closer comparison as the same modified Magnetherm was used as in this work. The HyperMAG particles for their measurements were also water based. As such samples A and C (listed on table 7.1 as D-A and D-C respectively) are used for comparison. The only major differences between the measurements in Drayton *et al.* and this work are the notable difference in the median size of Hyper-MAG C and the use of a 10 mg ml^{-1} concentration for HyperMAG A in this work. The particle sizes stated in Drayton's paper are the official particle sizes given by Liquids Research, and so are likely quoted rather than measured.

The SAR values measured by Drayton *et al.* are 21.8±0.4 Wg^{-1} for D-A and 44.5±0.7 Wg^{-1} for D-C. The HyperMAG C samples show good agreement, with a difference of less than 10%. The much more considerable difference between D-A and H-A (29%). Given the difference in ϕ_{Fe} a difference was to be expected, though some of this should be accounted for by reducing the value by the density of iron in the sample.

The SAR equation used in this work needs the density of iron per millilitre ϕ_{Fe}. This was not known for the polymer sphere sample. This was calculated from the M_s of the fluid and its density. The specific heat can be assumed to be similar to that of the regular samples as the polymer has a lower value of c than the deionised water and as such heating the water should be the rate determining step.

The M_s was provided at 1.58 emu g^{-1}, as well as the density at 1.02 g cm^{-3}. The expected M_s for 3 ml of fluid should be 4.83 emu. The polymer sphere samples provided by Liquids Research used HyperMAG C particles in the polymerisation process, so the M_s can be used to estimate the volume of magnetite in the 3 ml of fluid. From there, the concentration of iron can be calculated using equation 7.1 below

$$\phi_{Fe} = V_{Fe_3O_4}\phi_{Fe_3O_4}\frac{m_{Fe}}{m_{Fe_3O_4}} \tag{7.1}$$

where $V_{Fe_3O_4}$ is the volume of magnetite in the fluid, $\phi_{Fe_3O_4}$ is the density of magnetite, m_{Fe} is the atomic mass of iron per molecule of magnetite (167.5 g) and $m_{Fe_3O_4}$ is the atomic mass of magnetite (231.5 g). From equation 7.1 the expected concentration of iron in the polymer sphere sample solution is 3.76 $\text{mg}_{fe}/\text{ml}_{solution}$, and an SAR of 29.0±0.5 Watts/gram.

7.2 Hysteresis Heating

7.2.1 Moment Calibration

To measure the SAR output of the hysteresis heating, the moment in A.U. needed to be calibrated into a moment in emu. For a direct comparison, the loops needed to be measured in the same conditions as those used by the Magnetherm system (111 kHz 180 Oe) which would not fully saturate the sample. As the expected M_s of the samples was known this would have been the simpler method of defining the calibration standard. A sigmoidal function provides a suitable fit for the shape of a hysteresis loop, and so was used to calibrate the output of the B-H looper from AU to emu. This was completed by applying a sigmoidal fit to the positive and negative sweeps of a hysteresis loop at high field, as shown in figure 7.2.

The equation generated by the fitting software was then extrapolated to the point at which it saturates. This maximum value of the moment in AU is equal to the expected M_s for its volume. In the case of the HyperMAG samples M_s is 1.07 emu/cc, so for 7 μl of fluid the saturation point is 0.075 emu. For the polymer bead samples the M_s is stated to be 1.61 emu/cc, so 7 μl of fluid gives a saturation point of 0.011 emu. An example hysteresis loop for HyperMAG C with the updated moment in emu is shown in figure 7.3. Figure 7.4 shows a loop for the polymer sphere sample in the same conditions.
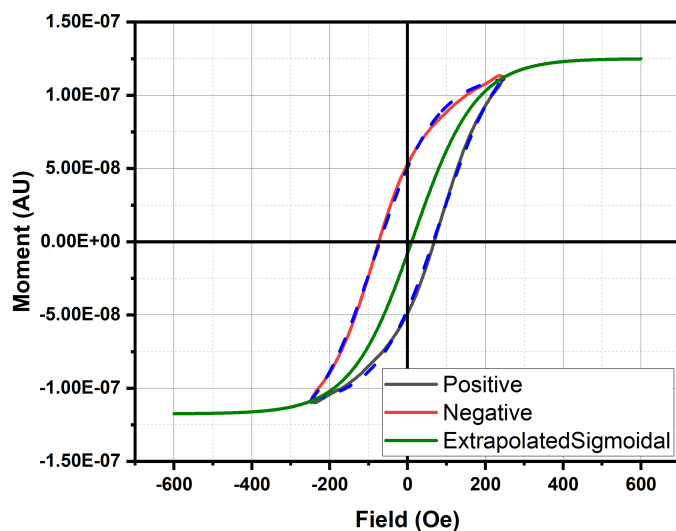
Figure 7.2: Hysteresis loop for HyperMAG C measured at 62 kHz, with an extrapolated sigmoidal fit (green) used to show the approximate saturation point.
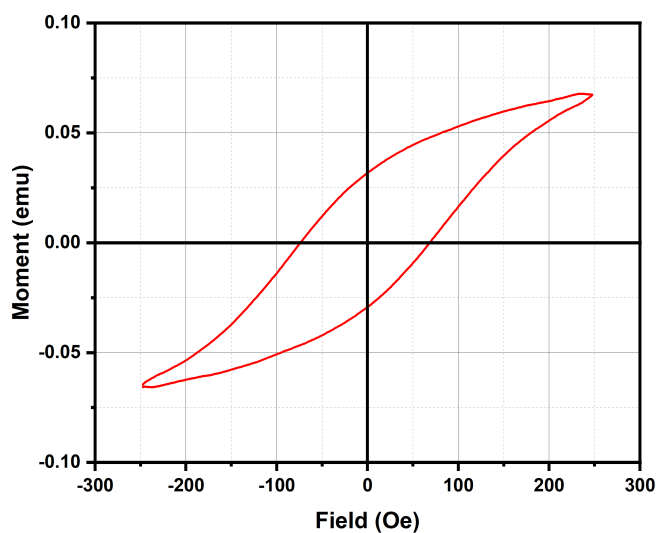
Figure 7.3: Moment calibrated hysteresis loop for HyperMAG C measured at 62 kHz.
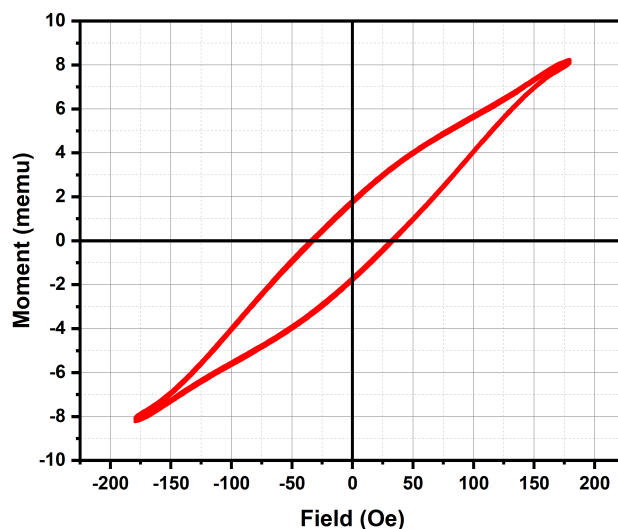
Figure 7.4: Moment calibrated hysteresis loop for the polymer sphere sample measured at 62 kHz.

7.2.2 Hysteretic SAR

With the moment calibration completed the next stage was the direct calculation of the SAR. The area inside the hysteresis loops was measured for each of the samples at varying fields and frequencies. This was completed by separating the upper (positive to negative) and lower (negative to positive) sweeps of a loop and removing all of the values with a moment of zero or lower. An example of this can be seen in figure 7.5.

The upper and lower sweeps were integrated over all values of H to give the area enclosed, also shown by figure 7.5. The area of the lower sweep was subtracted from the upper sweep to give the enclosed area giving half the hysteretic energy in erg. The product of these values with the frequency of measurement and the conversion factor to Joules gave the energy in Watts. For hyperthermia purposes the SAR is a measure of the power per unit mass of magnetic material, the Fe^{2+} and Fe^{3+} ions as in the general case.

From this, the measured SAR purely from hysteresis heating from the samples in the same conditions as the Magnetherm system are (17.1±0.3) Wg^{-1} for HyperMAG A, (22.8±0.3) Wg^{-1} for HyperMAG C and (28.5±0.3) Wg^{-1} for the polymer sphere

119
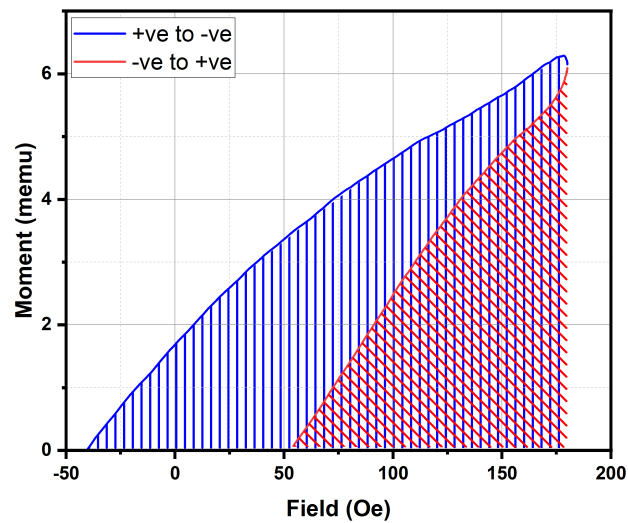
Figure 7.5: Example of the process for measuring the area inside a hysteresis loop. The area of the red shaded section is removed from that of the blue shaded to give the area within the loop.
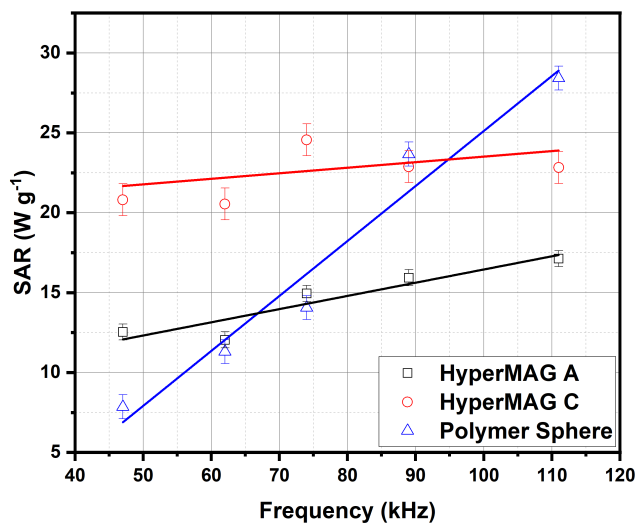
Figure 7.6: Variation in SAR for HyperMAG A, HyperMAG C and the polymer sphere samples as a function of frequency in a 180 Oe field.

samples.

A direct comparison with the Magnetherm system is shown in table 7.2. The error values shown are a result of the standard deviation in the results in combination with the error in the values frequency and field.

Sample	Magnetherm SAR (M-SAR) W g^{-1}	Error W g^{-1}	Hysteretic SAR (H-SAR) W g^{-1}	Error W g^{-1}	Percentage of H-SAR/M-SAR %
HyperMAG A	30.7	0.4	17.1	0.3	55.8
HyperMAG C	41.4	0.4	23	0.7	55.2
Polymer Spheres	29.0	0.5	28.4	0.5	98.1

Table 7.2: Comparison of total SAR (from Magnetherm system, M-SAR), hysteretic SAR (from B-H looper, H-SAR) and percentage of SAR given by hysteretic heating.

For both of the HyperMAG samples the measured SAR specifically through hysteresis heating accounts for just over 50% of the total heating - 56% for HyperMAG A and 55% for HyperMAG C. This is in good agreement of the wax immobilization study completed by Vallejo-Fernandez *et al.* [14] with the addition of confirming approximately half of the heating produced is hysteretic in origin at this field and frequency.

The polymer sphere sample with the immobilised particles shows a very small drop in the SAR between total heating power and hysteresis heating. This follows the expectations in section 3.2.4 - the polymer spheres cannot begin to rotate at the frequency required. There are several possibilities for how the additional 1.9% SAR arises. Polymer spheres on the extreme end of the distribution could be partially rotating in the field. These would have to be in the 50 nm or lower range for the Brownian relaxation time to be low enough to rotate. Polymer spheres of this size were not seen in the particle size distribution. A second option is the creation of a similar form of heating to susceptibility loss. The particles immobilised in the polymer spheres will be randomly aligned. This will lead to particles whose easy axis is not aligned with the field, causing a separation between their moment and the applied field. As with susceptibility loss the resulting magnetostatic energy would be released as heat.

In addition to the measurements made for comparison to the Magnetherm system,

additional SAR measurements for the samples were made for each of the frequencies available to the B-H looper. The SAR values can be seen in figure 7.6. These were also completed at 180 Oe, with the 111 kHz values being those quoted in table 7.2. Both HyperMAG A and C show a relatively gradual linear increase of SAR with frequency. As frequency is used as a multiplier in the hysteretic SAR calculation the linear response is expected.

HyperMAG A has an SAR response starting at 12.5 ± 0.3 Wg^{-1} and increasing to 17.3 ± 0.3 Wg^{-1} over the 64 kHz range. HyperMAG C had a lower SAR increase with frequency, starting at 21 ± 1 Wg^{-1} and ending at 23 ± 1 Wg^{-1}. The approximate increase of SAR as a function of frequency for HyperMAG A and C are approximately 7.5×10^{-5} Wg^{-1}Hz^{-1} and 1.6×10^{-5} Wg^{-1}Hz^{-1} respectively. The polymer sphere samples have a much more dramatic SAR increase, starting at 8.0 ± 0.5 Wg^{-1} and reaching 28.5 ± 5 Wg^{-1}. This increase is 3.2×10^{-4} Wg^{-1}Hz^{-1}, an order of magnitude larger than the regular samples.

Conclusion of results chapters description of both techniques for SAR measurement. Magnetherm system and results described first, with comparison to literature following as close to the same technique. Hysteretic heating second, with process for measuring the H-SAR at field. Two sets of results compared, showing hysteresis heating accounting for 55% of total heating. polymer spheres show almost no difference between hysteretic sar and total sar. polymer spheres additionally show significantly higher SAR variation with frequency. Proceeding to conclusions and future work.

This concludes the second results chapter. This chapter has been primarily about the heating outputs of the three nanoparticle samples, measured through both total SAR using the Magnetherm system and the hysteretic SAR using the B-H looper. The process through which the total SAR is described first, followed by the results for the samples and comparison with the two works whose technique is closest to this work. This is followed by the process for the calculation of the hysteretic SAR by the B-H looper system. Comparing the two shows that the hysteretic hating accounts for just over 50% of the total SAR for the regular particles. The hysteresis heating accounts for 98% of the total SAR for the polymer sphere samples, confirming immobilizing the particles in this fashion prevents heating through the stirring mechanism. In the next chapter the conclusions of the thesis will be presented.

Chapter 8

Conclusions and Future Work

In this work the conclusions and future work will be subdivided into three main areas. These are the determination of the anisotropy distribution for the HyperMAG samples, the construction of a high frequency B-H looper, and the comparison of the total specific absorption rate and that specifically from hysteresis heating for regular magnetic nanoparticles and those immobilised in polymer spheres.

Firstly, the distribution of anisotropy constants was measured for both the Hyper-MAG A and HyperMAG C samples. This was completed through the careful measurement of both the size and shape distributions for the samples to confirm the median value of the anisotropy distribution. This was combined with the temperature decay of remanence measurements completed by Professor Clara Marquina at the University of Zaragoza to give the width of the distribution. The remanence measurements were compared with two fitting programs written by Dr Vallejo-Fernandez at the University of York. The first of these used a uniform value of the anisotropy constant, the second used the anisotropy distribution calculated in this work.

The result of this is confirmation that the distribution of anisotropy constants must be taken into account when discussing systems where shape anisotropy is a dominant factor. This is important in the context of magnetic hyperthermia as the hysteretic losses control the amount of heat being generated. Previously in such cases the energy barrier to reversal in such systems has been assumed to be controlled primarily by the volume distribution. Should the anisotropy distribution not be taken into account

the hysteresis losses and therefore the heat generated at given parameters would be difficult to meaningfully predict.

Suggestions for future work in the area of the anisotropy distribution follow on directly from that last point. This work did not attempt to predict the hysteresis heating P_{hys} using the uniform or distributed case. Using the calculated distribution of anisotropy to predict the hysteresis heating would allow for a defined sample would allow for much greater precision in future magnetic hyperthermia trials.

The second advancement presented in this work is the construction of a high frequency B-H looper. It is the first system of this class to use soft ferrite cores, MnZn rods in this case, to amplify the field produced by the primary coil. This presents several advantages over other systems. Due to the field amplification the current requirements are significantly smaller than other systems, with a maximum field of 450 Oe at 2.5 A of applied current. Other systems are generally in the order of 10s of amps [16] to reach these fields, with some systems reaching the hundreds [86]. The low current also results in lesser cooling requirements. The B-H looper currently has an available range of five frequencies between 47 kHz and 111 kHz, though this could be expanded with minimal effort. A signal-to-noise ratio of 8 (9 dB) was achieved using 7 μL of a 13.4 G solution.

The final aim of the project was the comparison of the heating provided by different mechanisms of magnetic hyperthermia. The B-H looper was used in conjunction with a modified Nanotherics Magnetherm to measure and compare the specific absorption rates of a singular mechanism for heating, hysteretic heating, and the total heating output. The samples used were HyperMAG, A HyperMAG C and a sample of HyperMAG C in which the nanoparticles had been immobilised in 310 nm diameter polymer spheres. This immobilisation was to prevent the larger nanoparticles from physically rotating to follow the field, resulting in viscous or rotational heating.

The Magnetherm system was used to measure the total specific absorption rate through the heating of the sample in response to a direct high frequency field. These provided SAR values consistent with previous published works using the same samples and setup. These were 30.7±0.4 Wg^{-1} for HyperMAG A, 41.4±0.4 Wg^{-1} for HyperMAG C and 29.0±0.5 Wg^{-1} for the polymer sphere sample.

The B-H looper was used to measure the hysteretic SAR through the measurement of hysteresis loops at high frequency. These were measured using the same field and frequency as the Magnetherm system. The area encapsulated by the hysteresis loops multiplied by the frequency of operation gave the hysteretic SAR. For HyperMAG A the hysteretic SAR was measured at 17.1 ± 0.3 Wg^{-1}, 55.6% that of the total SAR. 23.0 ± 0.7 Wg^{-1} for HyperMAG C, 55.2% of the total. The polymer sphere samples provided a hysteretic SAR of 28.4 ± 0.5 Wg^{-1}, almost within error of the total specific absorption rate with a difference of only 1.9%.

The results of the HyperMAG A and C comparisons are in good agreement with previous works [36]. The polymer sphere sample presents a novel option for reducing the difficulty in predicting the heating output of hyperthermia therapies. Particles immobilised this way are unlikely to be biocompatible and are not currently approved for human use, but work as a proof of concept. If the hysteresis of a known particle can be accurately predicted as mentioned in the distribution of anisotropy this helps remove a significant barrier to the further usage of magnetic hyperthermia as a cancer therapy.

Options for further work on this front are split between the B-H looper and further measurements. The looper itself could be made significantly easier to use, either by simplifying the process in which the system parameters are changed or by automating the aspects that currently require human input. While the number of possible frequencies could be easily expanded the process by which one switches from one to the other currently requires taking much of the circuit apart to replace the capacitor banks. This could be replaced with a switch or dial to choose which bank to use. The data analysis could also be automated through the use of LabVIEW or Python.

It was hoped that the data provided by this work would be able to provide the groundwork for hyperthermia dosages. This now seems unlikely, but more measurements can be made using the high frequency B-H looper. Measuring the variation of SAR with field, and more measurements with the variation of frequency would allow for further advancement in the field. Further insight as to the proportions of hysteretic heating to viscous heating may negate the need for immobilisation at all.

Glossary

A_{VW} Hamaker constant. 48

A_c cross sectional area of secondary coil. 88

B magnetic flux density. 17, 18

C capacitance. 85

D particle diameter. 104

$D_P(0)$ critical diameter for superparamagnetsim. 54

$D_P(H)$ critical diameter for for swicthing in applied field H. 54, 55, 59

D_c critical diameter for transition from multi- to single-domain particle. 22

D_m median particle diameter. 104, 111

E_C critical energy barrier. 45

E_D dipole energy. 49

E_K anisotropy energy. 20, 21, 24, 28

E_P potential energy. 28, 29

E_{VW} van der Walls energy of attraction. 48

E_{ex} exchange energy. 21, 38

E_{ms} magnetostatic energy. 21

H applied magnetic field. 6, 17, 18, 33, 35–37, 54, 55, 67, 119

Bibliography

[1] R E Rosensweig. Heating magnetic fluid with alternating magnetic field. *Journal of Magnetism and Magnetic Materials*, 252:370–374, 11 2002.

[2] Y-X J Wang. Superparamagnetic iron oxide based mri contrast agents: Current status of clinical application. *Quantitative Imaging in Medicine and Surgery*, 1:35–40, 2011.

[3] Q A Pankhurst, J Connolly, S K Jones, and J Dobson. Applications of magnetic nanoparticles in biomedicine. *Journal of Physics D: Applied Physics*, 36:167–181, 2003.

[4] K Mahmoudi, A Bouras, D Bozec, R Ivkov, and C Hadjipanayis. Magnetic hyperthermia therapy for the treatment of glioblastoma: a review of the therapy's history, efficacy and application in humans. *International Journal of Hyperthermia*, 34:1316–1328, 2018.

[5] M Johannsen, U Gneveckow, L Eckelt, A Feussner, N. Waldöfner, R Scholz, S Deger, P Wust, S A Loening, and A. Jordan. Clinical hyperthermia of prostate cancer using magnetic nanoparticles: Presentation of a new interstitial technique. *International Journal of Hyperthermia*, 21:637–647, 2005.

[6] S Y Lee, G Fiorentini, A M Szasz, G Szigeti, A Szasz, and C A Minnaar. Quo vadis oncological hyperthermia (2020)? *Frontiers in Oncology*, 10, 9 2020.

[7] S V Spirou, M Basini, A Lascialfari, C Sangregorio, and C Innocenti. Magnetic hyperthermia and radiation therapy: Radiobiological principles and current practice, 6 2018.

[8] S Müller. Magnetic fluid hyperthermia therapy for malignant brain tumors-an ethical discussion. *Nanomedicine: Nanotechnology, Biology, and Medicine*, 5:387–393, 12 2009.

[9] J K Patra, G Das, L F Fraceto, E V R Campos, M D P Rodriguez-Torres, LS Acosta-Torres, LA Diaz-Torres, R Grillo, M K Swamy, S Sharma, S Habtemariam, and H S Shin. Nano based drug delivery systems: Recent developments and future prospects. *Journal of Nanobiotechnology*, 16, 9 2018.

[10] I Rubia-Rodríguez, A Santana-Otero, S Spassov, E Tombácz, C Johansson, P De La Presa, F J Teran, M D P Morales, S Veintemillas-Verdaguer, N T K Thanh, M O Besenhard, C Wilhelm, F Gazeau, Q Harmer, E Mayes, B B Manshian, S J Soenen, Y Gu, Á Millán, E K Efthimiadou, J Gaudet, P Goodwill, J Mansfield, U Steinhoff, J Wells, F Wiekhorst, and D Ortega. Whither magnetic hyperthermia? a tentative roadmap. *Materials*, 14:1–37, 2021.

[11] A S Thakor, J V Jokerst, P Ghanouni, J L Campbell, E Mittra, and S S Gambhir. Clinically approved nanoparticle imaging agents. *Journal of Nuclear Medicine*, 57, 2016.

[12] L Wu, W Wen, X Wang, D Huang, J Cao, X Qi, and S Shen. Ultrasmall iron oxide nanoparticles cause significant toxicity by specifically inducing acute oxidative stress to multiple organs. *Particle and Fibre Toxicology*, 19, 12 2022.

[13] S I Park, J H Lim, J H Kim, H I Yun, and C O Kim. Toxicity estimation of magnetic fluids in a biological test. *Journal of Magnetism and Magnetic Materials*, 304:406–408, 2006.

[14] G Vallejo-Fernandez, O Whear, A G Roca, S Hussain, J Timmis, V Patel, and K O'Grady. Mechanisms of hyperthermia in magnetic nanoparticles. *Journal of Physics D: Applied Physics*, 46, 2013.

[15] W J Atkinson, I A Brezovich, and D P Chakraborty. Usable frequencies in hyperthermia with thermal seeds. *IEEE Transactions on Biomedical Engineering*, BME-31:70–75, 1 1984.

[16] V Connord, B Mehdaoui, R P Tan, J Carrey, and M Respaud. An air-cooled litz wire coil for measuring the high frequency hysteresis loops of magnetic samples - a useful setup for magnetic hyperthermia applications. *Review of Scientific Instruments*, 85, 2014.

[17] P Lenox, L. K. Plummer, P Paul, J. E. Hutchison, A Jander, and P Dhagat. High-frequency and high-field hysteresis loop tracer for magnetic nanoparticle characterization. *IEEE Magnetics Letters*, 9:1–5, 2017.

[18] Liquids Research Ltd. https://www.liquidsresearch.com/.

[19] S E Khalafalla and G W Reimers. Preparation of dilution-stable aqueous magnetic fluids. *IEEE Transactions on Magnetics*, 16:178–183, 1980.

[20] B D Cullity and C D Graham. *Introduction to Magnetism and Magnetic Materials, Second Edition*. 1998.

[21] P Weiss. The variation of ferromagnetism with temperature. *Comptes Rendus Hebdomadaires Des Seances De L Academie Des Sciences*, 143:116, 1906.

[22] J Frenkel and J Dorfman. Spontaneous and induced magnetisation in ferromagnetic bodies. *Nature*, 126:274–275, 1930.

[23] C Kittel. Theory of the structure of ferromagnetic domains in films and small particles. *Physical Review*, 70:965–971, 12 1946.

[24] C Kittel and J K Galt. Ferromagnetic domain theory. *Solid State Physics - Advances in Research and Applications*, 3:437–564, 1956.

[25] L Néel. Propriétés d'un ferromagnétique cubique en grains fins. *Comptes Rendus Hebdomadaires Des Seances De L Academie Des Sciences*, 224:1488–1490, 1947.

[26] A. H. Morrish and S. P. Yu. Magnetic measurements on individual microscopic ferrite particles near the singl-domain size. *Physical Review*, 102:670–673, 1956.

[27] E C Stoner and E P Wohlfarth. A mechanism of magnetic hysteresis in heterogeneous alloys. *Mathematical and Physical Sciences*, 240:599–642, 1948.

[28] N Akulov. Zur quantentheorie der temperaturabhängigkeit der magnetisierungskurve. *Zeitschrift für Physik*, 100:197–202, 1936.

[29] L R Bickford. Ferromagnetic resonance absorption in magnetite single crystals. *Physical Review*, 78:449–457, 1950.

[30] C Zener. Classical theory of the temperature dependence of magnetic anisotropy energy. *Physical Review*, 96:1335–1337, 1954.

[31] J H Van Vleck. On the anisotropy of cubic ferromagnetic crystals. *Physical Review*, 52:1178–1198, 1937.

[32] S Mørup, H Topsøe, and J Lipka. Modified theory for mössbauer spectra of superparamagnetic particles : application to Fe$_3$O$_4$. *Le Journal de Physique Colloques*, 37:C6–287–C6–290, 1976.

[33] F. Söffge and E. Schmidbauer. Ac susceptability and static magnetic properties of an Fe$_3$O$_4$ ferrofluid. *Journal of Magnetism and Magnetic Materials*, 24:54–66, 1981.

[34] S R Hoon, B K Tanner, and M Kilner. Torque magnetometry of magnetic fluids. *Journal of Magnetism and Magnetic Materials*, 39:30–34, 1983.

[35] D B Lambrick, S R Hoon, N Mason, and M Kilner. Measurements of the anisotropy constant in Ni−Fe and Fe$_3$O$_4$ magnetic fluids. *IEEE Transactions on Magnetics*, 24:1647–1649, 1988.

[36] G Vallejo-Fernandez and K. O'Grady. Effect of the distribution of anisotropy constants on hysteresis losses for magnetic hyperthermia applications. *Applied Physics Letters*, 103:142417, 2013.

[37] I Joffe and R Heubregbr. Hysteresis properties of distributions of cubic single-domain ferromagnetic particles. *Philisophical Magazine*, 29:1051–1059, 1974.

[38] L Néel. Théorie du traînage magnétique des substances massives dans le domaine de rayleigh. *Journal de Physique et le Radium*, 11:49–61, 1950.

[39] C P Bean and J D Livingston. Superparamagnetism. *Journal of Applied Physics*, 30:S120–S129, 1959.

[40] A Tari, R W Chantrell, S W Charles, and J Popplewell. The magnetic properties and stability of a ferrofluid containing Fe$_3$O$_4$ particles. *Physica B+C*, 97:57–64, 1979.

[41] W J Schuele, S Shtrikman, and D Treves. Observation of superparamagnetism by the mössbauer effect. *Journal of Applied Physics*, 36:1010–1011, 1965.

[42] E Kneller. *Proceedings of the International Conference on Magnetism*. Institute of Physics, ninth edition, 1964.

[43] H D Williams, K O'Grady, S W Charles, and K J Davies. Curie-weiss behaviour in ferrofluids: the effects of particle size and distribution. *Journal of Magnetism and Magnetic Materials*, 122:134–138, 1993.

[44] C G Granqvist and R A Buhrman. Ultrafine metal particles. *Journal of Applied Physics*, 47:2200–2219, 1976.

[45] N Ashcroft and N D Mermin. *Solid State Physics*. Saunders Collage Publishing, 1974.

[46] C Kittel. *Introduction to Solid State Physics*. John Wiley and Sons, sixth edition, 1986.

[47] J. I. Gittleman and S. Bozowski B. Abeles. Superparamagnetism and relaxation effects in granular ni-sio2 and ni-al2o3. *Physical Review B*, 9, 1974.

[48] E P Wohlfarth. Spin glasses exhibit rock magnetism. *Physica B+C*, 86-88:852–853, 1977.

[49] S Shtrikman and E P Wohlfarth. The theory of the vogel-fulcher law of spin glasses. *Physics Letters*, 85:468–470, 1981.

[50] L E Wenger and J A Mydosh. Nonuniqueness of $H^{2/3}$ and H^2 field-temperature transition lines in spin-glasses. *Physical Review B*, 29:4156–4158, 1984.

[51] J L Dormann, L Bessaist, and D Fioranij. A dynamic study of small interacting particles: Superparamagnetic model and spin-glass laws. *Journal of Physics C*, 21:2015–2034, 1988.

[52] R Street and J C Woolley. A study of magnetic viscosity. *Proceedings of the Physical Society. Section A*, 62:562–572, 1949.

[53] K O'Grady, J Popplewell, and S W Charles. Time dependent magnetization of a system of fine cobalt particles. *IEEE Transactions on Magnetics*, 17:2943–2945, 1981.

[54] P Gaunt. Magnetic viscosity and thermal activation energy. *Journal of Applied Physics*, 59:4129–4132, 1986.

[55] H C Hamaker. The london-van der waals attraction between spherical particles. *Physica*, 4:1058–1072, 1937.

[56] K. O'Grady, R. W. Chantrell, and I. L. Sanders. Magnetic characterisation of thin film recording media. *IEEE Transactions on Magnetics*, 29:286–291, 1993.

[57] R Kaiser and G Miskolczy. Magnetic properties of stable dispersions of subdomain magnetite particles. *Journal of Applied Physics*, 41:1064–1072, 1970.

[58] P Bagchi. Enthalpic repulsion between two identical spherical particles coated with a polymeric adsorption layer. *Journal of Colloid And Interface Science*, 41:380–382, 1972.

[59] R W Chantrell, J Popplewell, and S W Charles. Measurements of particle size distribution parameters in ferrofluids. *IEEE Transactions on Magnetics*, 14, 1978.

[60] S Roussakow. History of magnteic hyperthermia rise and decline. *Conference Papers in Medicine*, 2013:1–40, 2013.

[61] A M Granov, O V Muratov, and V F Frolov. Problems in the local hyperthermia of inductively heated embolized tissues. *Theoretical Foundations of Chemical Engineering*, 36:63–66, 2002.

[62] R K Gilchrist, R Medal, W D Shorey, R C Hanselman, J C Parrott, and C B Taylor. Selective inductive heating of lymph nodes. *Annals of Surgery*, 146:596–606, 1957.

[63] J P Reilly. Principles of nerve and heart excitation by time-varying magnetic fields. *Annals of the New York Academy of Sciences*, 649:96–117, 1992.

[64] V Craciun, G Calugaru, and V Badescu. Accelerated simulation of heat transfer in magnetic fluid hyperthermia, 2001.

[65] Y Rabin. Is intracellular hyperthermia superior to extracellular hyperthermia in the thermal sense? *International Journal of Hyperthermia*, 18:202, 2002.

[66] F E Luborsky. Development of elongated particle magnets. *Journal of Applied Physics*, 32, 1961.

[67] I Andreu and E Natividad. Accuracy of available methods for quantifying the heat power generation of nanoparticles for magnetic hyperthermia accuracy of available methods for quantifying the heat power generation of nanoparticles for magnetic hyperthermia. *International Journal of Hyperthermia*, 29:739–751, 2013.

[68] Y Yuan and D-A B Tasciuc. Comparison between experimental and predicted specific absorption rate of functionalized iron oxide nanoparticle suspensions. *Journal of Magnetism and Magnetic Materials*, 323:2463–2469, 2011.

[69] T L Kline, Y-H Xu, Y Jing, and J-P Wang. Biocompatible high-moment feco-au magnetic nanoparticles for magnetic hyperthermia treatment optimization. *Journal of Magnetism and Magnetic Materials*, 321:1525–1528, 2009.

[70] E Natividad, M Castro, and A Mediano. Adiabatic vs. non-adiabatic determination of specific absorption rate of ferrofluids. *Journal of Magnetism and Magnetic Materials*, 321:1497–1500, 2009.

[71] S Huang, S Y Wang, A Gupta, D A Borca-Tasciuc, and S J Salon. On the measurement technique for specific absorption rate of nanoparticles in an alternating electromagnetic field. *Measurement Science and Technology*, 23:1–6, 2012.

[72] A A McGhie, C Marquina, K. O'Grady, and G Vallejo-Fernandez. Measurement of the distribution of anisotropy constants in magnetic nanoparticles for hyperthermia applications. *Journal of Physics D: Applied Physics*, 50:455003, 11 2017.

[73] S Foner. Vibrating sample magnetometer. *Review of Scientific Instruments*, 27:548, 1956.

[74] Lake Shore Cryotronics. *Lakeshore Model 8600 Operating Manual*. Lake Shore Cryotronics Inc., 2019.

[75] D M Clarke, C Marquina, D C Lloyd, and G Vallejo-Fernandez. Effect of the distribution of anisotropy constants on the magnetic properties of iron oxide nanoparticles. *Journal of Magnetism and Magnetic Materials*, 559:169543, 10 2022.

[76] M Knoll and E Ruska. Das elektronenmikroskop. *Zeitschrift für Physik*, 78:318–339, 5 1932.

[77] J Goldstein, D E Newbury, D C Joy, C E Lyman, P Echlin, E Lifshin, L Sawyer, and J R Michael. *Scanning Electron Microscopy and X-ray Microanalysis: Third Edition*. Springer US, third edition, 2013.

[78] T E Everhart and R F M Thornley. Wide-band detector for micro-microampere low-energy electron currents. *Journal of Scientific Instruments*, 37, 1960.

[79] ImageJ. https://imagej.nih.gov/ij/.

[80] A Drayton, J Zehner, J Timmis, V Patel, G Vallejo-Fernandez, and K O'Grady. A comparative measurement technique of nanoparticle heating for magnetic hyperthermia applications. *Journal of Physics D: Applied Physics*, 50, 2017.

[81] S B Slade, G. Kassabian, and A E Berkowitz. Combination high-sensitivity alternating current susceptometer and high-frequency b-h looper. *Review of Scientific Instruments*, 67:2871–2876, 1996.

[82] L M Lacroix, J Carrey, and M Respaud. A frequency-adjustable electromagnet for hyperthermia measurements on magnetic nanoparticles. *Review of Scientific Instruments*, 79, 2008.

[83] E Garaio, J M Collantes, J A Garcia, F Plazaola, S Mornet, F Couillaud, and O Sandre. A wide-frequency range ac magnetometer to measure the specific absorption rate in nanoparticles for magnetic hyperthermia. *Journal of Magnetism and Magnetic Materials*, 368:432–437, 2014.

[84] I V Nicolae and V Socoliuc. High amplitude oscillating magnetic field applicator for remote magnetic nanoparticle detection. volume 1916, 2017.

[85] D E Bordelon, R C Goldstein, VS Nemkov, A Kumar, J K Jackowski, T L DeWeese, and R Ivkov. Modified solenoid coil that efficiently produces high amplitude ac magnetic fields with enhanced uniformity for biomedical applications. *IEEE Transactions on Magnetics*, 48:47–52, 1 2012.

[86] E Garaio, J M Collantes, F Plazaola, J A Garcia, and I Castellanos-Rubio. A multifrequency eletromagnetic applicator with an integrated ac magnetometer for magnetic hyperthermia experiments. *Measurement Science and Technology*, 25, 2014.

[87] Fair-Rite Material 78 Datasheet. https://www.fair-rite.com/78-material-data-sheet/, 6 2021.

[88] M Prasad, R Rani Rao, and A K Ray Chaudhuri. A versatile ac mutual inductance bridge. *J. Phys. E: Sci. Instrum*, 19:1013, 1986.

[89] P Horowitz and W Hill. *The Art of Electronics*. Third edit edition, 1980.

[90] Magnetherm Consumables. http://www.nanotherics.com/magnetherm-consumables/.

[91] K O'Grady, J Popplewell, and S W Charles. Initial susceptibilty of ferrofluids. *Journal of Magnetism and Magnetic Materials*, 39:56–58, 1983.